3-D SEISMIC SURVEY DESIGN VIA MODELING AND REVERSE TIME MIGRATION:

PIERCE JUNCTION SALT DOME, TEXAS

A Thesis

Presented to

the Faculty of the Department of Earth and Atmospheric Sciences

University of Houston

In Partial Fulfillment

of the Requirements for the Degree

Master of Science

By

Suleyman Coskun

University of Houston

May 2014

3-D SEISMIC SURVEY DESIGN VIA MODELING AND REVERSE TIME MIGRATION:

PIERCE JUNCTION SALT DOME, TEXAS

_____

Suleyman Coskun

APPROVED:

_____

Dr. Robert Stewart (Chairman)

_____

Dr. Shuhab Khan (Member)

_____

Dr. Edip Baysal (Member)

_____

Dean, College of Natural Sciences and Mathematics

ACKNOWLEDGEMENTS

I would like to express my deepest appreciation to my advisor, Dr. Stewart for his guidance, understanding, and patience during my research. I am also very thankful to Dr. Shuhab Khan for his support and comments. My sincere thanks goes to Dr. Edip Baysal for his invaluable guidance and assistance in the preparation of this research. I would also extend my gratitude to Dr. Orhan Yilmaz and Irfan Tanritanir for their great support at Paradigm.

I also acknowledge Paradigm, GEDCO, and Geosoft for technical and software support. Texas Brine Company is also thanked for giving Allied Geophysical Laboratories (AGL) the unique opportunity to work in their facility. I sincerely thank the Turkish Petroleum Corporation (TPAO) for financially supporting me throughout my study.

I thank my fellows in University of Houston: Omer Akbas, Unal Okyay, Kenan Yazan, Sercan Pisen, Gokhan Kose, Eray Kocel, Ozbil Yapar, and all AGL members for their all-time support for this research.

I wish to express my great gratitude to my parents, Edip and Sehnaz Coskun, and to my brother Gokhan Coskun for their understanding, support, and encouragement.

Finally, and most importantly, it is difficult to find words to express my gratitude for my beloved wife, Selin Deniz Coskun. Her support, encouragement, quiet patience, and unwavering love inspired me to be successful both in my life and studies. I am also very grateful to her for bringing two adorable sons, Selim and Cihangir, to our family.

3-D SEISMIC SURVEY DESIGN VIA MODELING AND REVERSE TIME MIGRATION:

PIERCE JUNCTION SALT DOME, TEXAS

An Abstract of a Thesis

Presented to

the Faculty of the Department of Earth and Atmospheric Sciences

University of Houston

In Partial Fulfillment

of the Requirements for the Degree

Master of Science

By

Suleyman Coskun

University of Houston

May 2014

ABSTRACT

Seismic forward modeling studies are required for adequately imaging complex geological structures, such as folds, faults, and domes. Many U.S. Gulf Coast salt domes are used for oil and gas exploration, brine production, and underground hydrocarbon storage. For this reason, it is crucial to image the flank of the salt domes and surrounding sediments. Allied Geophysical Laboratories (AGL) carried out a 2-D seismic study in the Texas Brine Company facility to image the Pierce Junction salt dome. However, we were not able to image the salt flanks because of improper survey design. This led to the current study which proposes a 2-D and a 3-D seismic survey design using modeling and Reverse Time Migration (RTM) imaging.

We gathered original 2-D seismic, topography, and gravity data to build 2-D and 3-D velocity models of the Pierce Junction salt dome area. We processed the original 2-D data and extracted the velocities of the cap rock and near surface sediments for use in velocity models. We modelled gravity data collected in a north-south direction and performed analyses on the synthetic seismic data to determine new 2-D conventional seismic survey parameters that could be achieved with the limited acquisition equipment of AGL. We modeled synthetic shot gathers by a finite difference method using the full (two-way) acoustic wave equation, and generated seismic images using the Reverse Time Migration (RTM) method.

We determined the optimum parameters of the new 2-D seismic survey by reviewing the quality of the results. These parameters were able to adequately image the salt dome and its surrounding sediments. We then modified the 2-D parameters for a new 3-D survey, and obtained synthetic RTM images based on the 3-D velocity model.

Optimal 2-D and 3-D seismic survey designs for the Pierce Junction salt dome area were achieved using seismic modeling and RTM imaging. We found RTM imaging to be a novel and powerful method for determining seismic survey parameters for complex geological structures.

TABLE OF CONTENTS

CHAPTER ONE: INTRODUCTION

1.1 Motivation and Scope

A seismic project is comprised mainly of data acquisition, processing, and interpretation. Survey design and acquisition mostly determine the quality of processing and interpretation. Even the best processing techniques cannot reveal good results from data that have some insufficiencies in acquisition. Therefore, processing and interpretation should be considered in the survey design and acquisition part of a seismic study.

The goal of designing seismic surveys is to balance the cost of the survey and imaging needs of the interpreter. Expenses, equipment demands, and time limitations of surveys force geophysicists considering survey parameters to take economical, logistical, and technical parameters into account. Good survey design can only be possible by gathering as much information as possible from the survey area.

Stone (1994) identified two important survey objectives that should be kept in mind while planning a seismic survey: **(1) the primary objective** is to obtain geophysical data that provide a representation of the subsurface geology that is adequate to meet interpretational goals, and **(2) the secondary objective** is to acquire the maximum amount of data within budgeted funds and available time.

Acquisition parameters calculated by general survey design formulas are usually adequate to image flat layers and slightly dipping surfaces. However, determining these parameters for complex structures, such as folds, faults, domes, and reefs is more difficult due to complicated wave field behavior in these areas. Seismic data acquisition simulations over a model of the study area can provide crucial information for determining survey parameters. If a model is constructed close enough to the real structure, it is possible to obtain very realistic synthetic seismic data using seismic modeling. Therefore, seismic modeling is one of the most economical ways to establish and test the optimum acquisition parameters so as to get the best image of complex geological structures.

The Pierce Junction salt dome is one of the hundreds of salt domes in the U.S. Gulf Coast. Besides oil and gas production, brine production and underground hydrocarbon storage facilities are established in the field. The brine-producing caverns are operated by drilling the edge of the salt dome. Adequately imaging the salt dome flanks can reduce the risk of natural disasters such as sinkholes and hydrocarbon seepage. A 2-D seismic study was carried out in the Texas Brine Company facility by Allied Geophysical Laboratories (AGL). New 2-D and 3-D seismic surveys were also proposed since the original 2-D seismic data could only image a portion of the top of the salt. The motivation for this study is to investigate the feasibility of additional 2-D and 3-D seismic surveys for imaging the salt dome flanks and surrounding sediments using AGL's limited equipment.

The purpose of this study is to provide a seismic survey design decision method by an acquisition modeling study using the Pierce Junction salt dome area as an example. Two-D and 3-D velocity models of the area were built as close to the real environment as possible, and survey design parameters were determined by updating the initial survey parameters with finite difference modeling and Reverse Time Migration (RTM) images.

1.2 Structural Framework of the U.S. Gulf Coast

The Gulf of Mexico Basin is an elongated structural basin with a length of about 1,500 km. As shown in Figure 1.1, the offshore part of the basin comprises the Gulf of Mexico which covers an area of more than 1,500,000 km^2 (Salvador, 1991). The abyssal plain (> 3000 m deep) constitutes 20% of the Gulf, while the continental shelf (< 180 m deep), continental slope (180-3000m deep), and shallow and intertidal areas (< 20m deep) comprise 20%, 22%, and 38% of the Gulf, respectively (Gore, 1992).

The offshore area of the basin is bounded by a low coastal plain to the north and west. The low coastal plain is less than 50 km wide in east-central Mexico and more than 550 km wide in the central part of the United States Gulf Coastal Plain, including parts of the states of Texas, Louisiana, Mississippi, and Arkansas. Gulfward limits of the shallow parts of the Florida and Yucatan platforms are marked by the Florida and Campeche escarpments, where the floor of the Gulf of Mexico drops steeply to the east and south.

The limits of the Gulf of Mexico Basin are defined by structural features shown in Figure 1.2. The southern and eastern limits of the basin are estimated to be the Yucatan

and Florida carbonate platforms. The foot of the Chiapas massif, the Sierra Madre Oriental of Mexico, and the eastern edge of the Coahuila platform, form the western limits of the basin. The northern limit of the basin corresponds to a series of structural features: from west to east, these are the basinward flanks of the Marathon uplift, the Ouachita orogenic belt, the Ouachita Mountains, the Central Mississippi deformed belt, and the southern reaches of the Appalachian Mountains. The limit between Appalachian Mountains and the eastern limit of the basin is arbitrary, since there is no apparent structural feature observable separating the shores of the Atlantic Ocean and Atlantic Coastal Plain (Salvador, 1991).

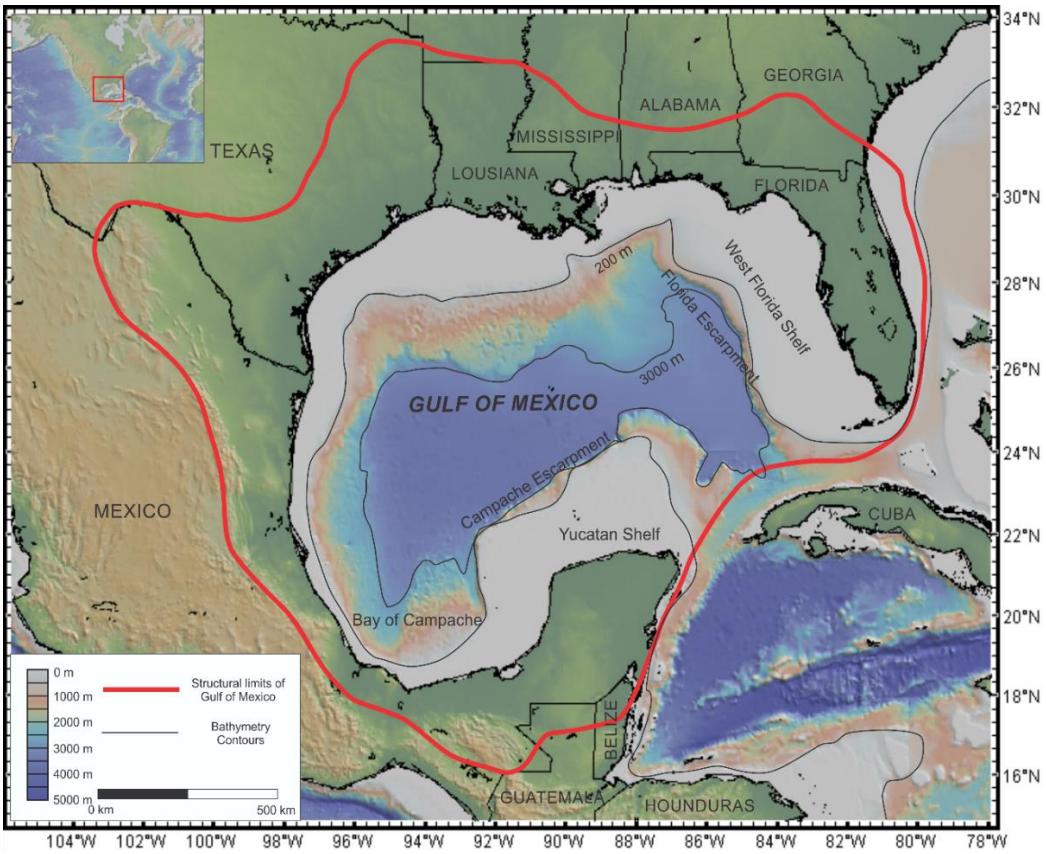

Figure 1.1. Location and structural limits of Gulf of Mexico Basin (modified after Salvador, 1991)

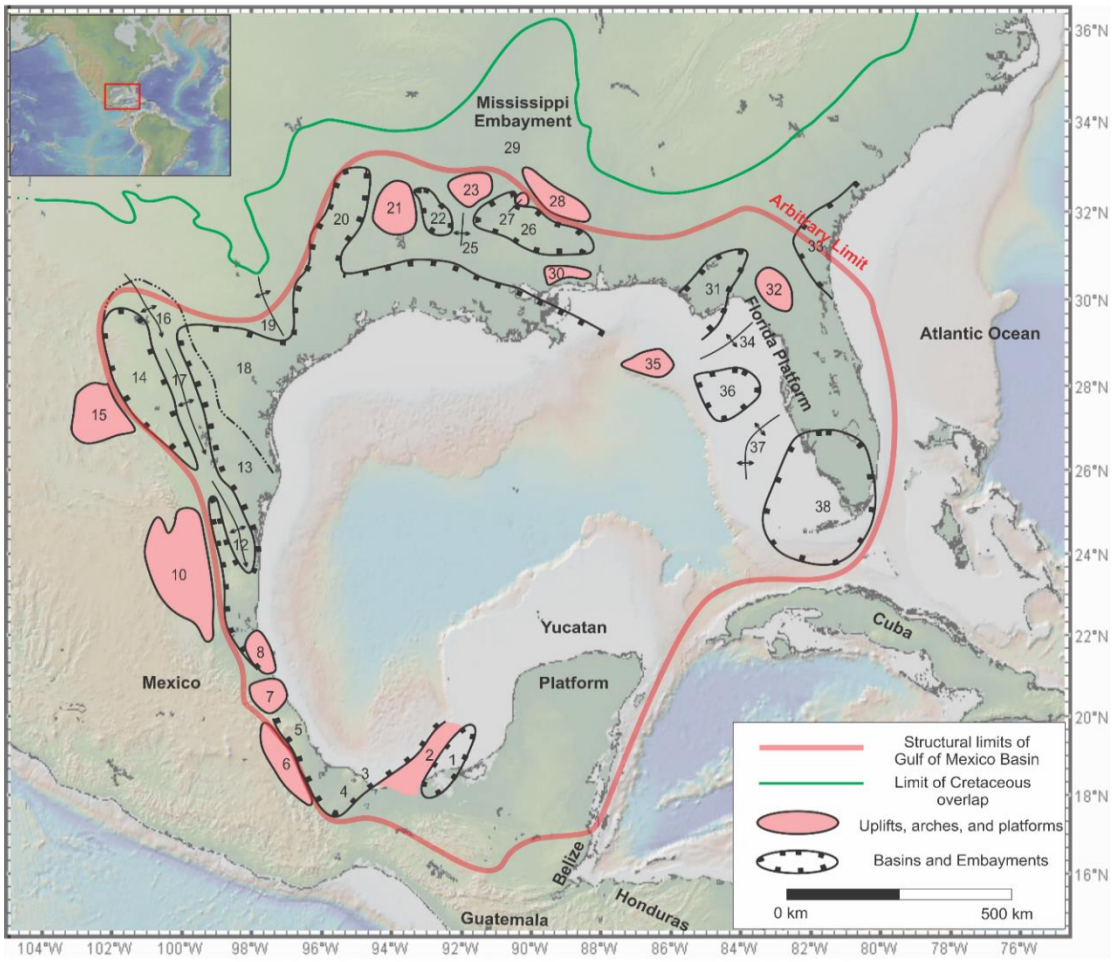

Figure 1.2. Second-order structural features within Gulf of Mexico Basin: 1, Macuspana basin; 2, Villahermosa uplift; 3, Comalcalco basin; 4, Isthmus Saline basin; 5, Veracruz basin; 6, Cordoba platform; 7, Santa Ana massif; 8, Tuxpan platform; 9, Tapica-Misantla basin; 10, Valles-San Luis Potosi platform; 11, Magiscatzin basin; 12, Tamaulipas arch; 13, Burgos basin; 14, Sabinas basin; 15, Coahuila platform; 16, El Burro uplift; 17, Peyotes-Picachos arches; 18, Rio Grande embayment; 19, San Marcos arch; 20, East Texas basin; 21, Sabine uplift; 22, North Louisiana salt basin; 23, Monroe uplift; 24, Desha basin; 25, La Salle arch; 26, Mississippi salt basin; 27, Jackson dome; 28, Central Mississippi deformed belt; 29, Black Warrior basin; 30, Wiggins uplift; 31, Apalachicola embayment; 32, Ocala uplift; 33, Southeast Georgia embayment; 34, Middle Ground arch; 35, Southern platform; 36, Tampa embayment; 37, Sarasota arch; 38, South Florida basin (modified after Salvador, 1991).

The Cenozoic tectonic history of the basin is dominated by salt-related deformation in the Gulf of Mexico. Basinward and landward dipping normal faults, contractional folds, and different types of salt structures are the major elements of the salt-related deformation (Figure 1.3). Eight river systems drain into the northern Gulf of Mexico basin: the Norma, Rio Grande, Carriso, Corsar, Houston, Red River, and Central and Eastern branches of the Mississippi River; these deposit their sediment loads in the coastal zone, continental shelf, and slope (Konyukhov, 2008). Salt flow activity began with the differential loading and gliding, the major elements of the driving force of salt flow. A variety of complex structures were formed by deformation caused by this salt flow. A block diagram illustrating schematic shapes of salt structures is shown in Figure 1.4.

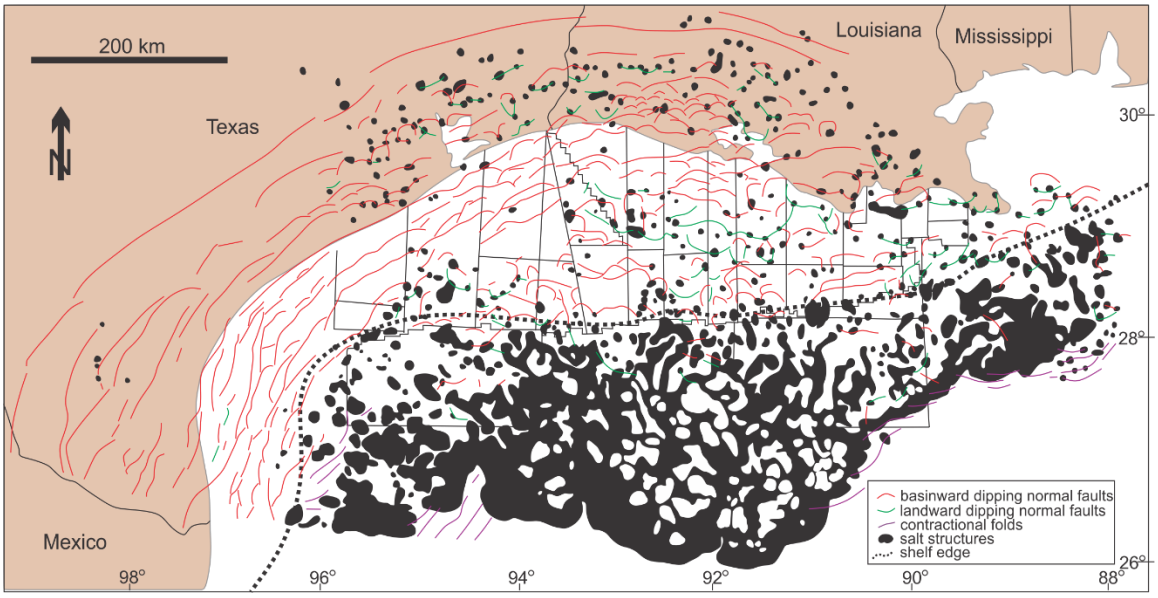

Figure 1.3. Structural elements and salt structures that cause salt-related deformation in the Gulf of Mexico (modified after Konyukhov, 2008).

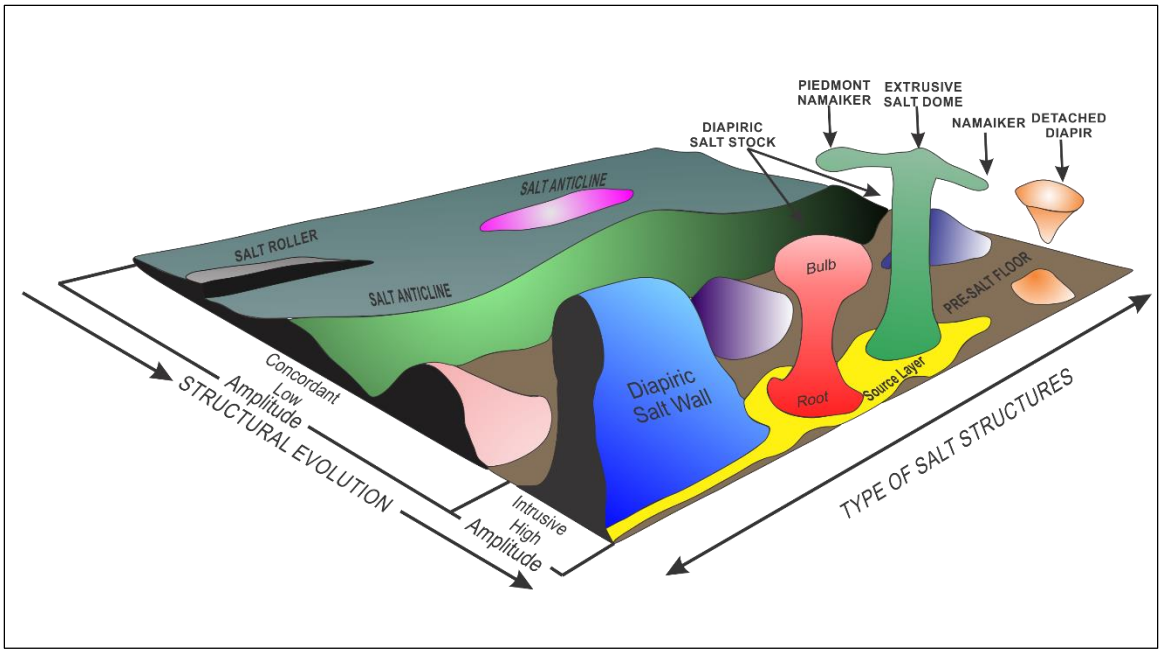

Figure 1.4. Salt structures displaying the evolution of salt tectonics (modified after Jackson and Talbot, 1986)

The Gulf of Mexico can be structurally divided into three major provinces: the northern progradational margin, the eastern carbonate margin, and the western compressional margin (Figure 1.5). The northern progradational margin is the best known part of Gulf of Mexico, since there are extensive oil and gas exploration well data and publications about the area. The northern progradational margin extends from northeastern Mexico to Alabama, and can be subdivided into the interior zone (Mesozoic structures) and the coastal zone (Cenozoic structures). In the interior zone, depositional and active tectonic basins and uplifts, and salt diapirism affected the early mixed clastic-carbonate shelf margin in the Late Jurassic and Early Cretaceous ages. This zone is also called the interior salt diapir province. In the coastal zone, a thick wedge of Upper Cretaceous and Cenozoic coarse clastic sediments, overlying the Mesozoic strata, have

caused progradation of the shelf margin hundreds kilometers seaward, generating "growth fault" systems and forming the coastal and offshore salt diapir provinces. The Florida and Yucatan carbonate platforms cover the large-scale and poorly known basins and uplifts in the eastern coastal carbonate margins. The western compressional margin covers the area from the Isthmus of Tehuantepec to northeastern Mexico. Laramide (Late Cretaceous-Eocene) folding and thrusting dominated the carbonate margin in the area (Ewing, 1991). Additional discussion will be limited to the northern progradational margin, as it is the main focus of this study.

The interior zone of the northern progradational margin covers a broad complex of embayments, which extend from the San Marcos arch eastward to Alabama. The zone is divided into basin and embayment provinces by the Sabine and Monroe uplifts. The Sabine uplift, located in the center of the embayment, splits the embayment into East Texas to the west, and the North Louisiana and Mississippi salt basins to the east. Also, the Mississippi embayment is separated from the southern basins by the Monroe uplift (Ewing, 1991). Important structural features in the interior zone are, from east to west, the Rio Grande embayment, San Marcos arch, East Texas basin, Sabin uplift, North Louisiana salt basin, Monroe uplift, Desha basin, and Mississippi salt basin.

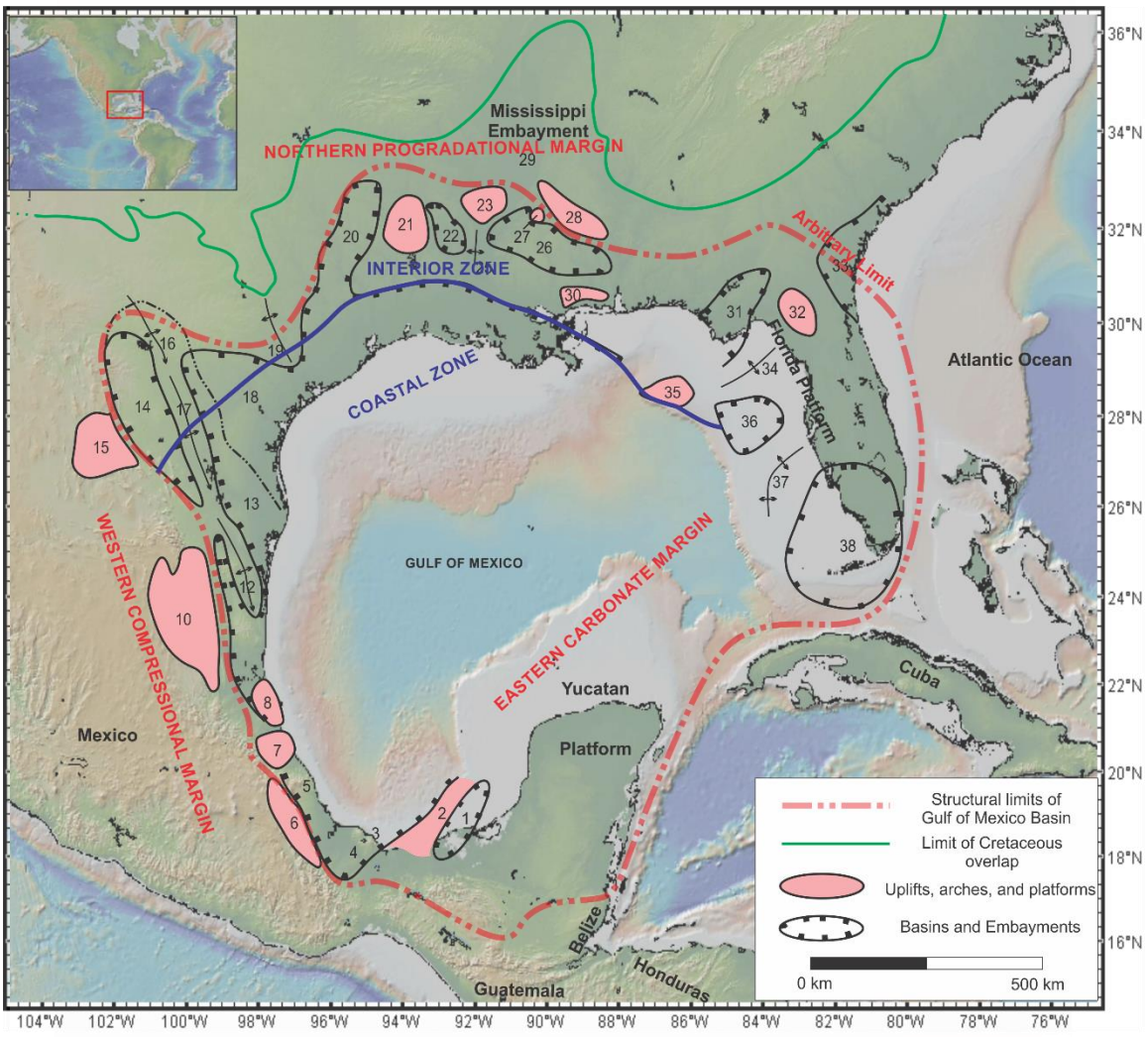

Figure 1.5. Index map showing major structural elements and provinces. The blue line is the boundary between the interior and coastal zones of the northern progradational margin. (modified after Ewing, 1991).

The Rio Grande, East Texas, Northern Louisiana, Mississippi, East Central, De Soto Canyon, Texas-Louisiana Slope, Perdido, South Louisiana Shelf, and West Florida salt dome basins are the ten major salt-controlled provinces of the interior and coastal zones of the northern progradational margin (Halbouty, 1967). The difference between styles of occurrence of salt and/or spatial clustering characterizes these salt diapir provinces.

Ewing (1991) states that the salt in diapir provinces may have been deposited in the Jurassic.

Our area, the Pierce Junction salt dome, is located in the Houston embayment, which is situated in the South Louisiana Shelf diapir province (Figure 1.6). The Houston embayment includes about 60 salt diapirs and a few salt pillows. The southern and western boundaries of the province do not contain distinct salt structures. On the other hand, the province merges with the South Louisiana province to the east. The East Texas basin is also connected to the province with a small line of diapirs on the northwest (Ewing, 1991).

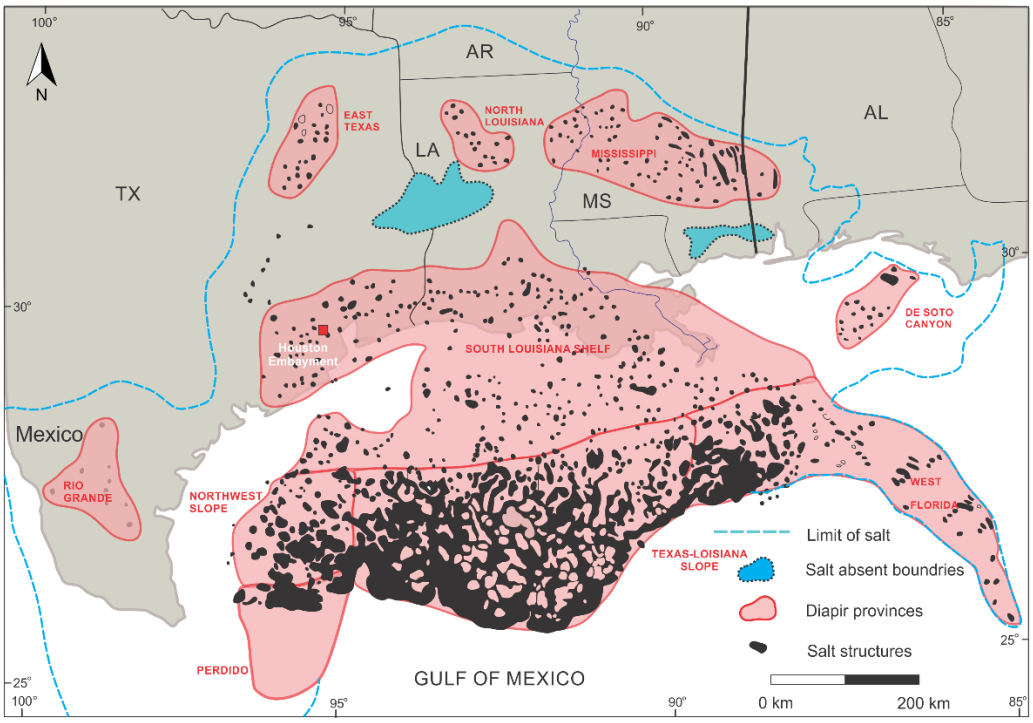

Figure 1.6. Salt diapir provinces of the northern progradational margin. The red square indicates our study area (modified after Ewing, 1991).

1.3 Fundamentals of Salt Dome Geology

1.3.1 Salt Dome Formation

Sedimentary loading after the tectonic stabilization of the Gulf of Mexico caused the development of the salt and salt dome basins predominantly in the Gulf Coast region (Halbouty, 1967). Deformation caused by gravity acting on the weak base of abnormally pressured shales and/or salt resulted in two main forms: salt-flow structures and listric-normal faults. Sediments that overlie or load the salt create a pressure gradient that provides salt flow. Many types of salt structure were developed by movement of the salt from areas of higher pressure toward areas of lower pressure because of differential loading of the overlaying or loading sediments (Nelson, 1991).

The term “salt” refers to a group of minerals, including both non-radioactive evaporites (halite, anhydrite, gypsum, and trona) and radioactive evaporites (sylvite, carnallite, langbeinite, polyhalite, and kainite). However, this term is also used for halite, as the salt contains 90%-98% of this mineral (Kupfer, 1989; Halbouty, 1979). The specific gravity of rock salt is usually greater than the specific gravity of halite (2.164) because of impurities dispersed through salt. Anhydrite is the most common mineral which affects the purity of salt. Hence, the average density of rock salt is often assumed to be 2.2 g/cc, calculated by a salt structure composed of 95% halite and 5% anhydrite. Composition and specific gravity of evaporite minerals are shown in Table 1.1.

Table 1.1. Composition and specific gravity of evaporite minerals (from Carmichael, 1984).

Mineral	Composition	Specific Gravity
Non-radioactive Evaporites		
Halite	NaCl	2.164
Anhydrite	$CaSO_4$	2.960
Gypsum	$CaSO_4 \cdot 2H_2O$	2.320
Trona	$Na_3(CO_3)(HCO_3) \cdot 2H_2O$	2.120
Radioactive Evaporites		
Sylvite	KCL	1.984
Carnallite	$KMgCl_3 \cdot 6H_2O$	1.610
Langbeinite	$K_2Mg_2(SO_4)_3$	2.830
Polyhalite	$K_2MgCa_2(SO_4)_4 \cdot 2H_2O$	2.780
Kalinite	$MgSO_4 \cdot KCl \cdot 3H_2O$	2.130

Salt flow is possible where driving forces overwhelm resisting forces. The major driving force of salt flow is differential loading. Overburden strength and boundary friction within the salt layer are considered to be the principle resisting forces (Hudec and Jackson, 2007). The depth of salt burial, geometry of the salt body, geologic setting, and thermal conditions of the salt determine the type of loading: (1) gravitational loading, (2) displacement loading, or (3) thermal loading. The combination of the weight of the rocks overlying the salt and gravitational body forces within the salt form the gravitational loading. If the flanks of a salt body are shifted from their original position during a regional shortening or extension, it causes the displacement loading. Thermal loading is a result of deformation in volume of the salt due to changes in temperature (Hudec and Jackson, 2007).

The salt flow direction and the point at which equilibrium is reached is related to the density of the salt and the overlying sediments. Nelson (1991) explained the salt flow mechanism for this model with three cases; sediments in this interval are (1) the same density as the salt, (2) less dense than the salt, or (3) more dense than the salt (Figure 1.7).

In Nelson's first case, with sediments of equal density to salt, there is no pressure difference within the salt; therefore, salt flow cannot be observed in this case, as can be seen in Figure 1.7a.

In Nelson's second case, in which sediments are less dense than salt, the pressure beneath the salt is higher than the pressure beneath adjacent sediments at the same depth, as seen in Figure 1.7b; this pressure difference forces the salt to move from the local high to the adjacent salt bed. Consequently, the salt high will be suppressed in amplitude, and subsidence is observed in the overlying sediment. This case is generally observed where shallow salt sheets are developed.

In Nelson's third case, in which sediments are more dense than salt, the pressure difference causes the salt flow from the salt bed into the local salt high. The salt diapirs dominantly seen in Gulf of Mexico basin region are developed as a result of the upward movement of the salt through the local salt high; this is shown in Figure 1.7c.

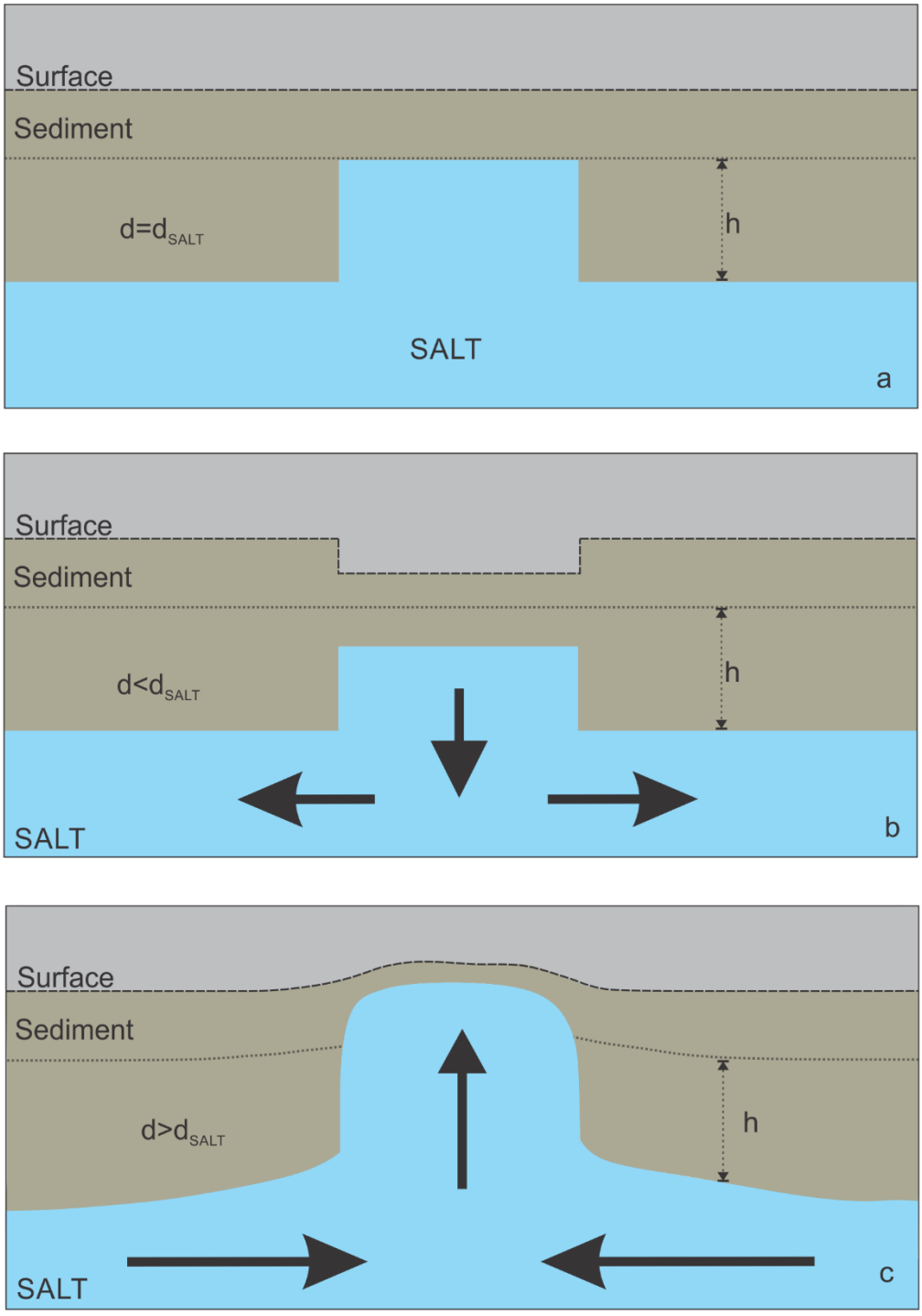

Figure 1.7. Model of differential loading related to structure on the top of the salt. a) Stable condition, b) damping of structural relief on top of the salt, c) model of diapirism. "h" indicates the interval of the overlying sediment (modified after Nelson, 1991).

The “fluid mechanical theory” of Nettleton (1934) basically described salt-flow principles. According to Nettleton’s theory, the initial configuration which localize the dome, the thickness of mother salt layer, the strength or viscosity of overlying rocks, and the strength or viscosity of the salt are the significant factors that determine the final form of a salt dome. According to Nettleton, the formation of a piercement salt dome can be illustrated in six stages, shown in Figure 1.8: (1) The initial stage of formation does not begin until the deposition of adequate sediments over the salt produce a pressure difference on the salt bed; (2) Sediment accumulation continues, and the upward movement of the salt begins when sufficient pressure differences occur; (3) Salt piercement through the overburden begins and overlying rocks are carried upward by the salt. Also, the drop in the peripheral sink cuts off the salt supply flowing towards the dome. Hence, after this stage formation of the dome will be completed with the amount of the material within the peripheral sink and salt core; (4) The original material over the dome is almost eroded; (5) After complete erosion of overlying rocks, the cap rock is produced by the interaction between the salt and circulating ground water; (6) Collapse of the upturned beds into the peripheral sink in the form of block fault segments completes dome growth (Nettleton, 1934; Halbouty and Hardin, 1956; Halbouty, 1967).

Categorizing salt domes by their form, size, and relationship to host sediments is required. Salt domes are classified in two ways: descriptively and structurally. Descriptive classifications refer to: (1) the depth of burial of the salt mass below the surface, (2) the form or shape of the salt structure, and (3) the genetic relationship of the salt structure

or group of structures. Structural classification includes the relationship of (1) the upper portion of the salt to adjacent sediments, (2) the lower portion of the salt mass to the source bed, (3) the salt stock to structural features in adjacent strata, and (4) the salt core to numerous typical fault patterns (Halbouty, 1967).

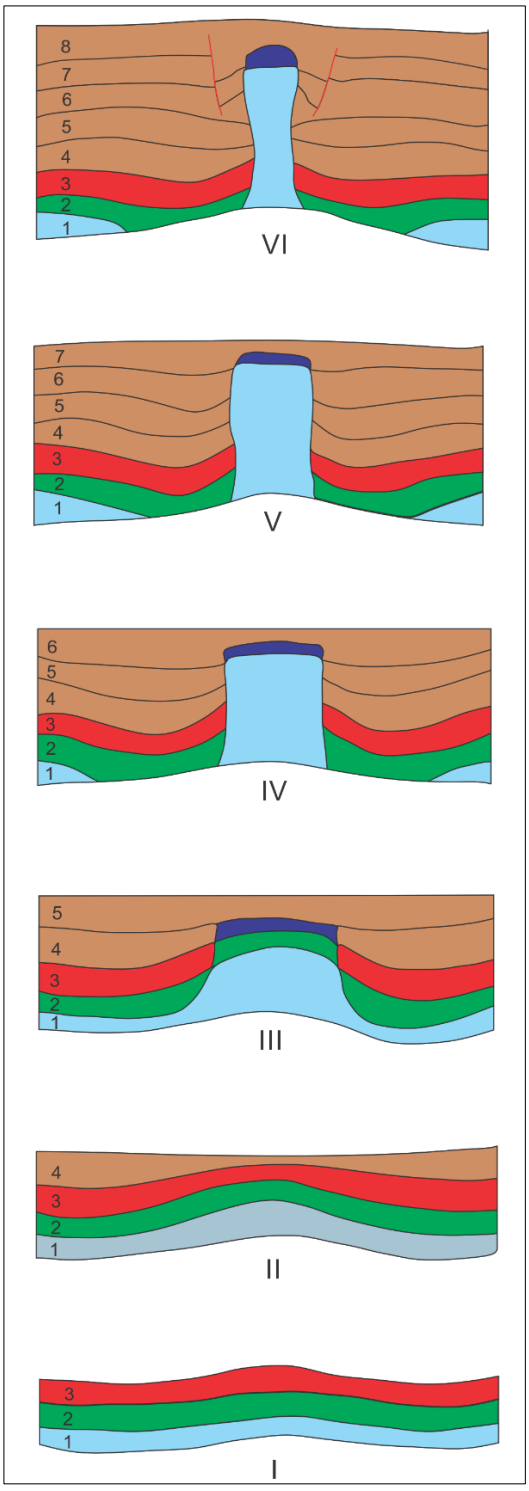

Figure 1.8. Development stages of a shallow piercement salt dome (modified after Nettleton, 1934).

1.3.2 Fault Systems around Salt Domes

Relative uplift of the sediments flanking the diapir results in fault activity around passive piercement salt domes. The reasons for diapir uplift can be attributed to a combination of salt withdrawal from the source layer, continued rise of salt plugs relative to source layers, and compaction and subsidence of the sediments surrounding salt plugs (Nelson, 1991).

The usual fault patterns around passive piercement salt domes are radial and commonly developed from the salt/sediment interface outward. Displacement of these faults is larger near a salt plug and become smaller down the flanks of the structure. Relative uplift produces an extensional stress around the circular salt plug. Since a salt plug has the tendency to move parallel to the salt/sediment interface, faults are developed perpendicular to that interface in response to the stress; this can be seen in Figure 1.9 (Nelson, 1991).

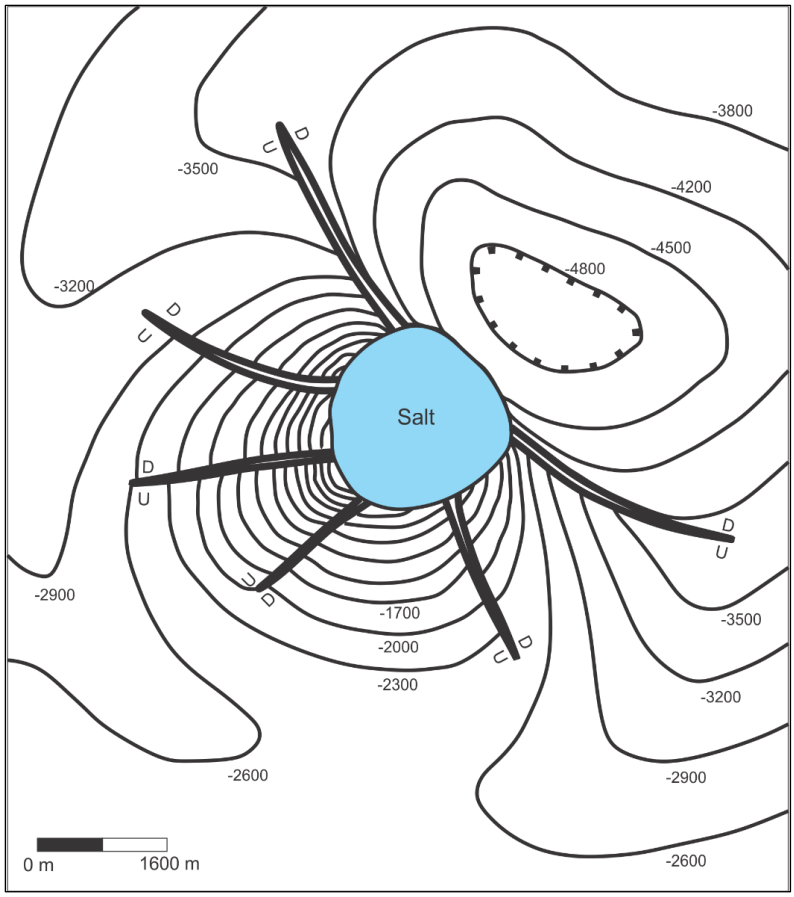

Figure 1.9. Schematic structure map of a sedimentary horizon around a typical piercement salt dome (modified after Nelson, 1991).

1.3.3. The Cap Rock

Cap rock can be described as layers of anhydrite, gypsum, and calcite that cover the salt plugs of passive piercement domes (Halbouty, 1979). A cross-section of a typical cap rock is shown in Figure 1.10. Dissolution of the top of the salt, generally by meteoric water, results in the formation of the cap rock (Murray, 1961; Posey and Kyle, 1988). Easily dissolved minerals, such as halite, are removed under these conditions. Minerals less soluble than halite accumulate along the salt/cap rock interface through a process called underplating (Kyle et al., 1987). Biogenic calcite and hydrogen sulfide are originated

by bacteria-associated chemical reactions of anhydrite and hydrocarbons present in the environment (Feely and Kulp, 1957). In a few situations, elemental sulfur can be formed by conversion of hydrogen sulfide. Hence, elemental sulfur can be preserved and deposited in the cap rock in commercial quantities (Halbouty, 1979).

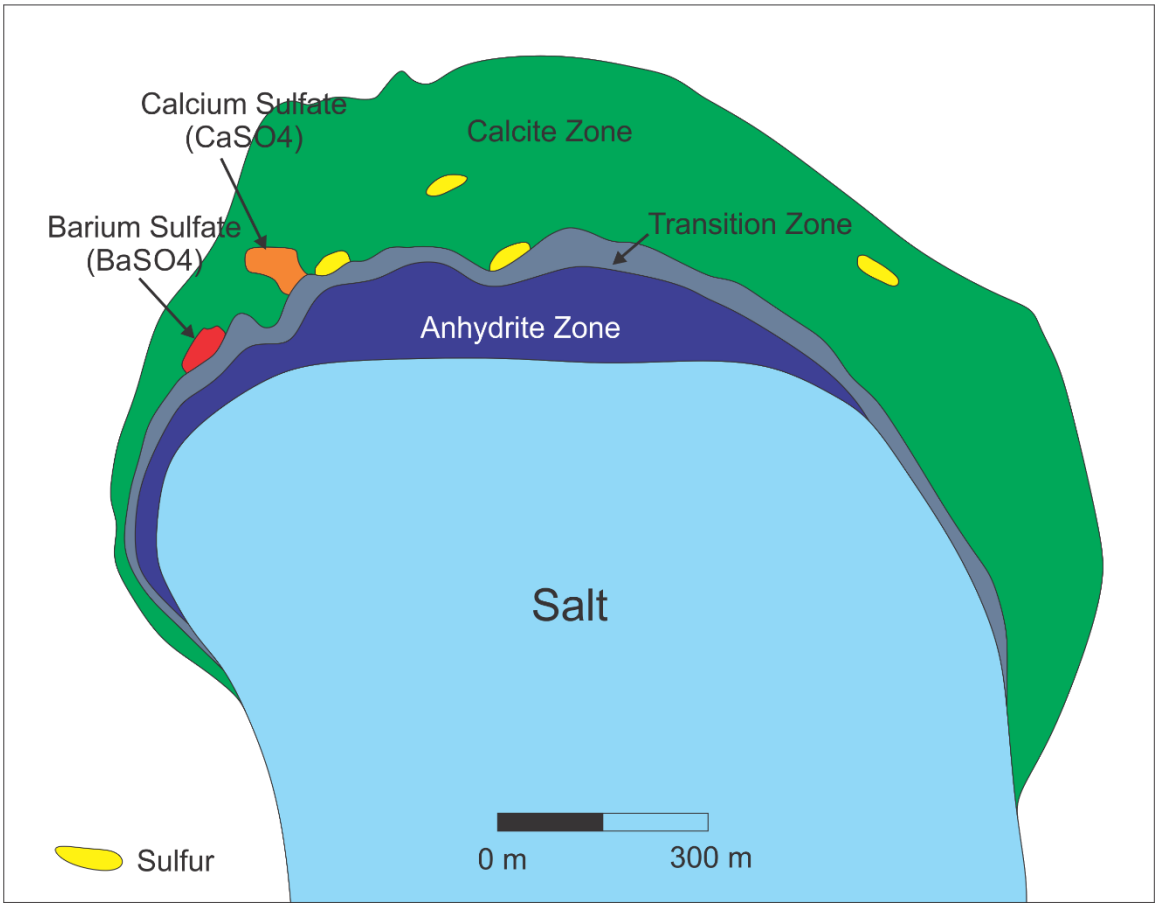

Figure 1.10. Cross-section of Jefferson Island dome, Iberia Parish, Louisiana showing three mineralogical zones typical of cap rock on many domes. Accessory minerals such as gypsum and sulfur, if present, are usually associated with the transition and calcite zones overlying the lower anhydrite zone (modified after Halbouty, 1967).

1.4 Thesis Organization

In **Chapter One,** we introduce the motivation and scope of this study, reviews the structural framework of the Gulf Coast dominated by salt structures, and addresses the fundamentals of salt dome geology.

In **Chapter Two,** we describe the data and methods used in 2-D and 3-D velocity model building. First, we present an overview of the Pierce Junction salt dome; then in order to gather more information for accurate velocity models, we interpret a series of geophysical data acquired and processed from the study area.

In **Chapter Three**, we describe our acquisition modeling steps. We define velocity model building procedures and then present our determination of seismic survey design parameters by acquisition modeling. We discuss the results and analyses of our survey designs, with RTM image examples.

In **Chapter Four**, we discuss the products of this study in terms of survey feasibility, equipment requirements, and cost; we present both problems that can be encountered while acquiring data in real environments and offer solutions.

In **Chapter Five**, we address the limitations of this study.

In **Chapter Six**, we present a summary and our conclusions.

CHAPTER TWO: DATA AND METHODS

2.1 Study Area

The Pierce Junction salt dome is located seven miles southwest of downtown Houston, in southern Harris County. It is named for its location at the intersection of what was then Buffalo Bayou, the Brazos and Colorado Rivers, and the Houston Tap railroad (Figure 2.1).

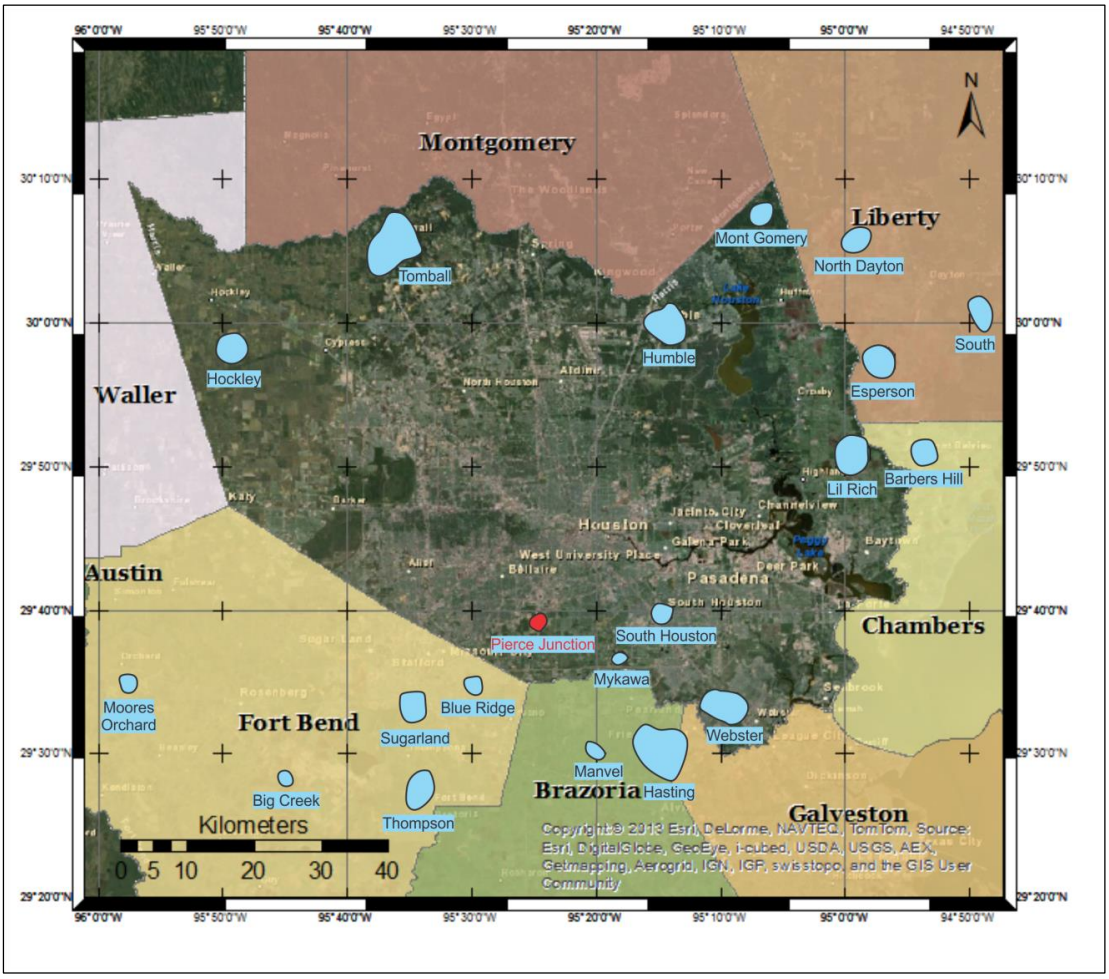

Figure 2.1. Location of Pierce Junction salt dome. Blue areas represent Gulf Coast salt domes (Huffman, 2004) in the Houston Metropolitan area within Harris County.

The dome is classified as a shallow piercement salt dome. As a typical Gulf Coast salt dome, it is overlain by cap rock and the salt spine is steep to overhanging. According to Beckman and Williamson (1990), the salt and overlying cap rock are encountered at depths of approximately 290 m and 207 m, respectively. The dome is almost circular and the area of the top of the salt is about 10 km^2, although it is about 35.25 km^2 at the deepest part (Beckman and Williamson, 1990). Elevation of the area is between 17 and 21 m above sea-level.

The stratigraphic sequence of formations in the Pierce Junction area is illustrated in Figure 2.2 and is based on the type electric log. Each stratigraphic unit from the lower Miocene through the lower Oligocene contains oil that is mostly accumulated on the flanks of the structure (Glass, 1953). The schematic west-east cross-section of the field indicates the stratigraphic convergence and arching of sediment bordering the salt. As seen in Figure 2.3, on the eastern flanks of the dome, the presence of steeply dipping and overturned beds are evidence of the increased structural effects of drag between the salt plug and sediment next to it exists beneath the salt overhang (Glass, 1953).

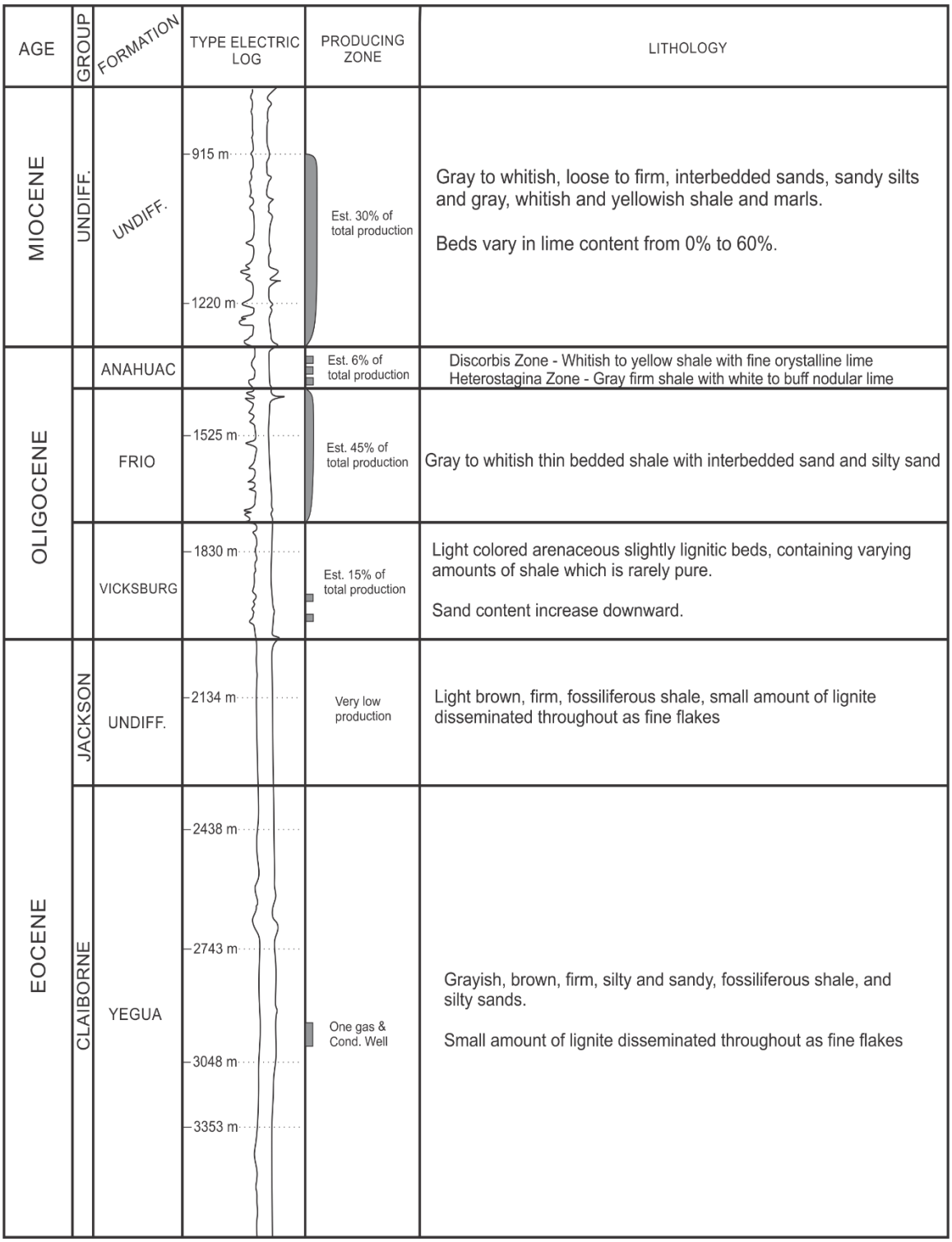

Figure 2.2. Stratigraphic section of Pierce Junction field (modified after Glass, 1953).

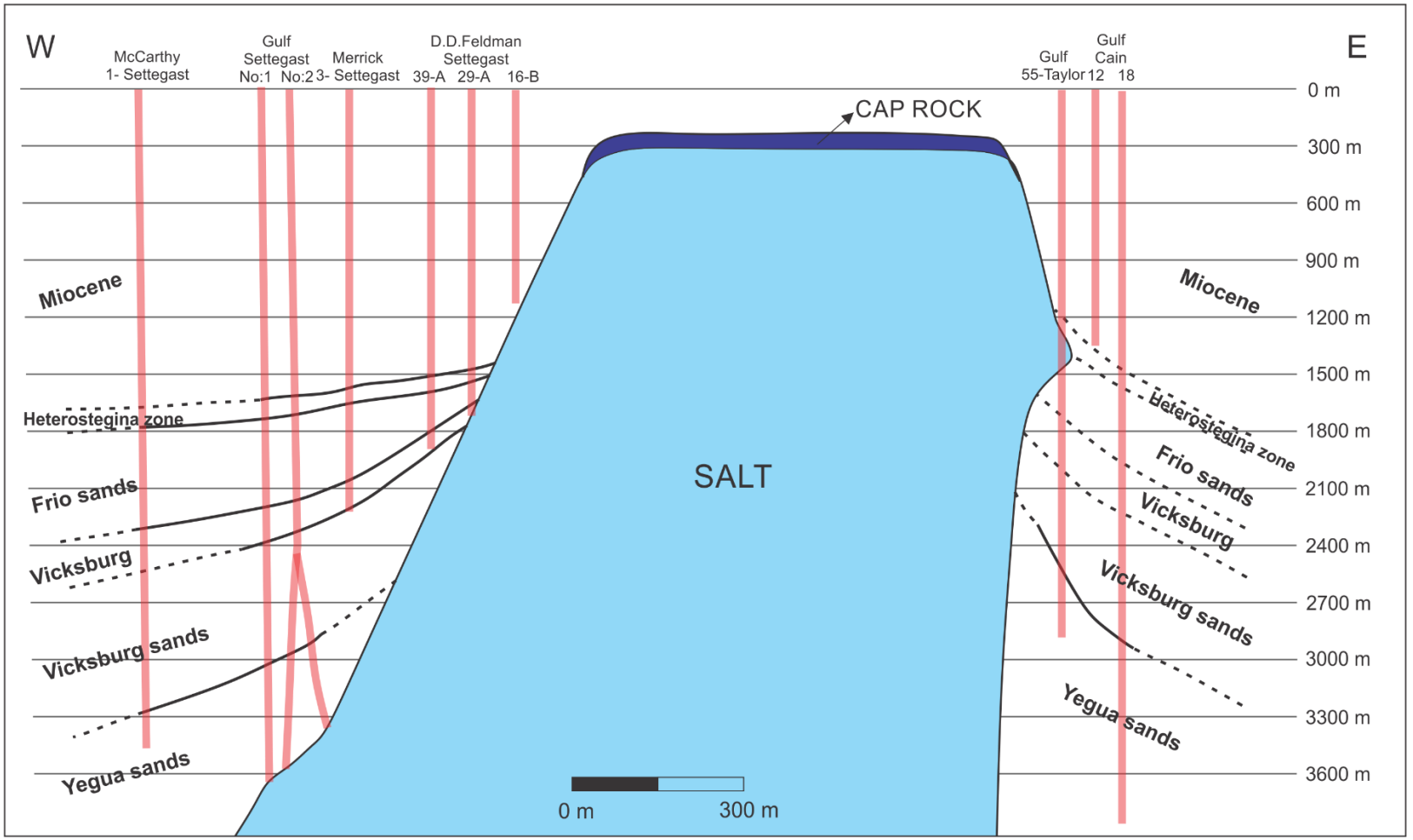

Figure 2.3. West–East Cross-section of Pierce Junction salt dome (modified after Glass, 1953).

The radial fault pattern formed by normal faults around the dome can be observed on the contour map of the "*heterostegina* zone" (Figure 2.4). Throws of those normal faults vary from 15 m to 90 m. The combination of structural effects of faulting and sedimentary movements ends up with a very complex structural pattern at the areas adjacent to the dome. Hence, this complex structure does not provide a reliable structural interpretation at the boundaries of the salt (Glass, 1953).

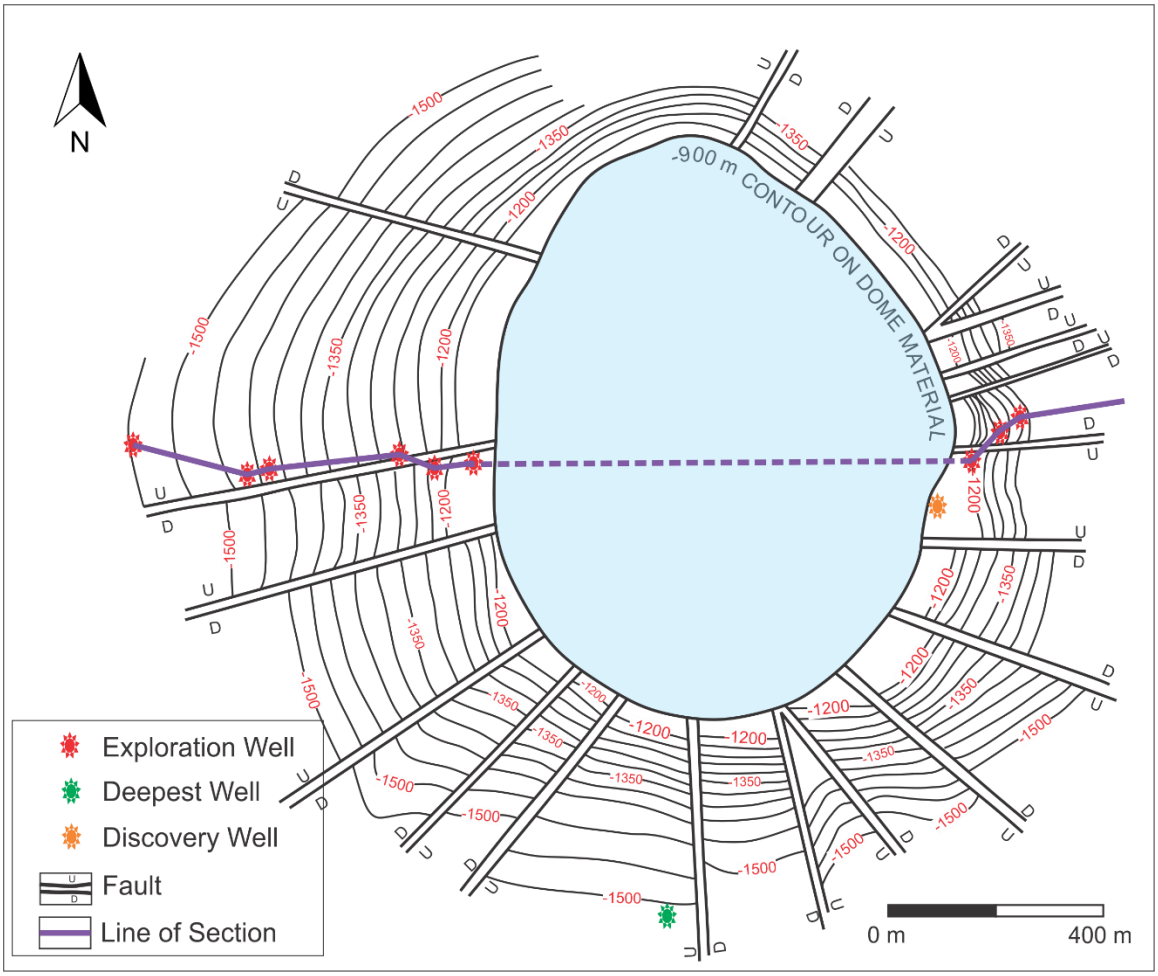

Figure 2.4. Contour map of top of the *heterostegina* zone around Pierce Junction salt dome (modified after Glass, 1953).

The Pierce Junction salt dome has an important place in oil and gas production history, as it is one of the earliest oil fields in Texas. The salt dome area was evaluated as barely productive in the early 1900s, since the poor drilling technology had not been successful on the first fifty-four holes. The first production at Taylor No. 2 gas well was made in 1921 by the South Texas Petroleum Company owned by Hugh Roy Cullen. It was first completed with a total depth of 1,072 m, and finally, initial flow of 3,000 barrels of oil per day was achieved at around 1,225 m depth. Until the 1930s, 19,637,240 barrels were produced from 86 wells in the area (Darton, 1933; Glass, 1953). Oil production here reached its final limits in the late 1940s with production from the Vicksburg on the south flank of the dome. In the 1950s, the field had produced 40 million barrels of oil with 107 wells producing 4,300 barrels per day and it was in advanced stage of depletion. The total oil production of the field prior to 1979 was recorded as 80 million barrels (Holzer and Bluntzer, 1984). According to Railroad Commission of Texas annual reports, the Pierce Junction salt dome produced 111,232 barrels of oil in 1997. However, the annual production decreased dramatically to 44,375 barrels in 2012. Annual production of the Pierce Junction oil field is depicted in Figure 2.5; gas production continued until 2000 and approximately 15 million cubic feet (Mcf) gas was produced from the field, as seen in Figure 2.6.

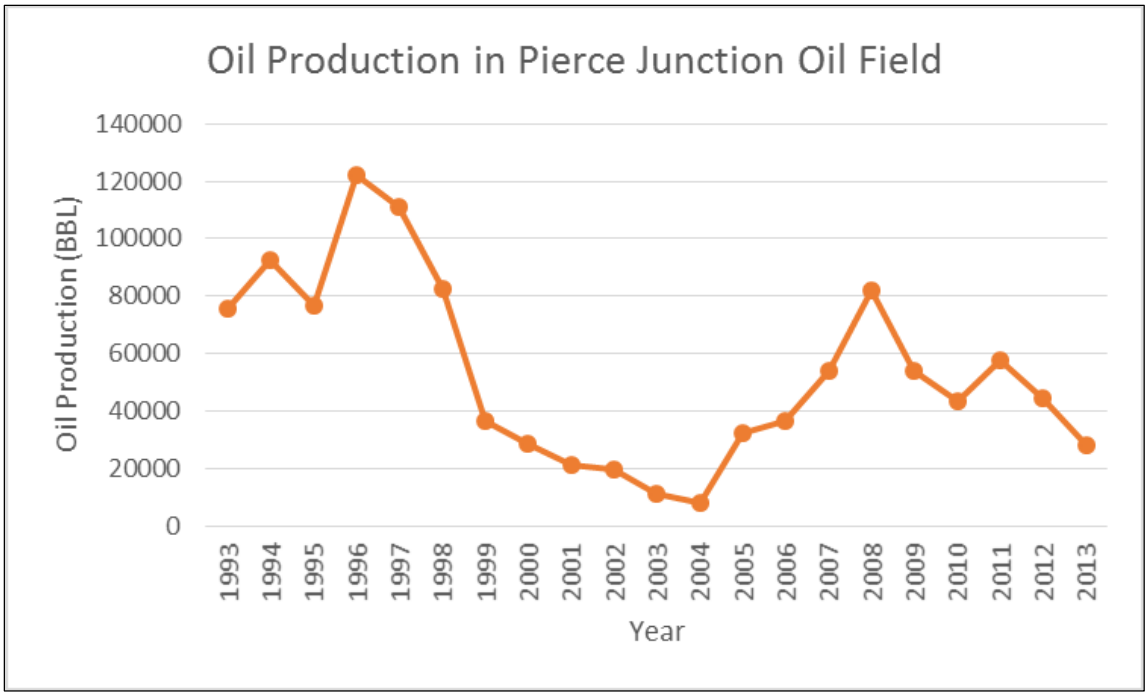

Figure 2.5. Oil production in Pierce Junction oil field (Railroad Commission of Texas, 2013).

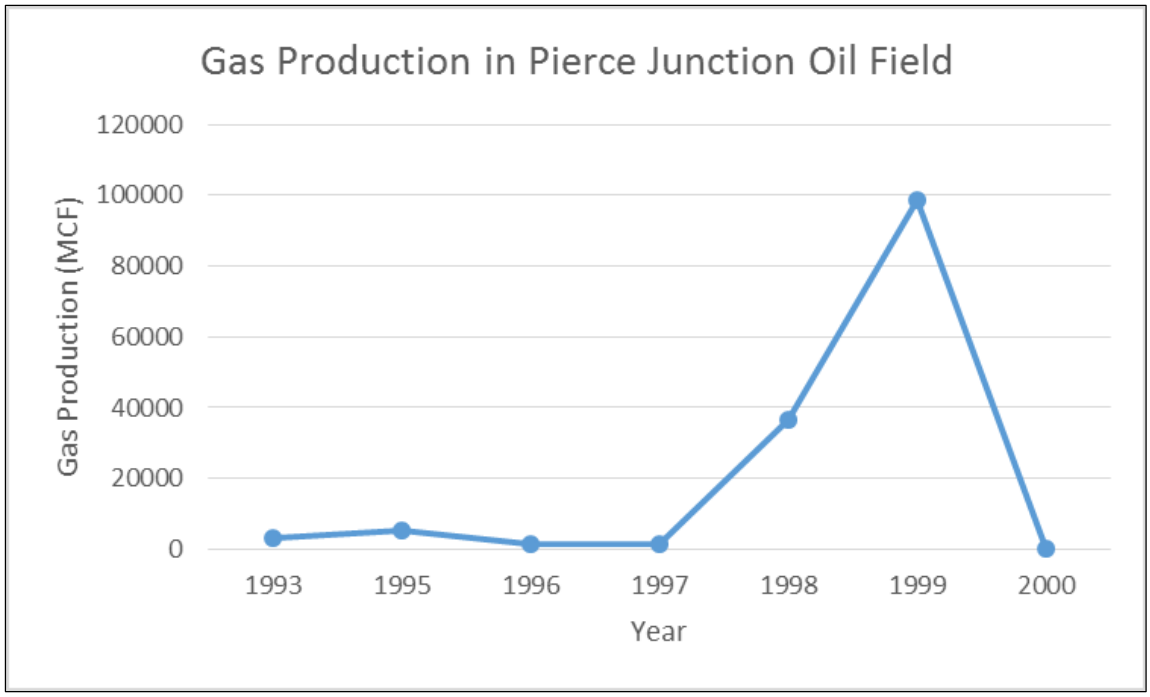

Figure 2.6. Gas production in Pierce Junction oil field (Railroad Commission of Texas, 2013).

Besides oil production, the Pierce Junction salt dome has been used for brine production and hydrocarbon storage over the last three decades. This field is the first facility where simultaneous brine production and hydrocarbon storage occured in Texas (Querio, 1974; Seni et al., 1984) Materials that do not dissolve salt can be stored in salt caverns securely, and brine production using controlled solution mining provides potential storage caverns in the salt dome (Thomas and Gehle, 2000). Texas Brine Company operates brine production, cavern construction and engineering, and management of storage facilities in the Pierce Junction salt dome.

2.2 Total Station Survey

Total Station is a modern electronic/optical surveying instrument that allows reading slope distances from the instrument to a particular point; it consists of a tripod, a distance measuring device, and a reflector prism (Figure 2.7).

A solid-state emitter within the Total Station generates an infrared laser signal. This laser signal is then reflected by reflector prism back to the measuring device. The distance between the Total Station and the reflector prism is calculated by an integrated computer that interprets the modulation pattern of the reflected signal. Most Total Station systems can determine the coordinates and elevation of a given point using simple trigonometry and triangulation equations. The data collected from Total Station survey are used to generate topographic maps of survey areas. Total Station surveys are preferred for detailed studies due to their very high accuracy (~1.5mm).

Figure 2.7. Elements of the Total Station survey instrument.

In 2011, Total Station survey data were collected at the boundaries of the Pierce Junction salt dome for static correction of seismic data. The survey was carried out every 5 m in the area where the seismic receivers were deployed (Figure 2.8). Average surface elevation in the area is about 19 m. Elevation difference between the beginning and end of the line was very small (about 2 meters). The elevation trend decreases slightly from north to south with a slope of about 2° (Figure 2.9).

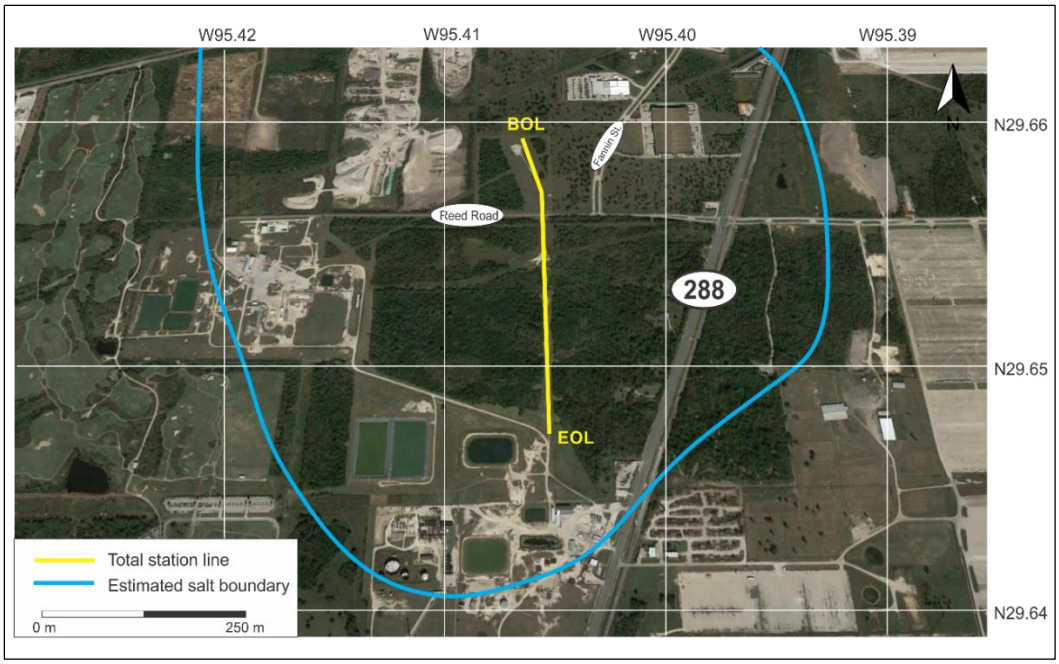

Figure 2.8. Map view of Total Station survey area. The yellow line represents the Total Station measurement line and blue line represents the estimated salt boundary (Huang, 2012).

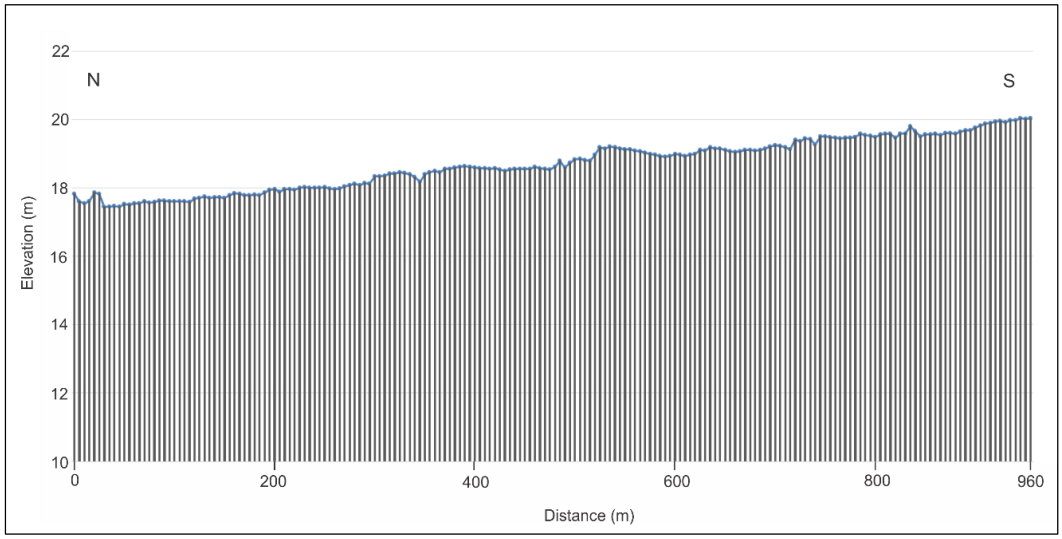

Figure 2.9. Elevation of N-S line in the center of the salt.

2.3 2-D Seismic Data

2.3.1 Seismic Data Acquisition

A 2-D seismic survey was conducted in the central part of the Pierce Junction salt dome in 2011, for the purpose of imaging the top of the salt on the same line of the Total Station survey (Figure 2.8). 120 vertical receivers were deployed at 5 m interval with a total length of 595 m. After shooting along the line, the receiver line was moved 360 m to the end so as to get total length of 955 m. AGL's MiniVibe seismic vibrator truck was used as the source. Sweep type was selected as linear from 10 to 120 MHz. Shots were fired between two receiver stations with 5 m intervals. The distance between source and receiver lines was kept at 5 m as much as possible. Figure 2.10 represents the receiver line and shot station configuration of this 2011 seismic survey in the Pierce Junction area.

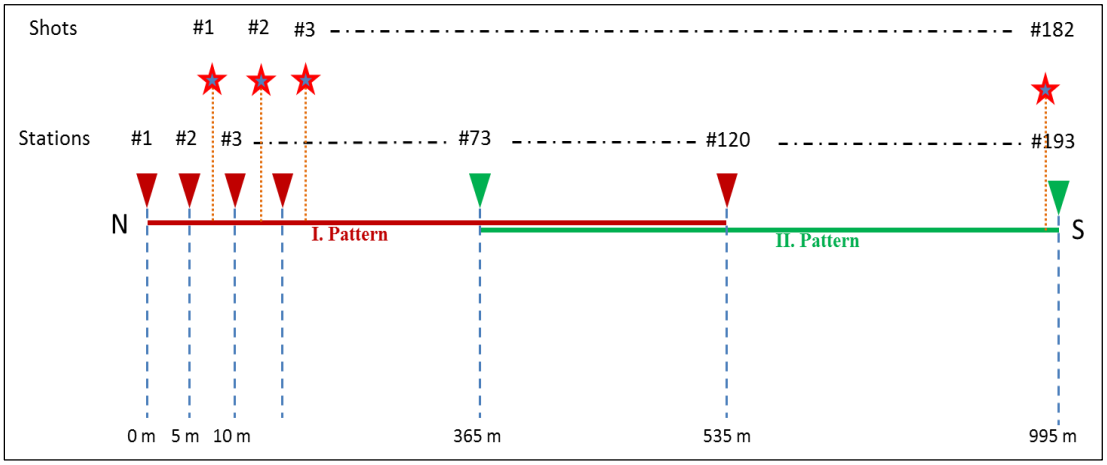

Figure 2.10. Shot and receiver configuration of 2-D seismic survey. Red and green triangles represent the stations of the first pattern, and second patterns, respectively. Red stars show shot locations.

2.3.2 Seismic Data Processing

Two-D seismic data from the Pierce Junction salt dome area were processed using Paradigm's Echos seismic processing software. The processing flow of seismic data is shown in Figure 2.11.

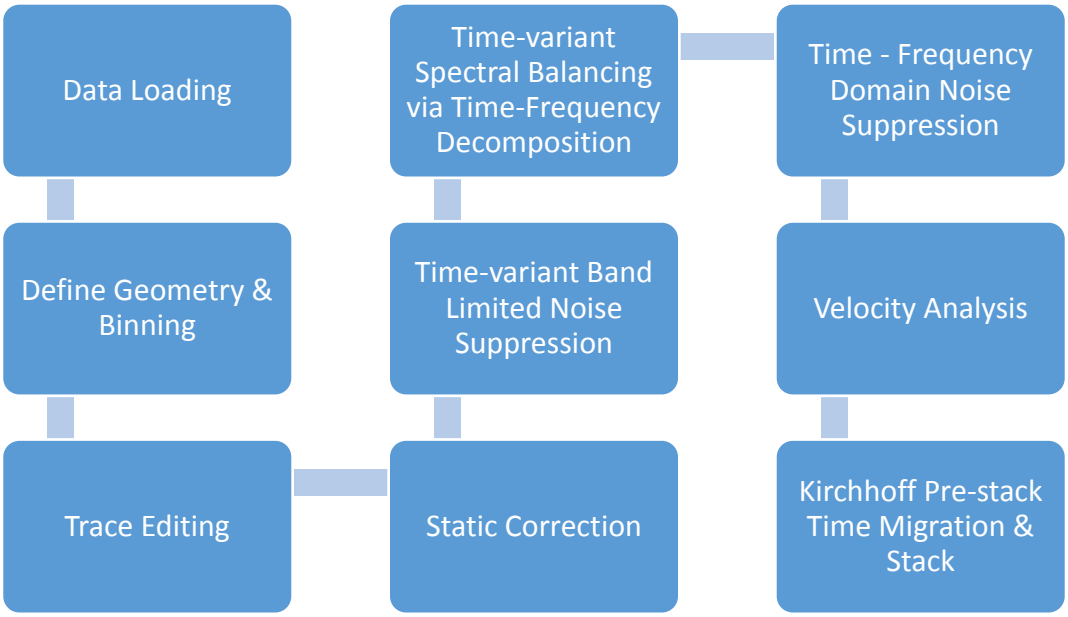

Figure 2.11. Processing work flow of Pierce Junction 2-D seismic data.

The collected data were first preprocessed using geometry loading, trace editing, and static correction. A series of noise suppression and filtering methods were also applied in order to eliminate low-frequency noise originating from producing wells and random sources.

First, time-variant band-limited noise suppression (SUPPRES module) with 3-20 Hz frequency band was applied to suppress organized type of noises, such as ground roll and air blast. In this method, noise and signal components in seismic traces are decomposed

using a 3-20 Hz Butterworth filter. Noise components of the trace are scaled down through comparison between noise and signal components, to have envelope match the specified signal envelope level. The final result is obtained by a summation of the original signal and scaled noise components (Oppenheim and Schafer, 1989; Robinson and Treitel, 1980; Taner et al., 1979)

Next, time-variant spectral balancing via time-frequency decomposition (TUNEUP module) was applied to the data. This method provides replacement of each input trace with the trace that has broader frequency band where the envelopes of the input and output traces are matched. Wavelet transforms using Gabor-Morlet wavelets yield the spectral extension of the trace (Goupillaud et al., 1984; Morlet et al., 1982; Partyka et al., 1999). The power spectrum of a shot gather before and after time-variant spectral balancing is shown in Figure 2.12.

Finally, time-frequency domain noise suppression (TFCLEAN module) was used to eliminate the noise bursts in gathers. This application uses Fast Fourier Transforms to transform the input gather into a time-frequency domain, to split input gather into its amplitude and phase components, and to decompose it into different sub-bands. A noise threshold, calculated automatically by median of frequency sub-bands, is used to scale the noises whose spectral amplitude value exceeds the threshold within the sub-band. Subsequently, unaltered phase information is combined with both scaled and unscaled amplitude information and transformed into filtered time-space domain by an inverse Fourier Transform. As a result of sample-by-sample noise suppression on various

frequency components, nicely balanced spectra are obtained (Goupillaud et al., 1983; Morlet et al., 1982; Partyka et al., 1999; Taner et al., 1979).

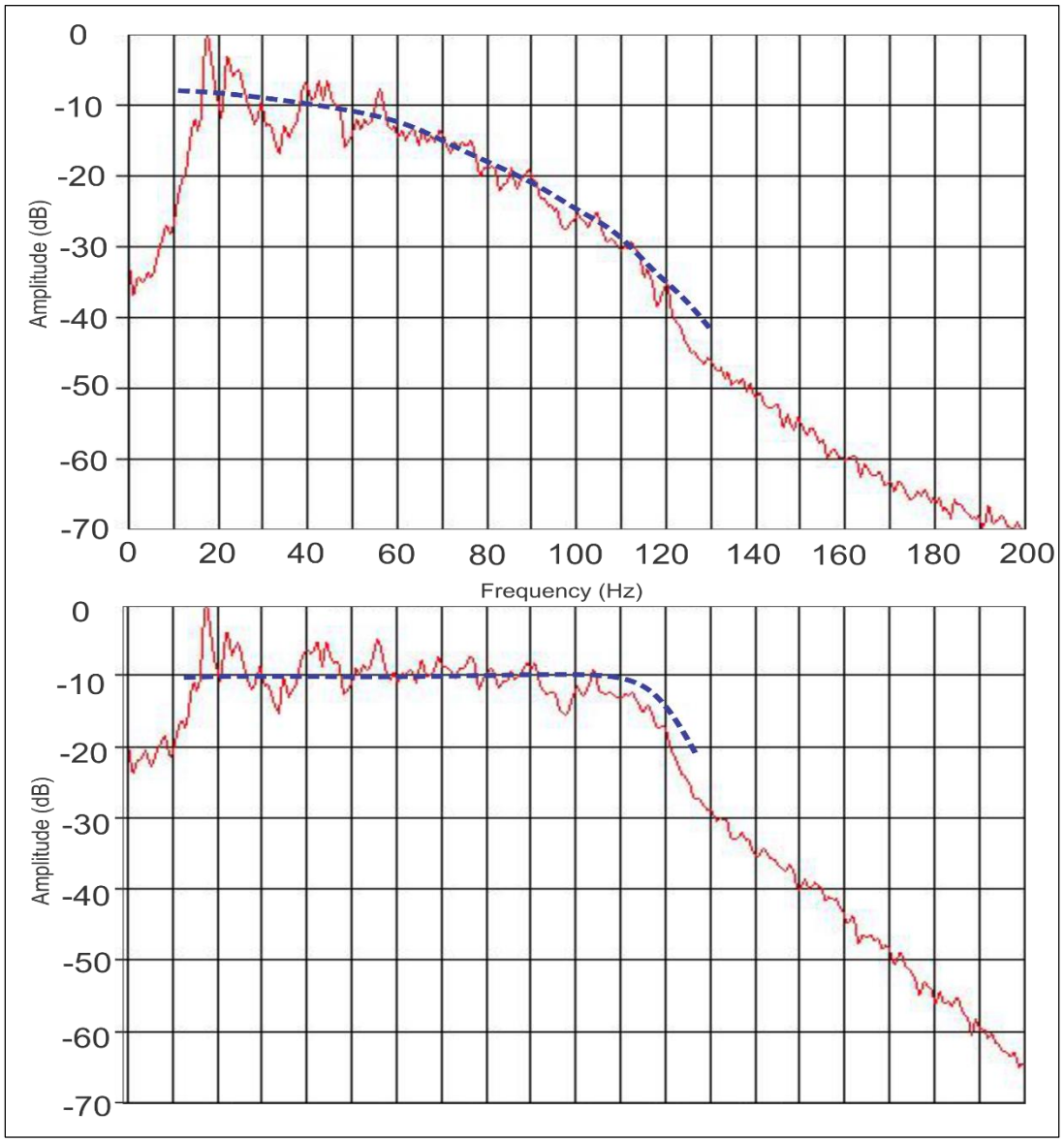

Figure 2.12. Average power spectrum of shot gather No.51 before and after time-variant spectral balancing. Above, before time-variant spectral balancing, the amplitude decreases with increasing frequencies. Below, after time-variant spectral balancing, the amplitude stays at the same high amplitude value with increasing frequencies. The blue dashed-line represents the amplitude trend with increasing frequencies.

In addition to the noise suppression methods already mentioned, surface-consistent amplitude balancing, predictive deconvolution, ensemble equalization, F-K filtering, low-frequency array filtering, and surface-consistent deconvolution techniques were also applied. However, as reasonable results could not be observed on shot gathers, these techniques were not used in the final processing flow.

Comparison of raw and noise suppressed shot gathers of the 1st and 55th shots are shown in Figures 2.13 and 2.14, respectively. Strong ground roll, air blast, and low frequency surface consistent noise in raw shot gathers were suppressed by the methods mentioned in this sub-section. These noise suppression methods increased the resolution and enhanced the possible reflections.

Root-mean-square (RMS) velocity function was determined through detailed velocity analysis and used in a Kirchhoff pre-stack time migration (Figure 2.15). Final Kirchhoff pre-stack time migrated and stacked sections are shown in Figure 2.16.

2.3.3 Seismic Interpretation

The final stack of the data showed a reflector having stacking velocities about 2000 m/s, which is reasonable for a “salt reflector”. This reflection was observed at 290 ms, which corresponds to about a 290 m depth with a 2000 m/s stacking velocity. Another reflector, comparatively weaker than a “salt reflector”, had a velocity of ~1950 m/s, and was observed at 210 ms, corresponding to a 205 m depth. This reflector was interpreted

as a “cap rock reflector” (Figure 2.17). Reflector depths obtained from seismic data match the cap rock and salt depth information from previous studies in the area.

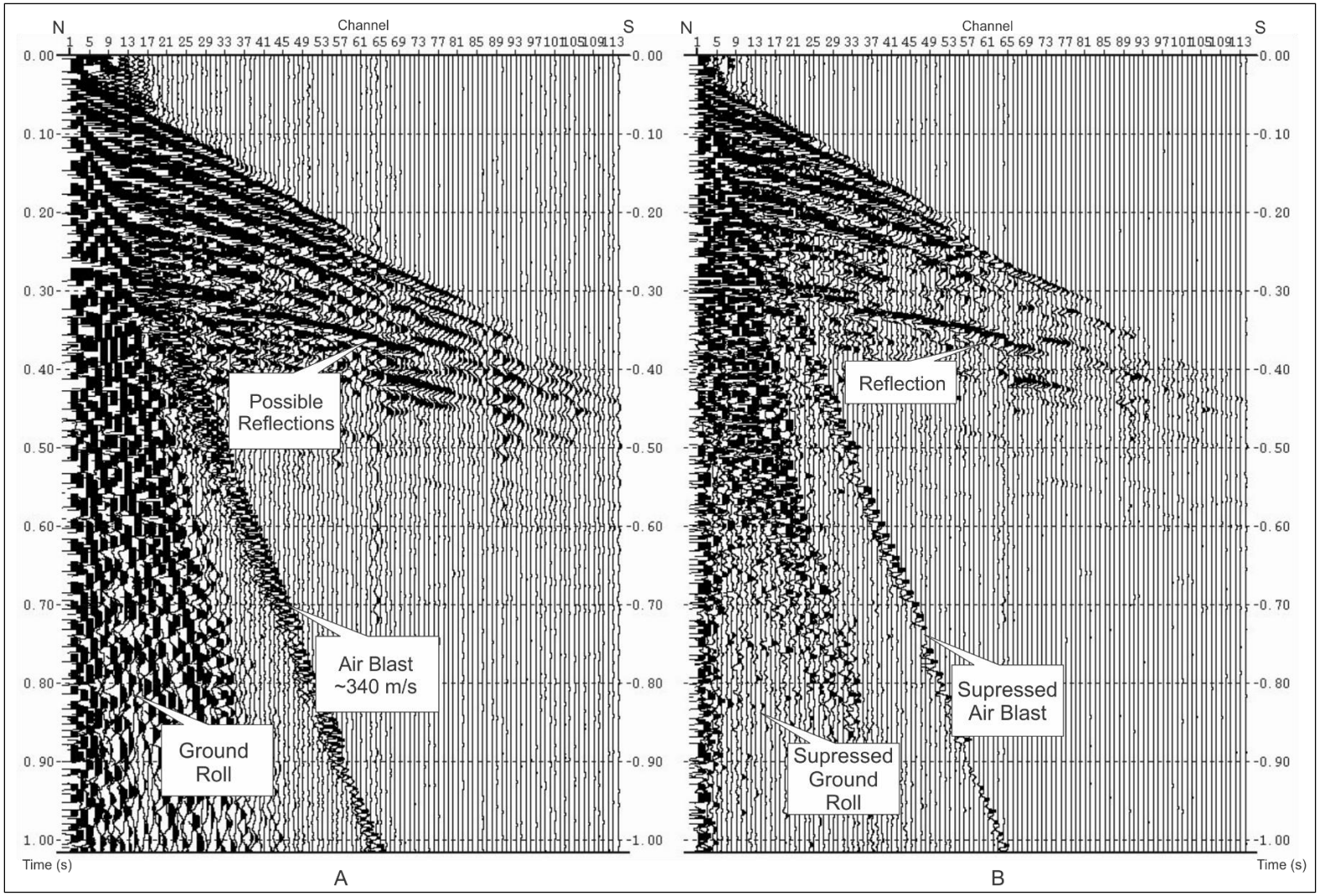

Figure 2.13. Comparison of raw (A) and processed (B) shot gathers of the 1st shot.

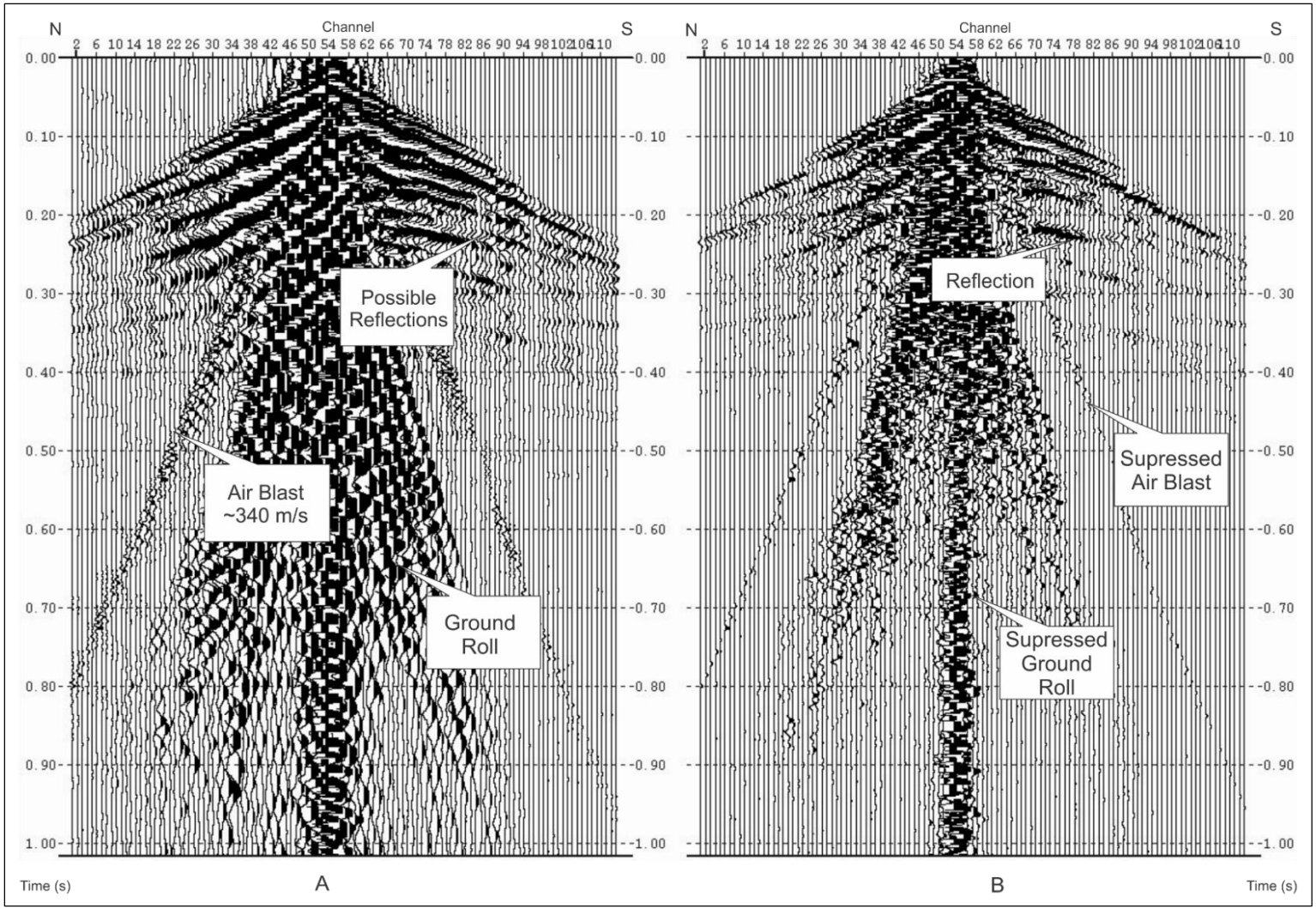

Figure 2.14. Comparison of raw (A) and processed (B) shot gathers of the 55st shot.

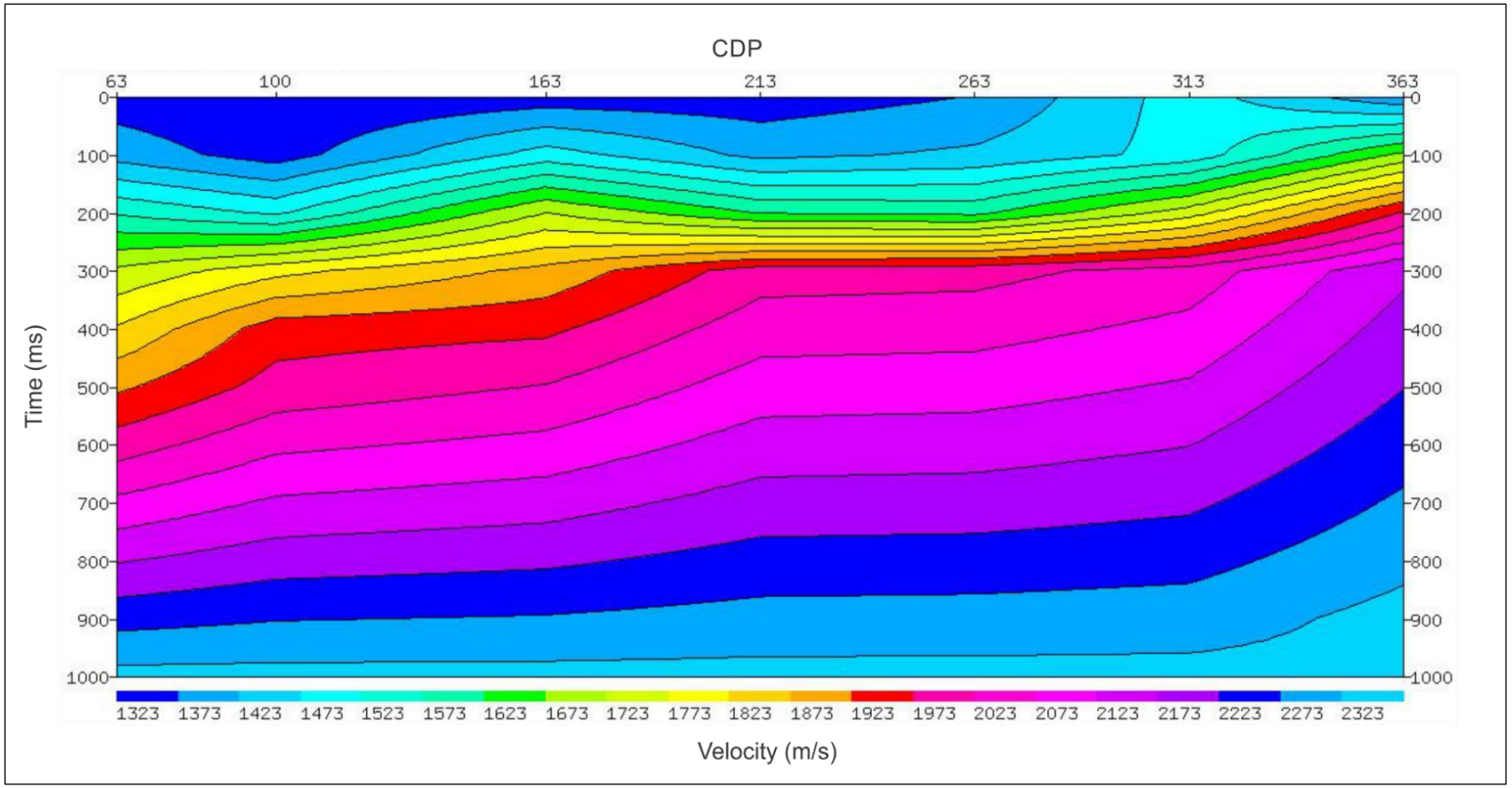

Figure 2.15. RMS velocity model used in pre-stack Kirchhoff time migration.

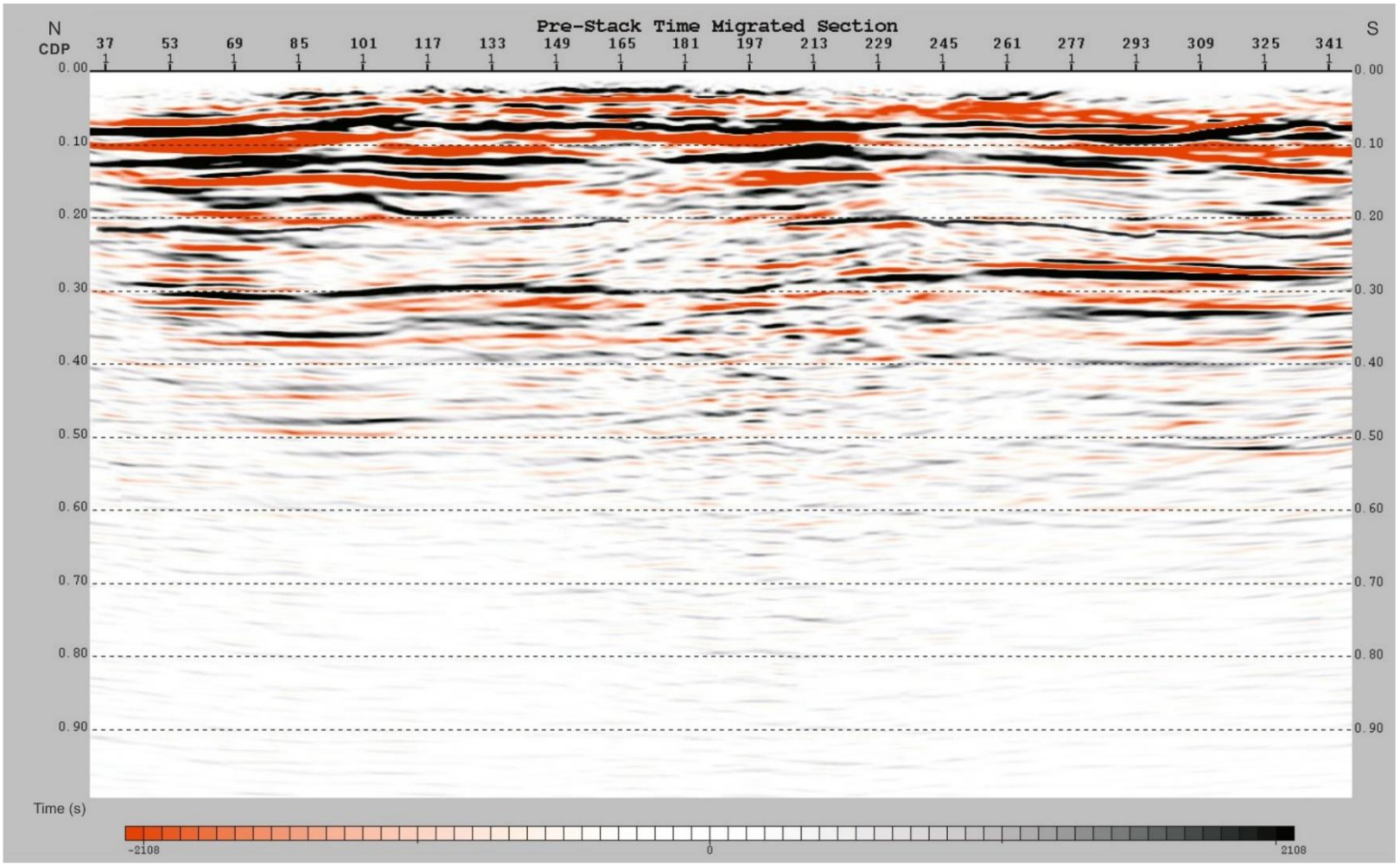

Figure 2.16. Final pre-stack Kirchhoff time migrated image. The color scale indicates the amplitude.

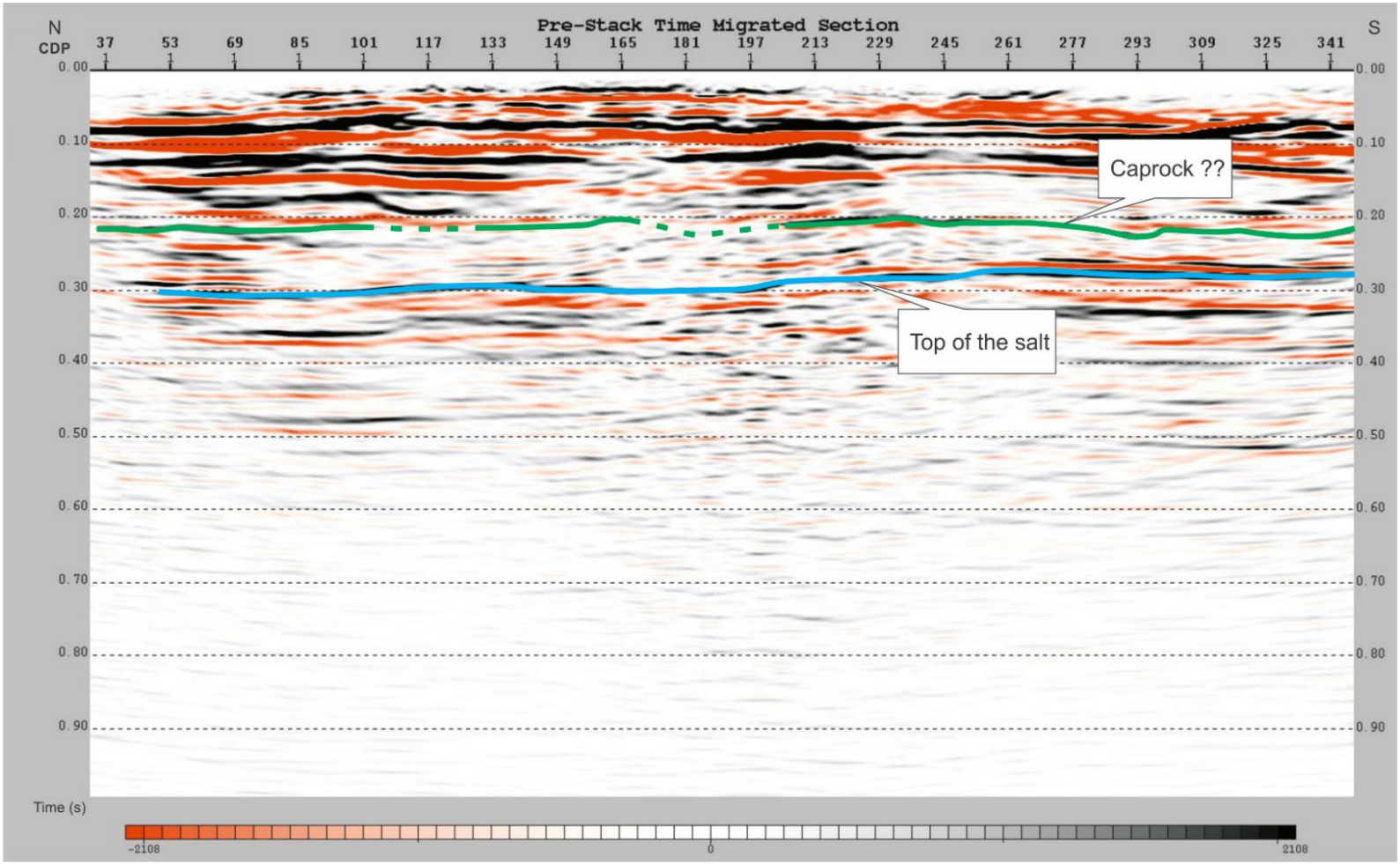

Figure 2.17. Interpreted pre-stack Kirchhoff time migrated image. The reflection, which is highlighted with a blue line, is interpreted as the top of the salt, and the horizon, which is highlighted with a green line and a green dashed line, is interpreted as cap rock. The color scale indicates the amplitude.

2.4 Gravity Modeling

The gravity method is an effective geophysical technique to reveal the subsurface structure. This method allows the area of interest to be modelled using the gravitational field variations caused by differences in the distribution of densities, and therefore distribution of rock types (Sheriff, 2002).

2.4.1 Gravity Data Acquisition

A 2-D gravity survey was carried out over the Pierce Junction salt dome in 2013 The objective of the survey was to model the gravity data and obtain a north-south cross-section of the salt dome, in addition to the east-west cross-section drawn by Glass (1953). However, due to permission issues and geographical limitations, the survey was carried out along Almeda Road. Hence, the data were collected along a southwest-northeast trending (18^{o}) profile. The total length of the profile was 7600 m with 200 m station intervals (Figure 2.18). AGL's Scintrex CG-5 Autograv gravimeter, Garmin GPS, distance measurement tools, and safety equipment were used during the data acquisition. The graph of the raw gravity data is shown in Figure 2.19.

Figure 2.18. Location of the gravity survey. The blue area represents the estimated top of the salt boundary (modified after Huang, 2012).

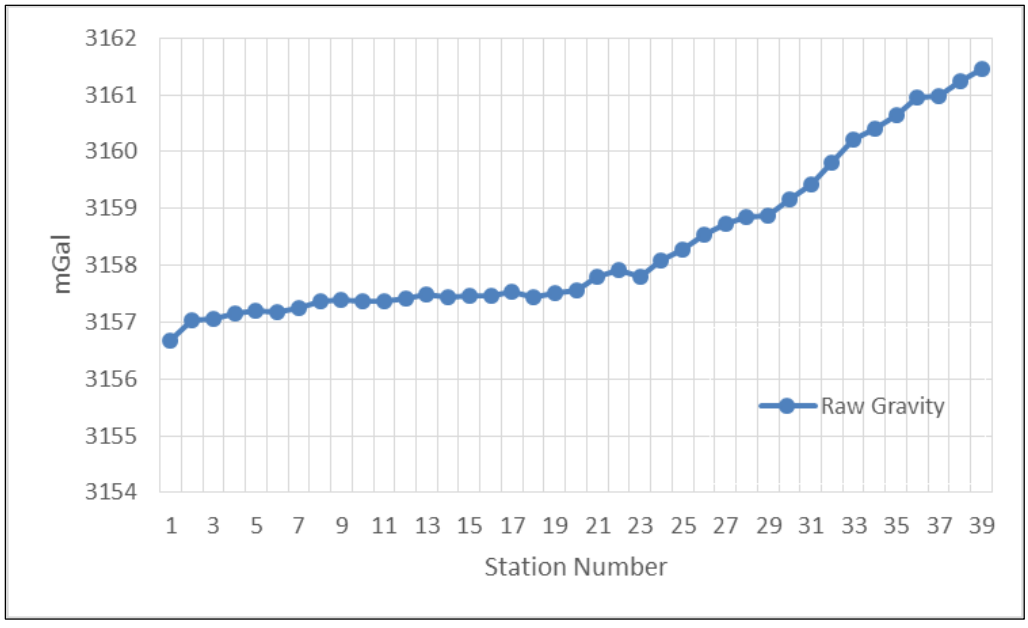

Figure 2.19. The graph of the raw gravity data of SW-NE line.

2.4.2 Gravity Data Processing

Density differences in subsurface lithology cause small gravity variations. These small anomalies can be observed after removing the temporal and spatial effects from the data (Boyd, 2003; Otoum, 2011; Seigel, 1995). Drift and tide corrections were applied to eliminate the time-varying effects caused by instrumental drift and tidal effects. Spatial corrections consisted of latitude, free-air, Bouguer, and terrain corrections. The elliptical shape and rotation of the earth cause variations in the gravity field based on location of the measurements (Nettleton, 1976). In order to avoid this effect, latitude correction was made employing the following Moritz (1992) equation (Eq. 2.1):

$$\boldsymbol{G_n = 9780327\left(1.0 + 0.0053024\, sin^2(\theta) - 0.0000058\, sin^2(2\theta)\right)} \quad \text{Eq. 2.1}$$

where:

G_n = gravity normal in mGal after latitude correction, and

Θ = latitude of the measurement location in decimal degrees.

Gravity measurements are also affected by the elevation of the measurement location (Nettleton, 1976). As data are collected at different distances from the center of the earth than that of the datum, free-air correction is required (Sheriff, 2002). Free-air correction was defined by the following equations:

$$G_f = G_o - G_n + \Delta G_f \quad \text{, and} \qquad \text{Eq. 2.2}$$

$$\Delta G_f = \pm 0.3086h \quad , \qquad \text{Eq. 2.3}$$

where:

G_f = free-air corrected gravity reading in mGal,

G_o = raw observed measurement in mGal,

ΔG_f = free-air correction in mGal, and

h = elevation in meters.

If the measurement location is above sea level, free-air correction will be positive; otherwise, free-air correction will be negative.

The attraction of the rock between the station and the elevation of the datum causes another effect on gravity data. The Bouguer correction was applied to eliminate this kind of effect by using the density of the intervening rock and the elevation (Sheriff, 2011). The Bouguer correction is defined by the following equation:

$$G_B = 0.04192\rho h \quad , \qquad \text{Eq. 2.4}$$

where:

G_B = Bouguer correction in mGal ,

ρ = bulk density of the overburden in grams per cubic centimeter, and

h = elevation in meters.

The equations for latitude, free-air, and Bouguer corrections were implemented using Microsoft Excel and calculated for known parameters. Subsequently, results obtained from free-air and Bouguer corrections were used as inputs for the modelling step. The elevation values of the gravity stations used in free-air and Bouguer corrections were extracted from GPS data. For each station, elevation was measured at least three times and the average of these measurements was used as the input parameter.

2.4.3 Forward Modeling and Interpretation

Bouguer anomaly data were modelled using GEOSOFT Oasis Montaj software. Typical gravity anomalies of salt domes vary due to depth of the structures. A shallow Gulf Coast salt dome should produce a gravity difference between 0-2 mGal (Prieto, 2000). As expected, the Pierce Junction salt dome produces about a 1 mGal difference from its surrounding material. In general, these anomalies increase in amplitude and sharpness (frequency). But it is also possible to observe smaller anomalies due to positive anomaly superimposition that is caused by the faulting activity around the salt and cap rock.

Typical Gulf Coast sediment densities were used in the modelling stage (Prieto, 2000) (Table 2.1). The data were modelled for a 4000 m depth, which is about a half-length of the data profile. As control points for modeling, we used depths of the surrounding sediments, the top of the salt, and the overlying cap rock found in by well logs around the salt dome on east-west cross-section of our study area.

Table 2.1. Layers and densities used in gravity modeling.

Layer	Density (g/cm^3)
Salt	2.20
Caprock	2.60
Miocene	2.25
Frio	2.35
Vicksburg	2.43
Yegua	2.50

The gravity profile was located in the eastern part of the salt dome. The expected diameter of the top of the salt is about 1.2 km, but as the profile does not cross over the center of the salt dome, it was modelled as 800 m. Also, the thickness of the cap rock varies and becomes thinner on the sides of the salt dome (Figure 2.20). Besides the anomaly that is interpreted as the salt dome, there are two gravity variations at the north and south ends of the profile. These variations could be caused by faulting activity, dramatic changes in sedimentary thickness, salt dome rooting, and tilting in N-S direction.

As a result, the modelled gravity data show that the extension of the salt dome in north-south direction is in the expected boundary. However, this gravity profile is not precise enough to interpret the shape and size of the salt dome.

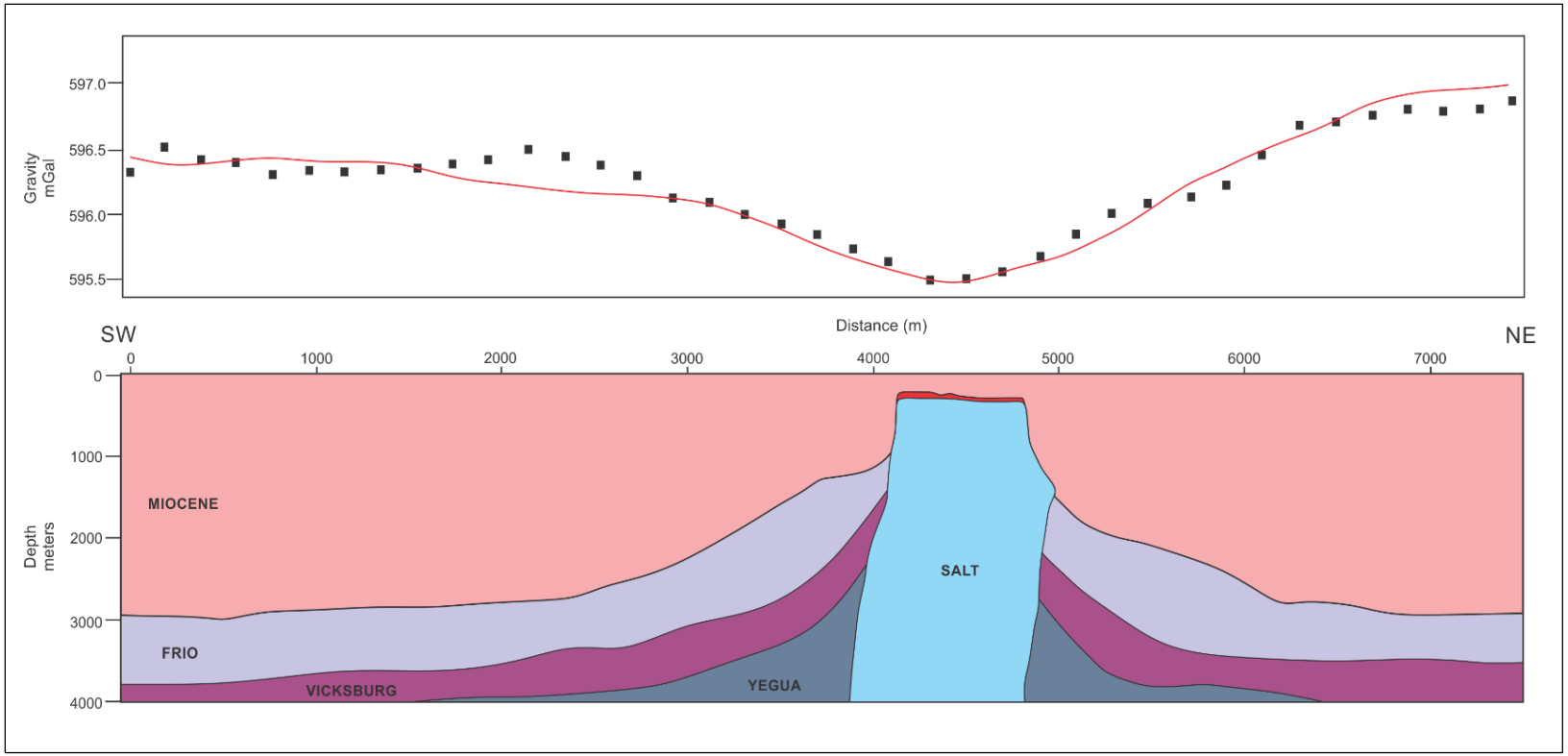

Figure 2.20. Gravity model of SW-NE profile. Black dots and the red line represent observed and calculated gravity, respectively. Vertical exaggeration of model is 0.5.

CHAPTER THREE: ACQUISITION MODELING FOR THE PIERCE JUNCTION SALT DOME

3.1 Velocity Models

Two-D and 3-D velocity models were built using GEDCO (Geophysical Exploration and Development Co.) OMNI 3D Survey Design software.

First, a 2-D velocity model of the east-west cross-section of the salt dome was created. The extent of the model was set to 16 km in order to provide sufficient space in survey design analyses. Geological cross-sections from well logs, other examples, 2-D seismic data, and gravity data were used to obtain the 2-D velocity model. According to previous studies, the Pierce Junction area consists of four main sedimentary layers along with the salt dome and overlying cap rock (Glass, 1953). These sedimentary layers are the Miocene, Frio, Vicksburg, and Yegua (Figure 2.3).

Average P-wave interval velocities of the Vicksburg, Frio, and Yegua layers were adapted from the previous studies of Ewing et al. (1983), Parra and Collier (1997), and Bain (2010). The interval velocities of the cap rock layer and the shallowest part of the near-surface layer were calculated as 2200 m/s and 1800 m/s, respectively, using the RMS velocities from the original 2-D seismic data. Velocities within the Miocene layer were separated into six constant velocity sub-layers to create a velocity gradient within the layer. Interval velocity gradients within the Miocene layer were adapted from Lash (1980), and show P-wave velocity gradients within the Miocene layer in Gulf Coast sediments (Figure 3.1). The P-wave velocity of the salt was assigned as 4500 m/s, which is the

average velocity used in many seismic modeling studies (Jiao et al, 2012; Oezsen, 2004; Willis et al., 2006). Final 2-D interval velocity and RMS velocity models are shown in Figures 3.2 and 3.3, respectively.

S-wave velocities were calculated using V_p/V_s= 2.37, which is the common ratio for the Gulf Coast sediments recommended by Castagna et al. (1985). Properties of each layer within the model are given in Table 3.1.

Table 3.1. Properties of layers in 2-D model.

Layer	P-wave Interval Velocity (V_p) m/s	S-wave Interval Velocity (V_s) m/s	V_p/V_s
Miocene	1800 - 2500	600-1000	3.0-2.5
Frio	3000	1265.8	2.37
Vicksburg	3300	1319	2.37
Yegua	3600	1519	2.37
Salt	4500	2.250	2
Caprock	2200	1100	2

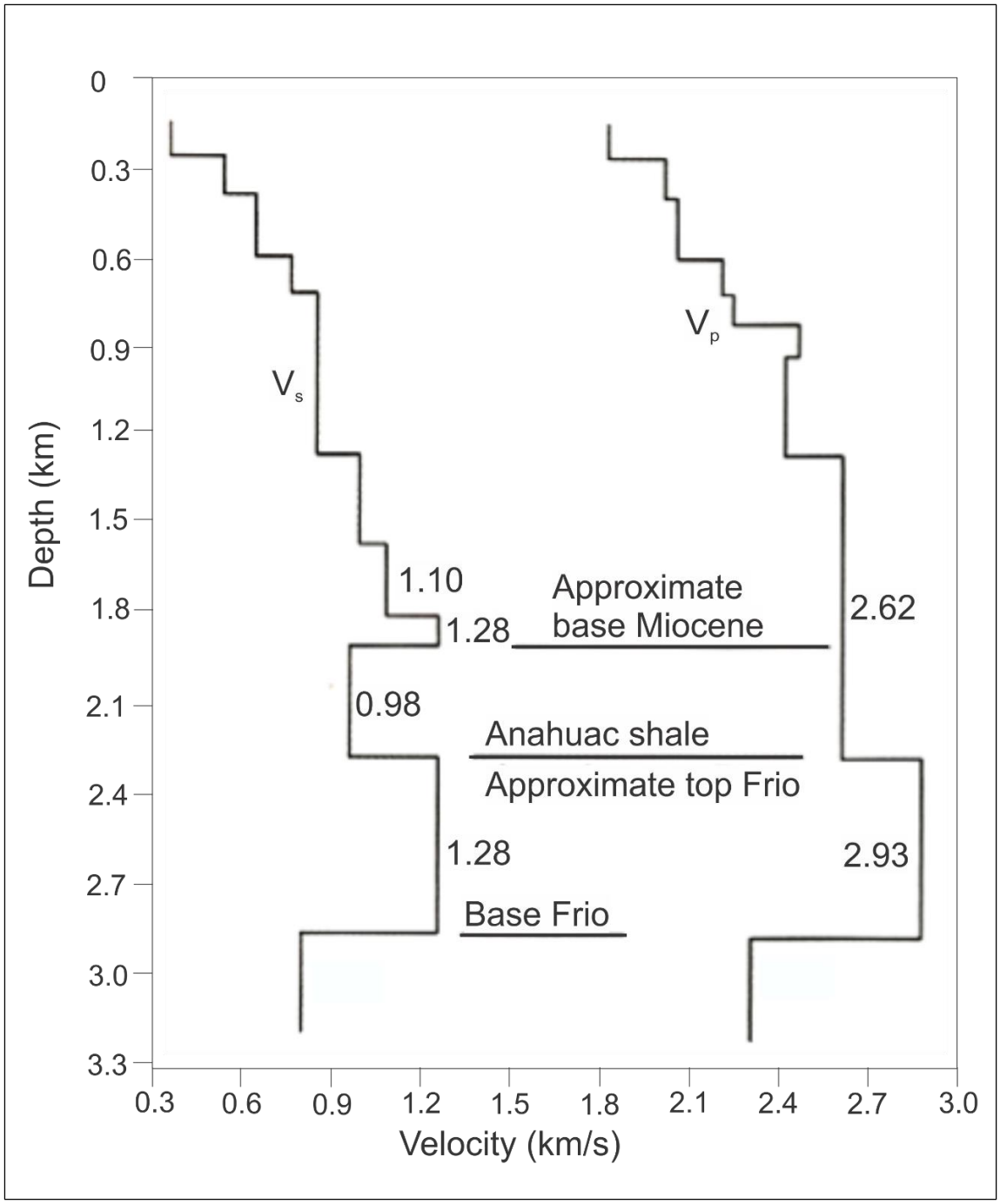

Figure 3.1. P-wave and S-wave velocities within the Miocene layer for Gulf Coast sediments (modified after Lash, 1980).

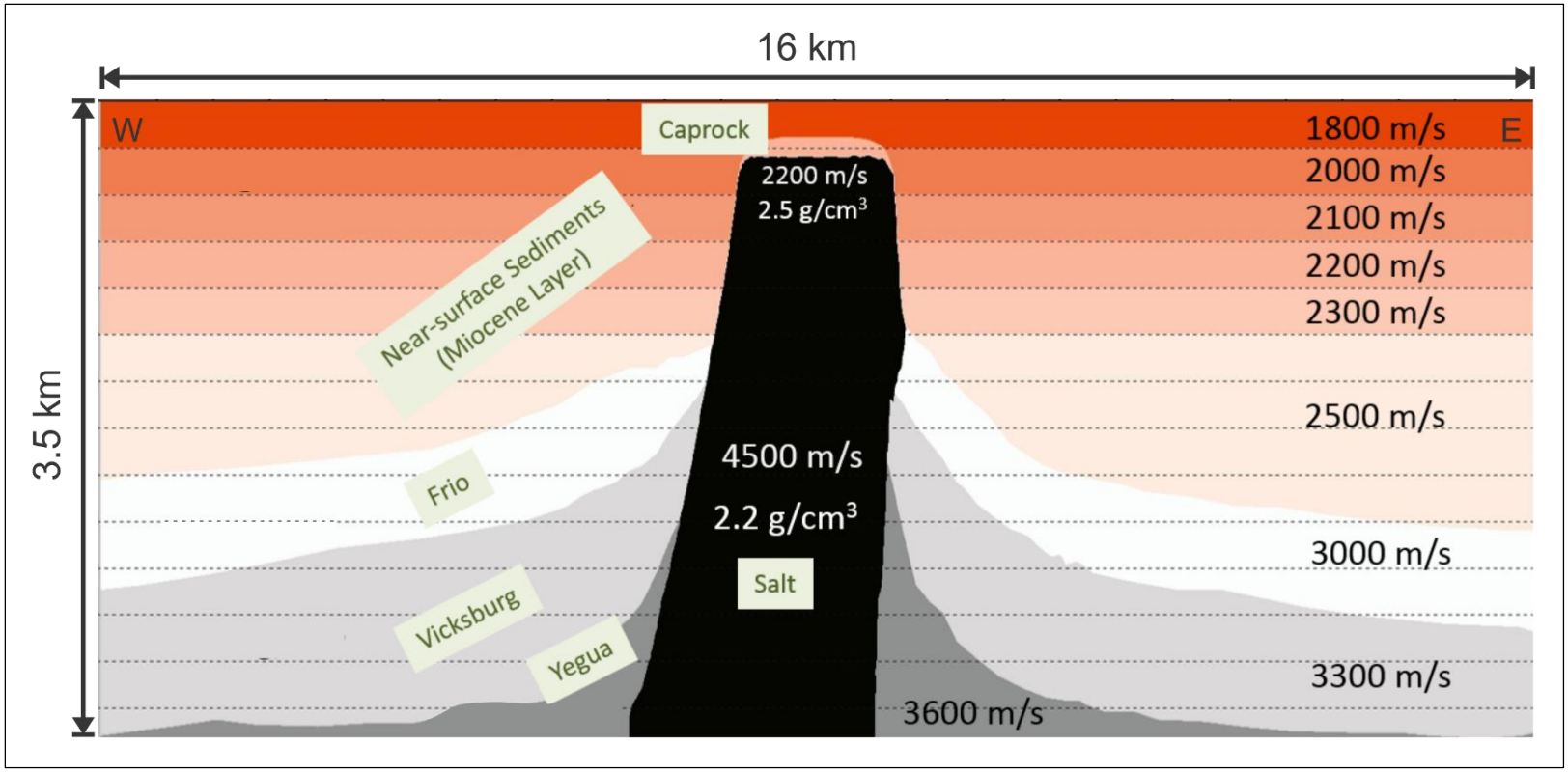

Figure 3.2. Final 2-D interval velocity model of the Pierce Junction salt dome.

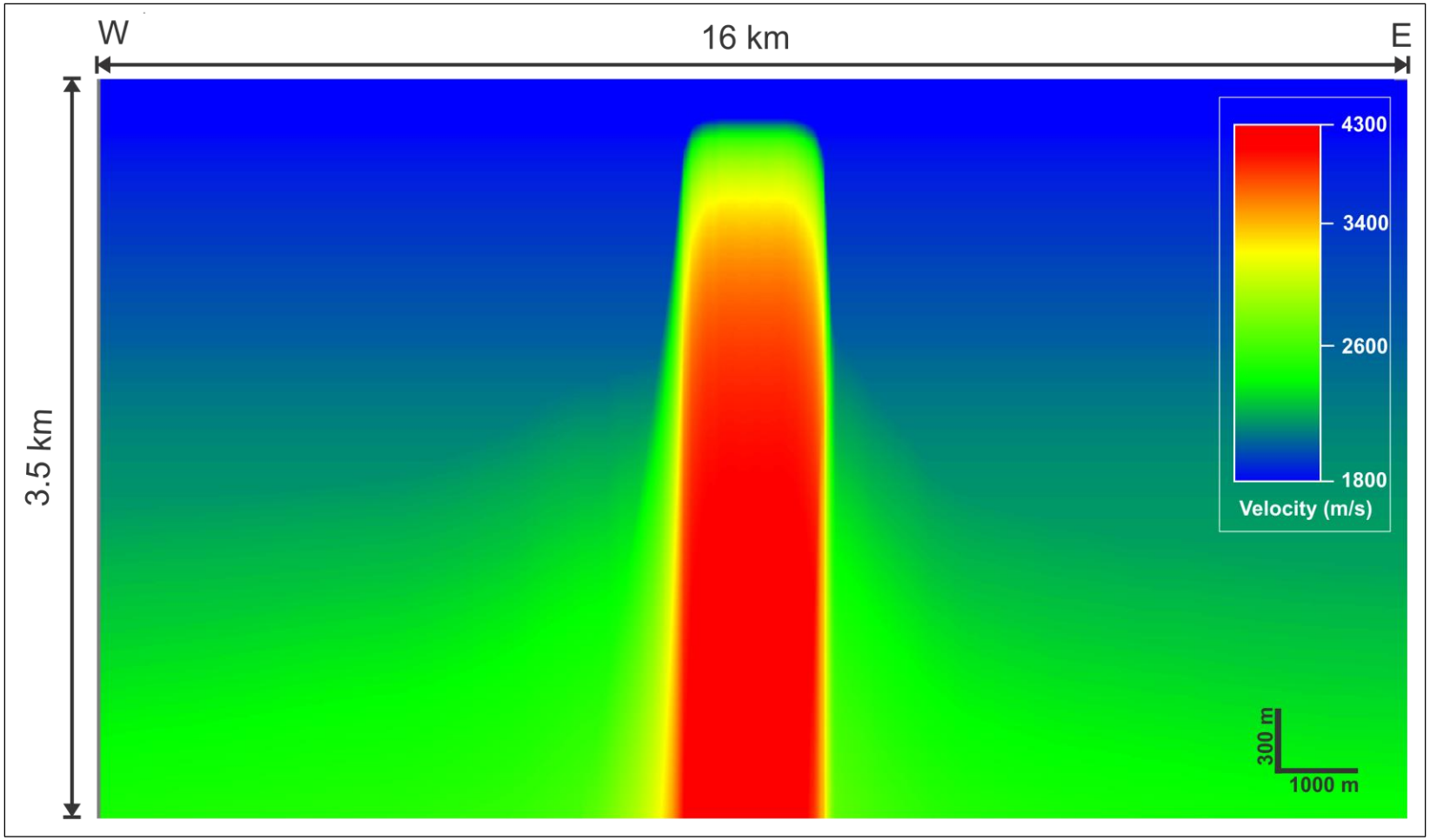

Figure 3.3. Final 2-D RMS velocity model of the Pierce Junction salt dome.

Every set of geological and geophysical data from the study area contributed valuable information for building an accurate 3-D velocity model. In this study, a circular piercement salt dome shape was built using the dimensions of the dome in an east-west cross-section. A coordinate transformation was applied to the eastern half of the 2-D model, and then rotated 360° from the center with a 1° interval, to obtain 3-D horizons of sedimentary layers (Figure 3.4). Unlike the horizontal Miocene layers in the 2-D velocity model, the Miocene layer for the 3-D model was separated into three layers with angles of 5°, 10°, and 15° so as to understand the effect of the dipping layers at different angles to the acquisition and imaging. Consequently, a volume with dimensions of 16x16x3.5 km that represents the salt dome and surrounding area was created for 3-D survey design analyses and modeling purposes. The resulting in-line/cross-line representation and the 3-D chair diagram of the model imaged by Paradigm 3-D Canvas software are shown in Figures 3.5 and 3.6, respectively.

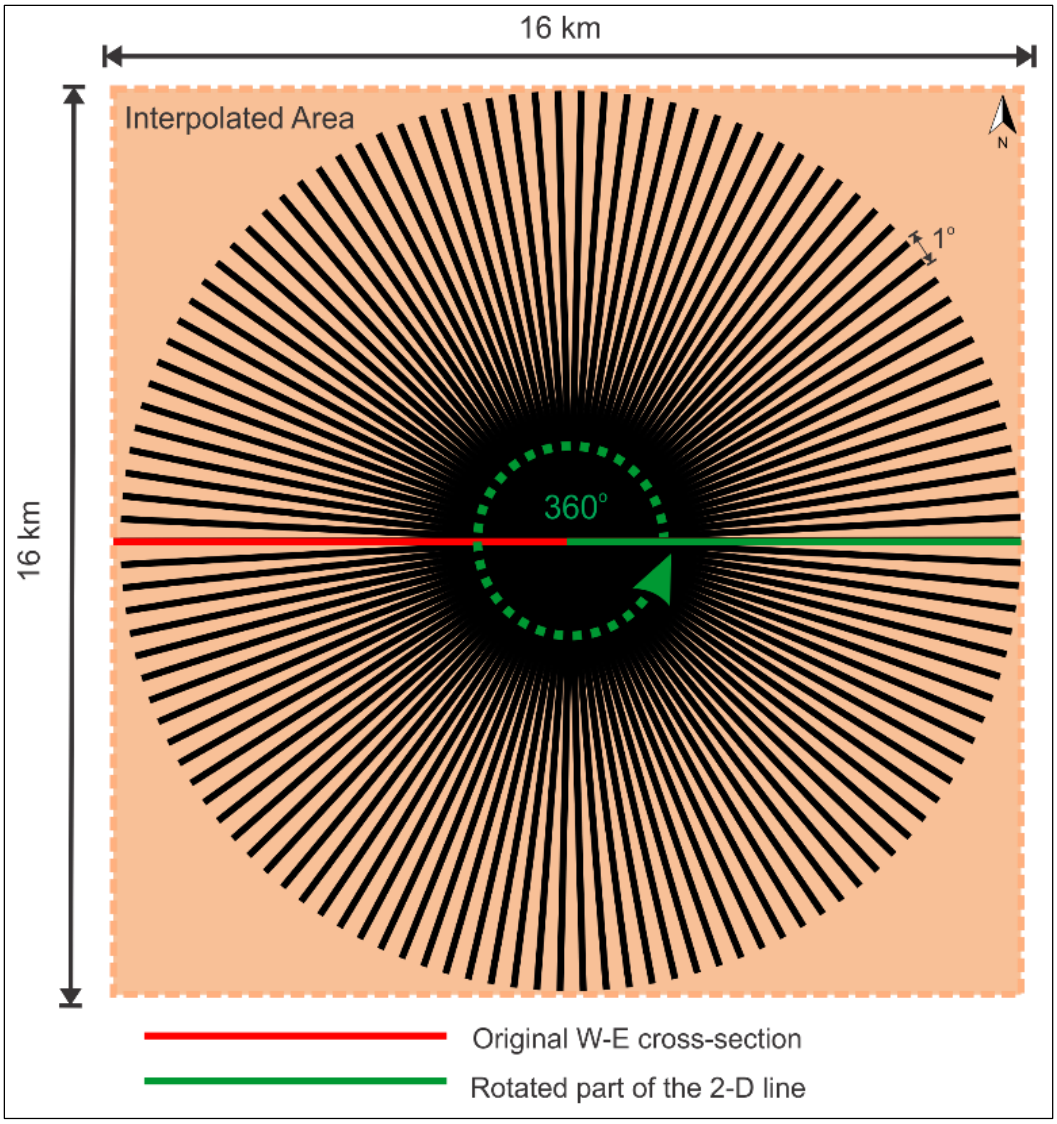

Figure 3.4. The method used to obtain 3-D horizons by rotating the original 2-D W-E Cross-section.

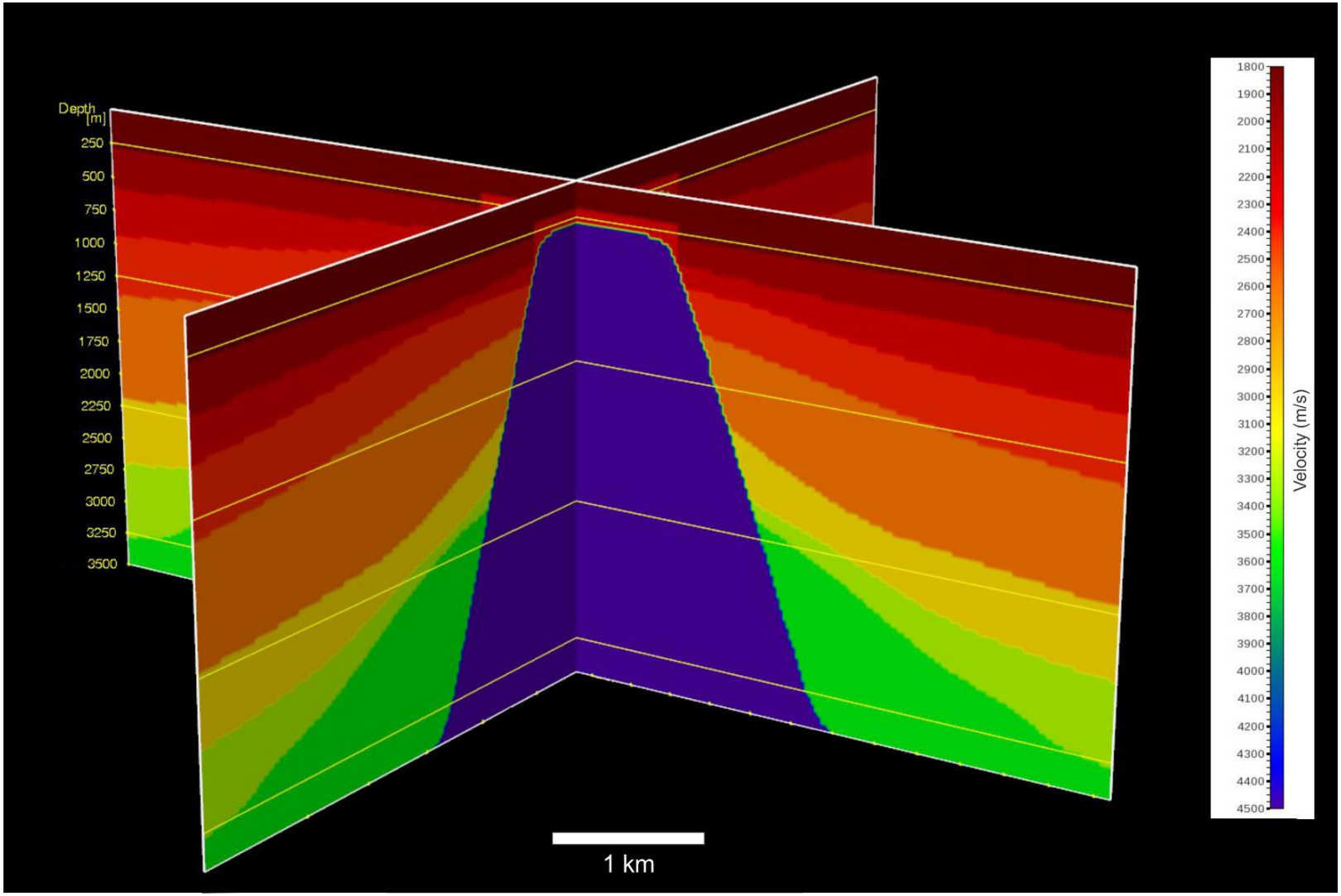

Figure 3.5. In-line/Cross-line representation of 3-D velocity model of the Pierce Junction salt dome area.

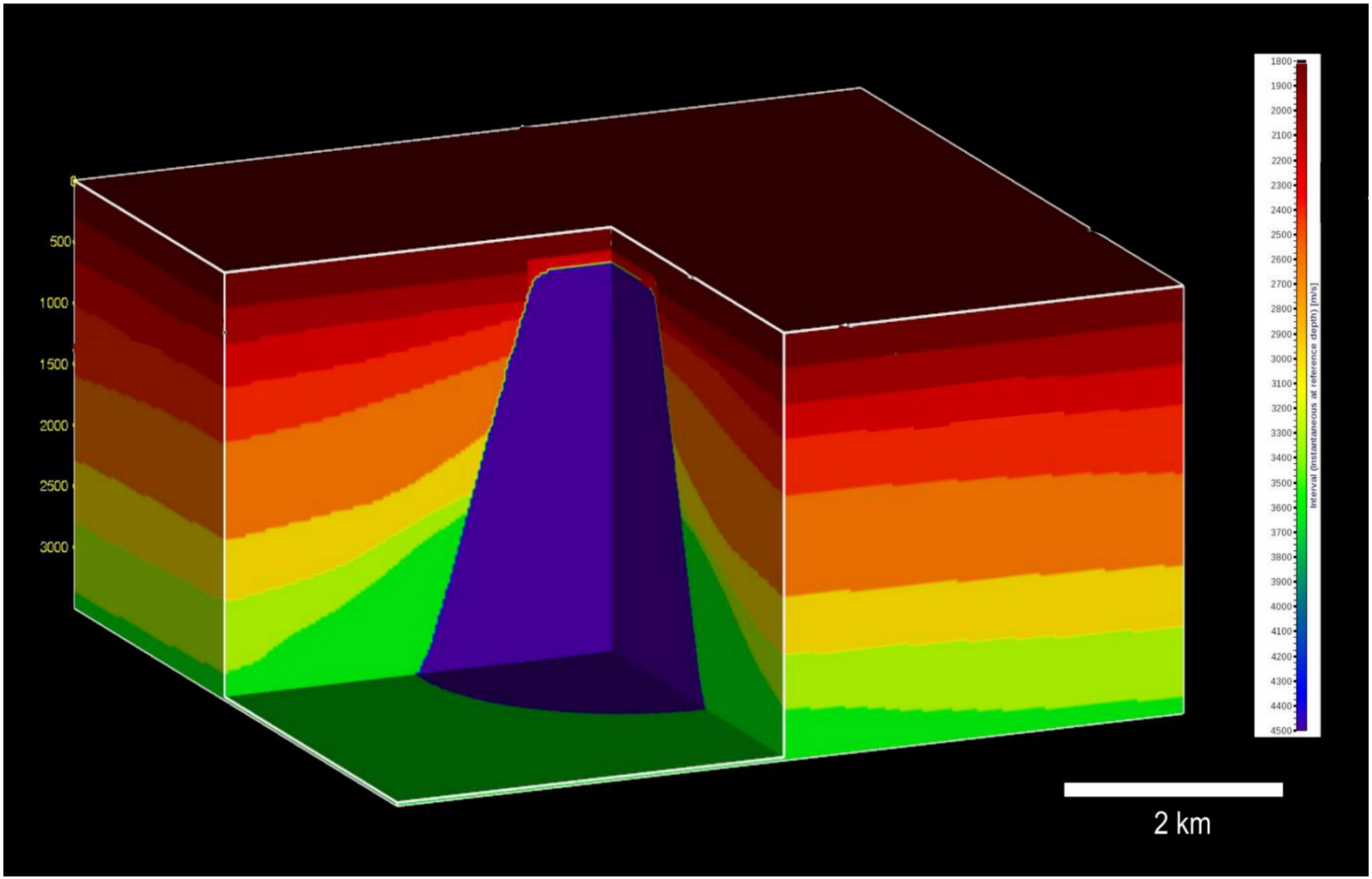

Figure 3.6. Chair diagram of 3-D velocity model of the Pierce Junction salt dome area.

3.2 Two-D Seismic Survey Design via Modeling and RTM Imaging

3.2.1 Fundamentals of 2-D Seismic Survey Design

Over the last century, 2-D seismic data acquisition has been one of the most effective geophysical methods allowing us to delineate subsurface geology. Two-D seismic surveying has kept its popularity through the years, even though it is being replaced with 3-D seismic surveys. Two-D surveys have been commonly implemented as a cost-effective method to provide information for 3-D survey design projects. The most important criterion in 2-D seismic survey design is optimizing cost and time while imaging the targets in as much detail as possible.

3.2.1.1 Description of Important Subsurface Elements

Definition of the horizons in the survey area provides important information for determining the survey parameters, such as offset range, source frequency, sample rate, subsurface coverage, and resolution.

As shown in Figure 3.7, horizon definition can be given by four important layers: (1) near-surface layer, (2) shallow horizon, (3) target layer, and (4) deep horizon (Stone, 1994). Existing well logs, seismic data, and check shot information can be used to approximate velocity and maximum dip determination. Each layer has distinct importance when considering survey parameters. Modeling of these layers using depth, average velocity, and time information usually assures that the designed survey will meet imaging requirements.

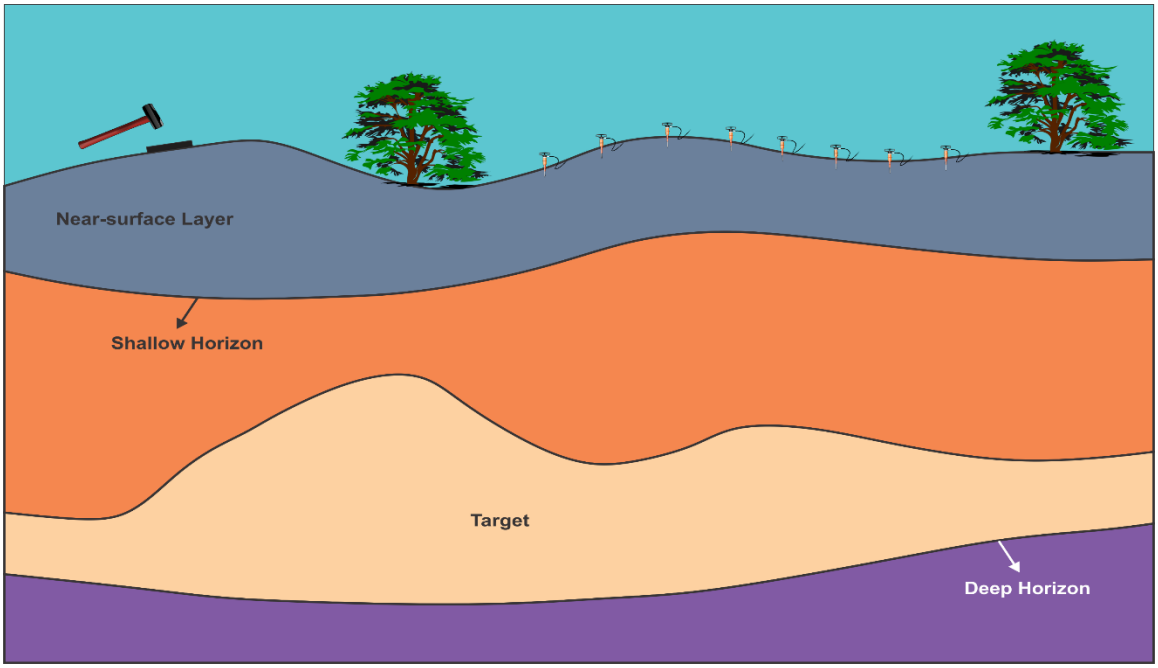

Figure 3.7. Key horizons for defining the survey parameters: surface, shallow, target, and deep horizons (modified after Stone, 1994).

3.2.1.1.1 Near-surface layer

Ground roll determination and offset calculation are made using near-surface layer velocities. Weathered layers are mostly affected by erosion and exposure, and show very low velocity. A small portion of the seismic data can be tested by comparing ground roll modeling. Also, static time shifts are able to be controlled with a reflection survey in areas where the weathered layer is thick and variable (Stone, 1994).

3.2.1.1.2 Shallow layer

Velocity information of the layers shallower than the target layer is usually required for processing and interpretation purposes. Imaging the shallower horizons is possible if the near offset, distance to the nearest receiver from the source, is less than

the depth of the shallow horizon. Depth of the horizon can be calculated by the following basic time-distance equation:

$$\boldsymbol{Z_{sh} = 0.5 \times t \times V_{sh}} \quad , \qquad \text{Eq. 3.1}$$

where:

t = two-way travel time to the shallow horizon,

V_{sh} = average-velocity to the layer, and

Z_{sh} = depth to the shallow layer.

Nearest usable offset (H_{near}) can be determined by noise tests in the field. The goal of these noise tests is keeping the near offset as small as noise conditions allow for imaging the shallower depths. Near offset parameter is determined by the following inequality:

$$\boldsymbol{H_{near} < Z_{sh}} \quad . \qquad \text{Eq. 3.2}$$

3.2.1.1.3 Target layer

The requirements of a survey design are determined according to the main layer of interest. If the information about a shallower layer is redundant, the same near offset calculations can be used for the target layer. Additionally, expected thickness and reflectivity information of the layer should be used to estimate the frequency range required to image the target. In theory, a quarter the wavelength of the source signal should be equal to the thickness of the target layer in order to image the top and bottom

of the layer (Liner, 2004). For real cases, however, possible maximum frequency is used to obtain the best image.

3.2.1.1.4 Deep Horizon

The deepest horizon desired to be imaged should be considered while deciding the survey parameters. In most cases, a seismic survey is not only designed to image the target layer, but is also designed to image deeper layers that will be used in interpretation, just as shallow layers are. Record length, source power, instrumental filters, and the maximum offset are considered by taking the depth of the deep horizon into account.

The rule of thumb is that the maximum offset (H_{max}) should be at least equal to the deepest target (Z_{deep}). The spread size can be a little greater for dipping layers. The rule for the maximum offset is given by Eq. 3.3:

$$\boldsymbol{H_{max} \geq Z_{deep}} \quad . \qquad \text{Eq. 3.3}$$

3.2.1.2. Group Interval (Spatial Sampling)

The group interval can be described as the horizontal distance between the centers of adjacent geophone groups, and can be seen in Figure 3.8 (Sheriff, 2002). Aliasing is the most important factor that determines the maximum group interval. Spatial aliasing can be seen in seismic data when the group spacing is coarse. In contrast to adequately selected group intervals, individual points do not merge into a continuous event. Hence, spatial aliasing decreases the quality of the seismic image (Liner, 2004).

Group intervals can be smaller depending on the survey budget, but they should not exceed the spatial aliasing limit. Maximum group interval condition is given by the following equation:

$$\mathbf{G_m} < \frac{\mathbf{V_{int}}}{\mathbf{2 \times f_{max} \times \sin \theta}} \quad , \qquad \text{Eq. 3.4}$$

where:

G_m = maximum group interval,

V_{int} = interval velocity,

f_{max} = maximum frequency expected, and

θ = maximum dip of the target horizon in degrees.

The Fresnel zone is another factor that can limit the maximum group interval. A Fresnel zone is the portion of a reflector making an actual image of the individual events (Sheriff, 2002; Stone, 1994). Maximum group interval determined the Fresnel zone is given by the following equation:.

$$\boldsymbol{G_f} < \frac{\boldsymbol{V_{rms} \times (t_z)^{\frac{1}{2}}}}{\boldsymbol{4 \times (f_{max})^{\frac{1}{2}} \times sin\, \theta}} \quad , \qquad \text{Eq. 3.5}$$

where:

G_f = maximum group interval determined by the Fresnel zone,

t_z = two-way record time of the target horizon,

V_{rms}= RMS velocity,

f_{max}= maximum frequency expected, and

θ = maximum dip of the target horizon in degrees.

The purpose of both aliasing and Fresnel zone formulas is to make the group intervals as large as possible to decrease survey cost while meeting resolution expectations.

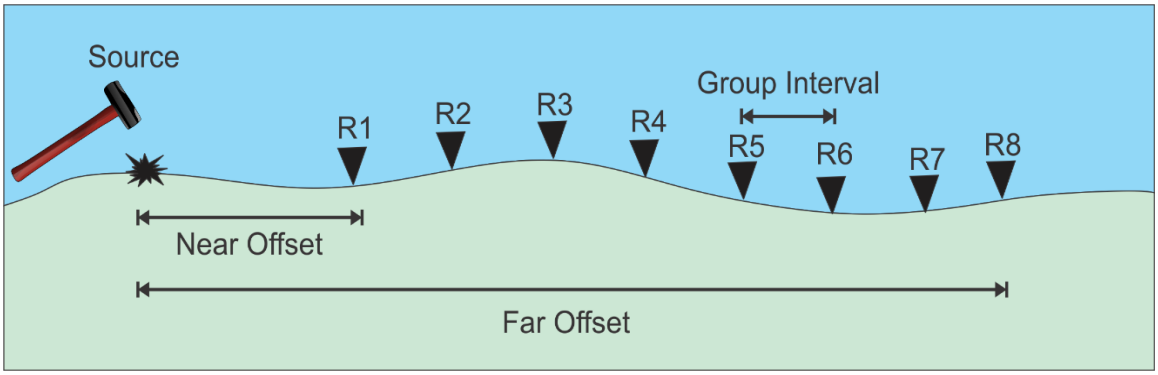

Figure 3.8 Representation of near offset, far offset, and group intervals. Triangles represent the geophone groups.

3.2.1.3 Time Sample Rate

The wave field initiated by the shot and recorded by the receiver should be adequately digitally sampled in the time and space domains. The maximum sampling frequency is determined by the Nyquist frequency. Frequencies above the Nyquist frequency threshold are aliased and reconstructed wave field are recorded with low frequencies which do not represent the original data. This effect is called temporal aliasing or simply aliasing (Liner, 2004). Nyquist frequency (f_{nyq}) is defined by the following:

$$f_{nyq} = \frac{1}{2\,dt} \quad , \qquad \text{Eq. 3.6}$$

where dt is the sample rate.

One half of the Nyquist frequency is the limit for the highest actual frequency, f_{max}, for reconstruction of a uniform wave field of the original signal. This rule provides the condition expressed in Eq. 3.7 for dt:

$$\boldsymbol{dt \leq \frac{1}{2}\left[\frac{1}{2f_{max}}\right] = \frac{1}{4f_{max}}} \quad . \qquad \text{Eq. 3.7}$$

In most of seismic surveys, the time sample rate is selected as 1 ms, since the sampling rate does not affect to acquisition cost. On the other hand, processing cost and data size are inversely proportional to sampling rate.

3.2.1.4 Recording Time

Recording time (listen time) of the survey should be calculated appropriately to reach survey objectives and/or adjust the survey cost. A rule for maximum recording time, t_{max}, is defined by the following (Liner, 2004):

$$\boldsymbol{t_{max} \geq \frac{1.4}{V_{avg}}\sqrt{x_{max}^2 + 4z_{max}^2}} \quad , \qquad \text{Eq. 3.8}$$

where:

V_{avg} = average velocity from the acquisition surface to the deepest reflector,

x_{max} = maximum offset, and

z_{max} = depth of the deepest horizon.

Employing this equation ensures that the listen time is long enough to record both reflections and diffractions coming from the deepest horizon. As represented in the equation, maximum recording time is calculated to be 40% longer than exact recording time to provide plentiful time for diffractions and possible dipping reflections (Liner, 2004). If steep dips or turning waves are expected, the recording time should be chosen to be longer than the calculated maximum recording time. Even though extra time will increase the survey cost, it is better to make sure that all possible seismic data are collected.

3.2.1.5 Signal-to-noise Improvement, Vertical Stack, and Fold Coverage

Any kind of event or vibration except primary reflections and diffractions are considered as noise in seismic data. The classification of noise types encountered in seismic data is shown in Figure 3.9.

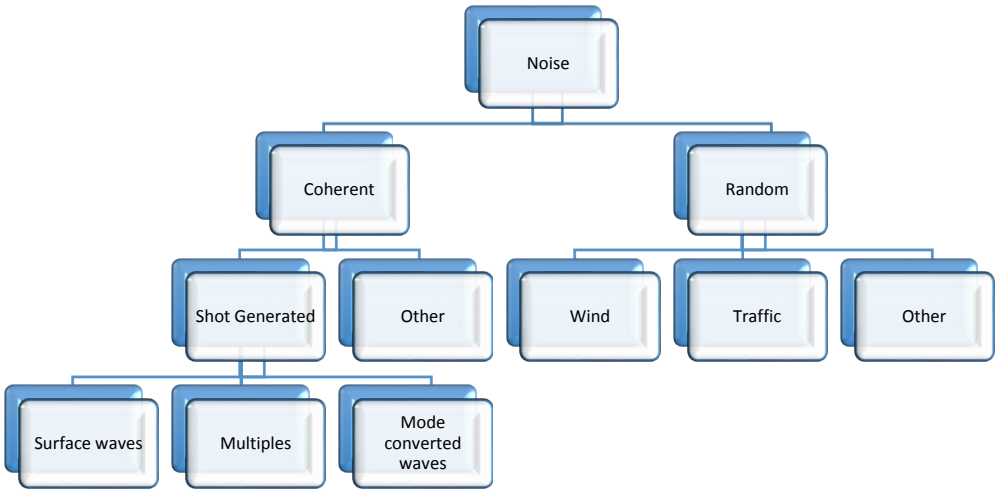

Figure 3.9. Classification of the noise types encountered in seismic data (modified after Liner, 2004).

Signal-to-noise ratio is the term that is used to explain the signal strength relative to noise strength. Unless the noise is used for specific analysis, a higher signal-to-noise ratio is always desired in seismic data. However, in practice, it is difficult to determine and isolate signal from noise (Liner, 2004; Sheriff, 2002).

Vertical stacking and common-midpoint (CMP) stacking are the two main methods that can be applied in acquisition to increase the signal-to-noise ratio. Vertical stacking is a signal-to-noise enhancement method that combines the subsequent shot profiles generated at the same shot location. The number of vertical stacks directly affects the acquisition time. Therefore, number of vertical stacks is one of the fundamental factors that determines survey duration. Industry standards state that the fold of vertical stack should be between one and eight (Stone, 1994).

Furthermore, common midpoint stacking can be considered as both a recording and a processing method. Traces assumed to be coming from a certain position on the earth's surface are stacked to generate a single trace at that position to increase the signal-to-noise ratio. The number of those traces, which are added to give a single trace in a certain position, is called stacking fold or fold-of-coverage (Cordsen et al., 2000; Liner, 2004; Sheriff, 2002). The number of recording channels, groups, and shot intervals are the main factors that determine the CMP fold. The fold for a 2D line is defined by the following equation:

$$F_{2D} = \frac{N_c \times dx_g}{2 \times dx_s} \quad , \qquad \text{Eq. 3.9}$$

where:

F_{2D} = fold for a 2D line,

N_c = number of recording channels,

dx_g = group interval, and

dx_s = shot interval.

The effect of those stacking procedures can be defined with signal-to-noise improvement factor, I_{sn}, as follows:

$$I_{sn} = \sqrt{F_v \times F_{cmp} \times N_g} \quad , \qquad \text{Eq. 3.10}$$

where:

$F_{v:}$ = fold of vertical stack,

F_{cmp} = fold of CMP stack, and

N_g = number of geophones per group.

The final signal-to-noise ratio can be calculated employing the following equation:

$$R_{snf} = R_{snr} \times I_{sn} \quad , \qquad \text{Eq. 3.11}$$

where:

R_{snf} = final signal-to-noise ratio,

R_{snr} = raw signal-to-noise ratio, and

I_{sn} = signal-to-noise improvement factor.

3.2.2 Analyses of the Actual 2-D Survey

In this part of study, the 2-D seismic survey carried out within the salt boundary was analyzed in terms of fold, illumination, resolution, and offset distribution in 2-D velocity model. Parameters of the survey are given by Table 3.2.

Table 3.2. Acquisition parameters of actual 2-D seismic survey.

Number of Receiver Stations	193	**Number of Shots**	192
Number of Receivers	120	**Receiver Interval**	5 m
Shot Interval	5 m	**Shot line length**	945 m
Receiver line length	955 m	**Sampling rate**	1 ms
Recording length	4 s		

The maximum fold of the survey was 120; however, fold values were not uniformly distributed along the survey line, since the receiver line was rolled once from the 73rd station, unlike in the conventional 2-D seismic acquisition (Figure 3.10). A trace count-offset histogram of the survey is shown in Figure 3.11.

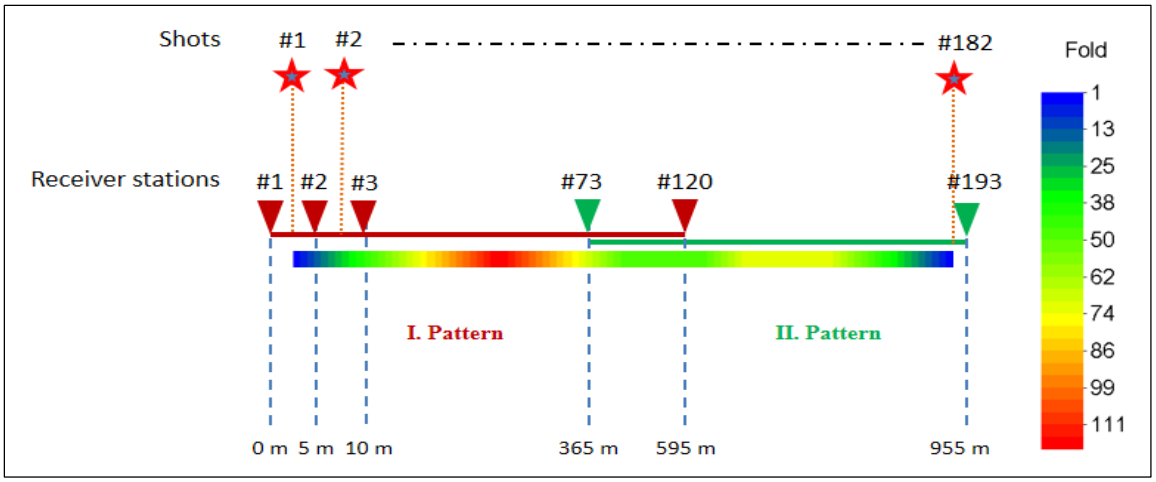

Figure 3.10. Survey geometry and fold distribution of the actual 2-D survey.

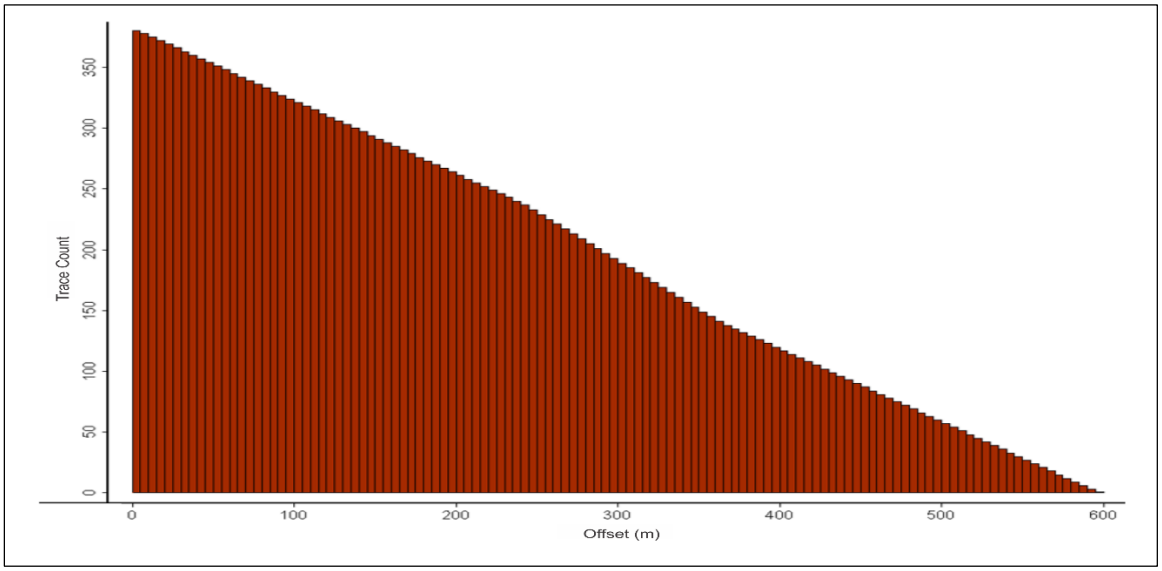

Figure 3.11. Trace count-Offset histogram of actual 2-D seismic survey. The chart shows the number of traces that fall within each range of offset values.

Source frequency and group interval parameters were used in the survey to determine vertical and horizontal resolutions. Possible vertical and horizontal resolutions of the seismic image before and after migration are depicted in Figures 3.12 and 3.13, respectively. Note that a 120 Hz maximum frequency and 2.5 m CDP interval were used to determine these resolutions.

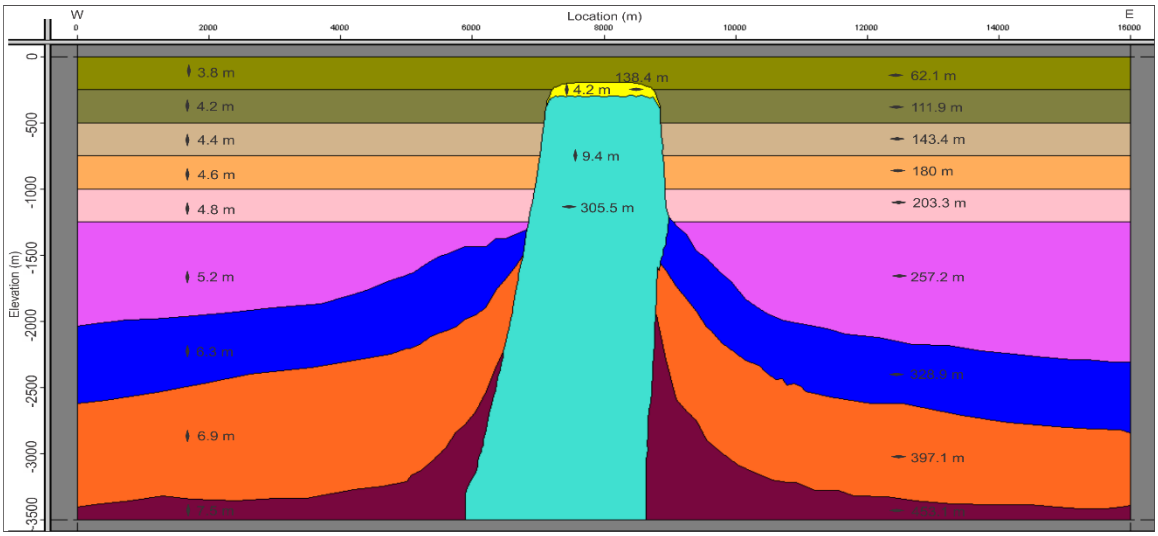

Figure 3.12. Vertical and lateral resolutions of actual 2-D seismic survey in certain depths before migration. Vertical and horizontal diamond shapes represent the vertical and lateral resolution, respectively.

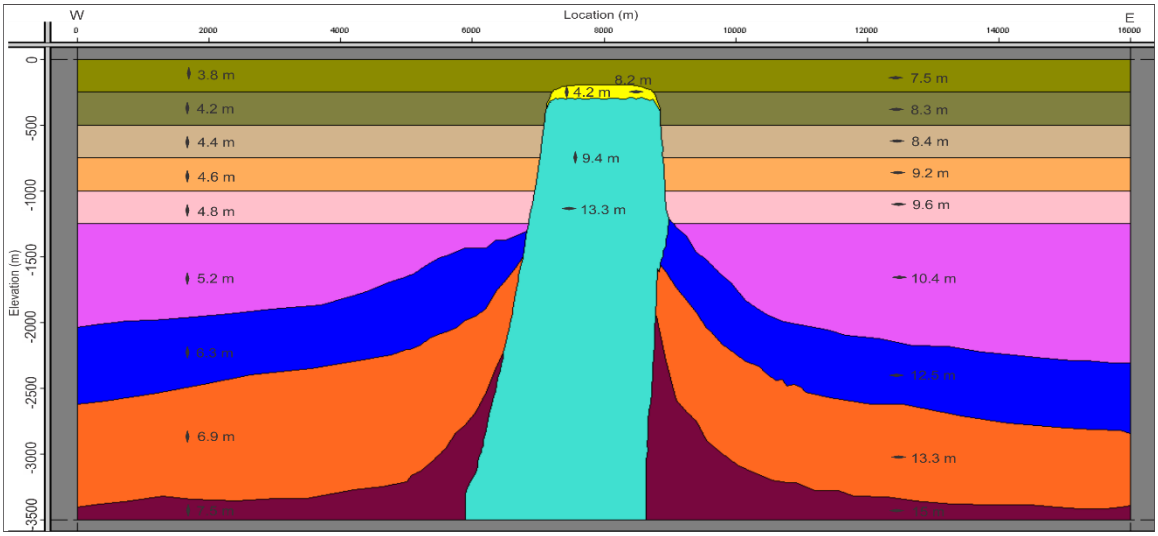

Figure 3.13. Vertical and lateral resolutions of actual 2-D seismic survey in certain depths after migration. Vertical and horizontal diamond shapes represent the vertical and lateral resolution, respectively.

Although the data had been collected close to the edge of the salt dome, the edge of the salt could not be imaged. Illumination analysis showed that this survey geometry can only provide images from the top of the salt and overlying cap rock layers, since the

reflections from the edges of the salt dome were not recorded by the receivers (see Figures 3.14 and 3.15). As a result, a new 2-D seismic survey with larger offsets and better fold distribution was carried out in this study in order to image the salt and surrounding sediments.

Figure 3.14. Illumination of the first shot in actual 2-D seismic survey.

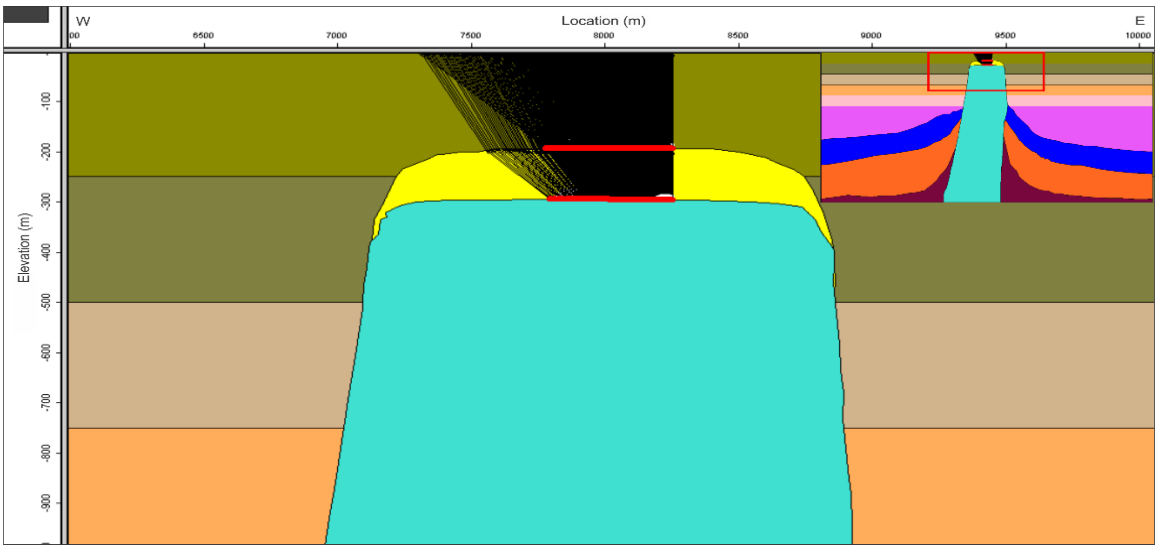

Figure 3.15. Illumination of the last shot in actual 2-D seismic survey.

3.2.3 Two-D Seismic Survey Design using RTM Cases

Acquisition parameters calculated using general survey design equations are usually adequate to image flat layers and slightly dipping surfaces. However, determining those parameters for complex structures, such as folds, faults, domes, and reefs is more difficult due to the complicated wave field behavior in these areas. Seismic data acquisition simulations over a model of the study area can provide crucial information for determining survey parameters. If the model is constructed close enough to the real structure, it is possible to obtain very realistic synthetic seismic data by seismic modeling. Therefore, seismic modeling is one of the most economical ways to establish and test the optimum acquisition parameters for getting the best image of these complex geological structures.

In this part of the study, a series of analyses were performed with seismic modeling to propose a conventional 2-D seismic survey with the same limited acquisition equipment to image the salt structure and surrounding sediments. Pre-stack modeling (shot gathers) was done with the finite difference method using a full (two-way) acoustic wave equation. The Reverse Time Migration (RTM) algorithm was used in the pre-stack imaging, since the velocity models consisted of complex and highly dipping structures. Unlike the other migration techniques, RTM uses the two-way acoustic wave equation without any approximations and assumptions (Baysal et al., 1983). Therefore, RTM makes imaging of the complex structures possible without any error or dip limitations. In this study, both pre-stack modeling and imaging were done using Paradigm's Echos software.

3.2.3.1 Maximum offset determination

The goal of the maximum offset determination process is to keep the maximum offset range as small as possible, while keeping the events from important reflectors, which are necessary in migration, within the recorded data. In order to determine the optimum offset range, different ranges were tested through pre-stack modeling and RTM imaging, starting with the initial survey parameters. These initial survey parameters were chosen without considering survey cost or time. First, a maximum group interval was calculated from basic equations (Eq. 3.4 and 3.5) for spatial aliasing and the Fresnel zone. Based on the calculations, the maximum group interval was expected to be less than 13.3 m for a 120 Hz maximum frequency, 70° maximum dip, and 3000 m/s average interval velocity of the model. So, the maximum group interval was chosen as 10 m. Shots were generated for every two receiver stations with a 20 m interval. Finally, 1600 receivers and 800 shots were used along a 16 km spread for the initial pre-stack modeling. Shot and receiver configuration of the initial model is shown in Figure 3.16. Initial record length of the survey was chosen as 8 s.

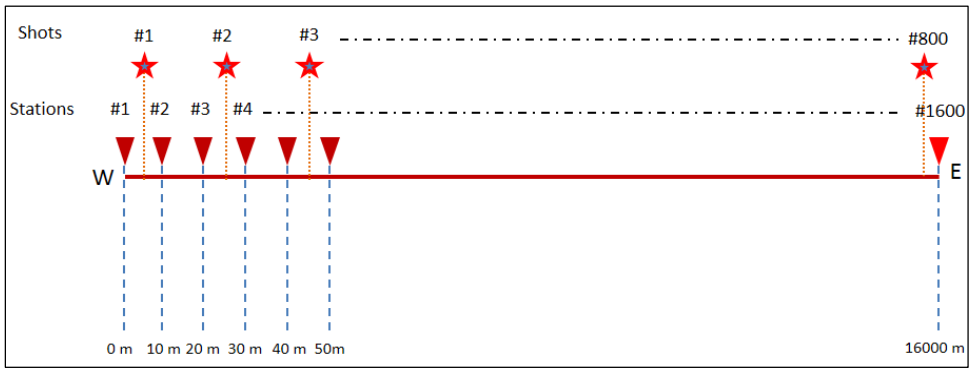

Figure 3.16. Initial shot and receiver configuration for pre-stack modeling.

The seismic source signal to create shot gathers was analyzed before generating the synthetic data. The autocorrelation of a linear vibroseis sweep resulted in a Klauder wavelet. Sweep length, sweep taper, and start and end frequencies of the sweep determine the shape of the source wavelet. In order to test the effect of sweep tapers on the source wavelet, three sweep signals were generated with same sweep length (12 s) and frequency (linear sweep from 10 Hz to 120 Hz) (see Figure 3.17). According to these sweep taper analyses, autocorrelation of sweep with a 0.1 s taper showed narrower wavelet closer to a spike with better amplitude range. However, ringing artifacts can be seen on the power spectrum of the signal (see Figure 3.18). Therefore, sweep taper can be chosen between 0.1 s and 1 s to have a desired source signal without the ringing artifacts.

Also, the Butterworth source wavelet was compared with the Klauder. The Butterworth wavelet did not show a ringing artifact in the power spectrum and had fewer side lobes than the Klauder wavelet, as can be seen in Figure 3.19. Before deciding the source wavelet used in pre-stack modeling, example shot gathers were created with both the Klauder and Butterworth wavelets (Figure 3.20). Based on the examined shot gathers, the Butterworth source wavelets revealed better images compared to the Klauder wavelets, since the side lobes of the Klauder wavelets caused ringing effect on shot gathers, which is not desirable in data processing. Also, effects of the Klauder source wavelets can be seen in every part of the image since it is a long wavelet. Therefore, the Butterworth wavelet was preferred as the source wavelet in our pre-stack modeling.

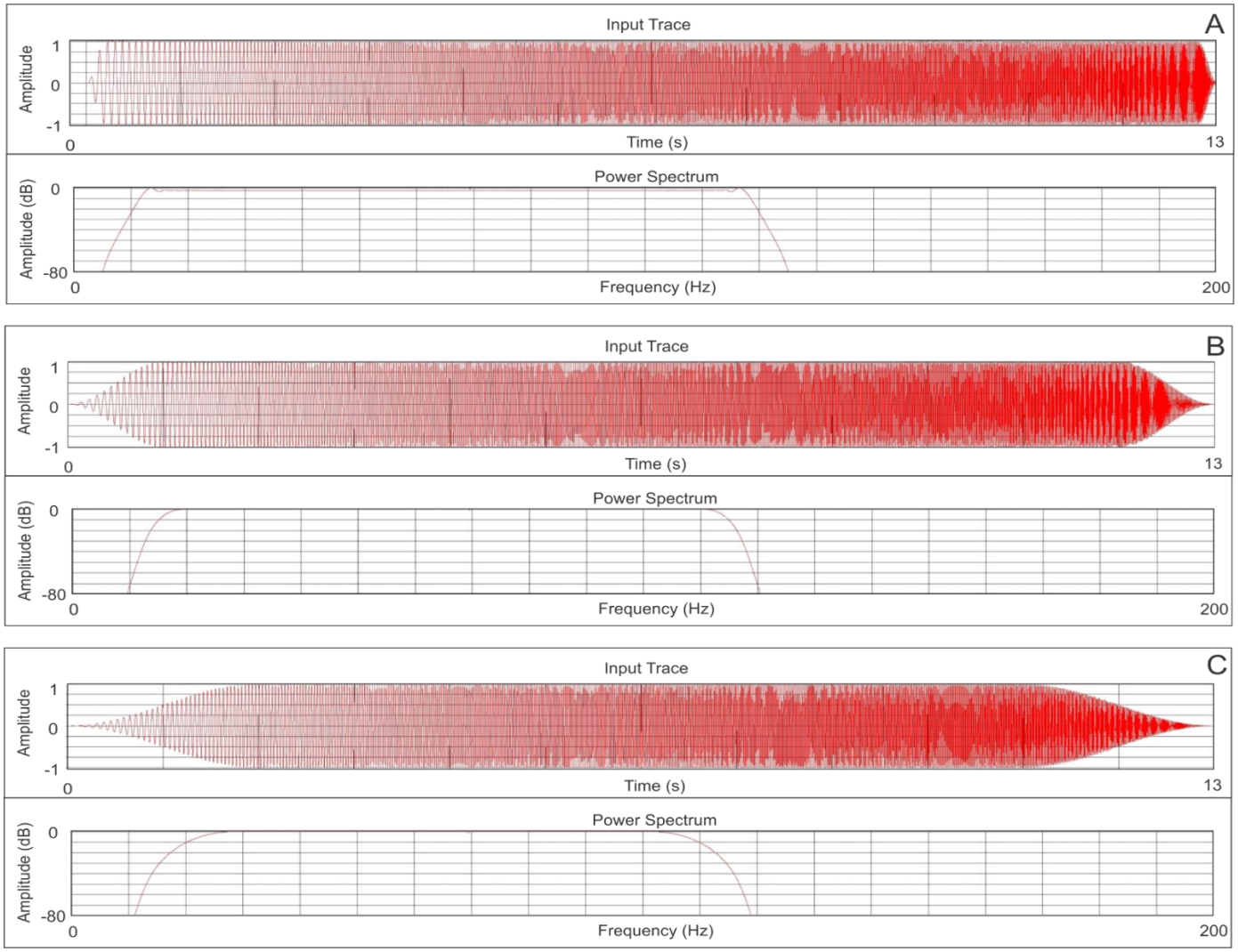

Figure 3.17. Vibroseis sweeps with different taper lengths: A) Taper length: 0.1 s, B) Taper length: 1 s, and C) Taper length: 2 s.

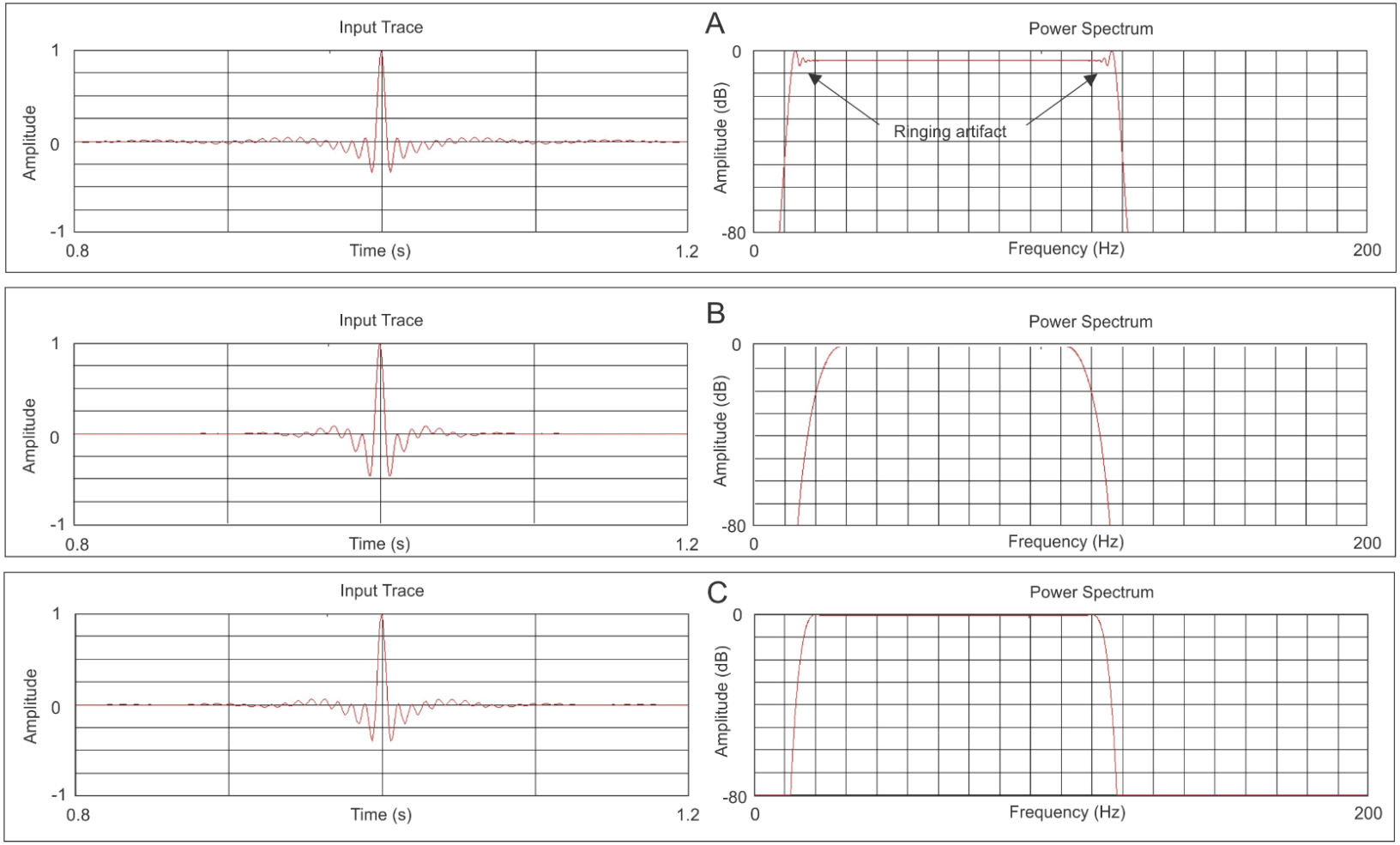

Figure 3.18. Klauder wavelets obtained by auto correlation of vibroseis sweeps with different taper lengths and their power spectrums: A) Taper length: 0.1 s, B) Taper length: 1 s, and C) Taper length: 2 s.

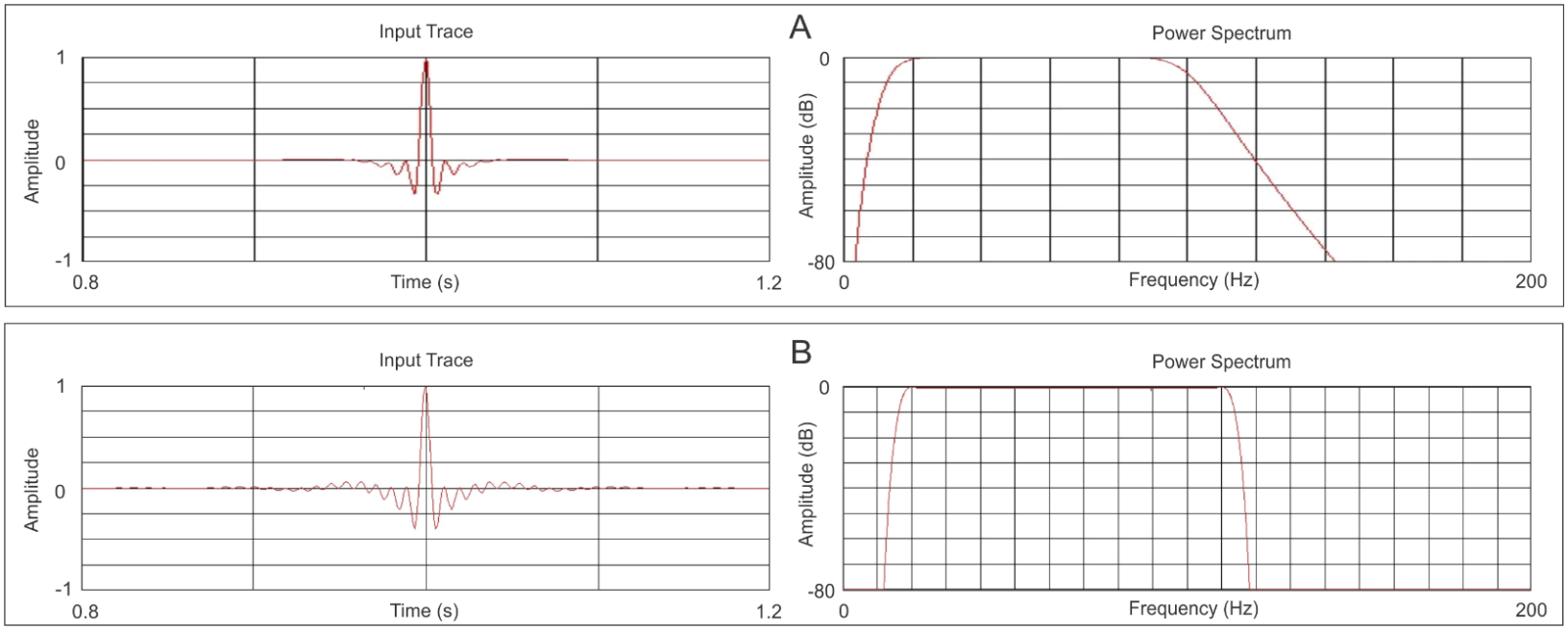

Figure 3.19. Comparison of the Butterworth and Klauder wavelets: A) Input trace and power spectrum of the Butterworth wavelet, and B) Input trace and power spectrum of the Klauder wavelet.

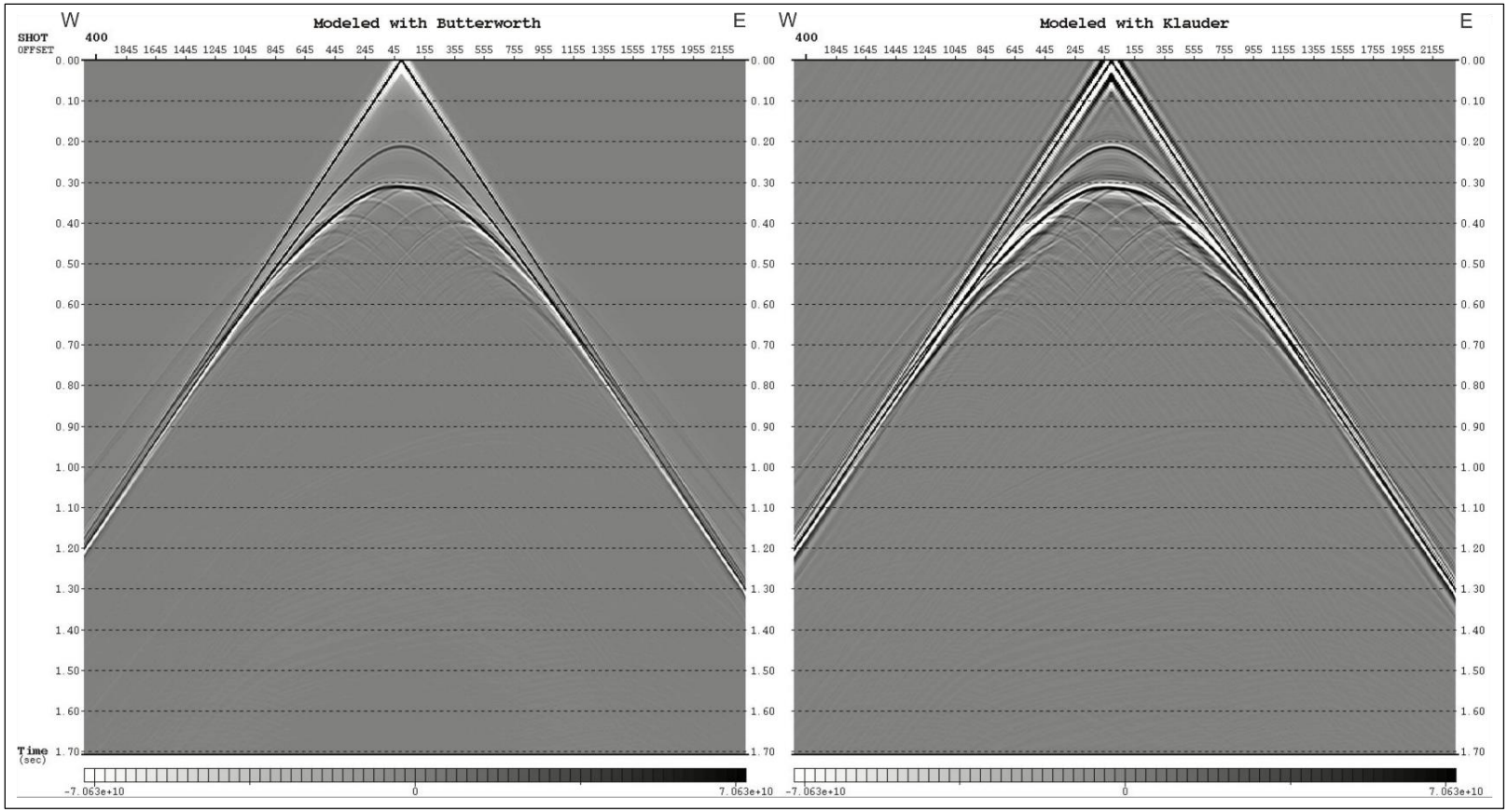

Figure 3.20. Comparison of the Butterworth and Klauder wavelets in modeled shot gathers. Color bar indicates the amplitude.

After the source signal decision, raw shot gathers were modeled using initial survey parameters. RTM was applied to raw shot gathers to obtain images from every shot. In addition to RTM images, illumination analysis with ray tracing was done to demonstrate the contribution of every shot. RTM images of the first, middle, and last shots and the illumination of these shots are shown in Figures 3.21-3.23. As seen in these figures, all shots provide important information from different events to the final RTM image. Especially, shots far from the salt structure allowed us to record the reflections and diffractions generated from dipping layers and the edge of the salt dome. The shots located closer to the salt dome contributed to the final image by illuminating the near surface reflections coming from the top of the salt, cap rock, and shallow layers.

In the final RTM image obtained from raw shots, the effects of the first breaks appeared as low frequency noise, especially on shallow parts of the data (Figure 3.24). This low frequency noise made the shallow events unclear for interpretation. Thus, first breaks were eliminated from each shot to increase the quality of the data (Figure 3.25). Comparison of RTM images before and after first break elimination is shown in Figure 3.26. It is obvious that elimination of the first breaks made the top of the salt, cap rock, and shallow horizontal layers more interpretable.

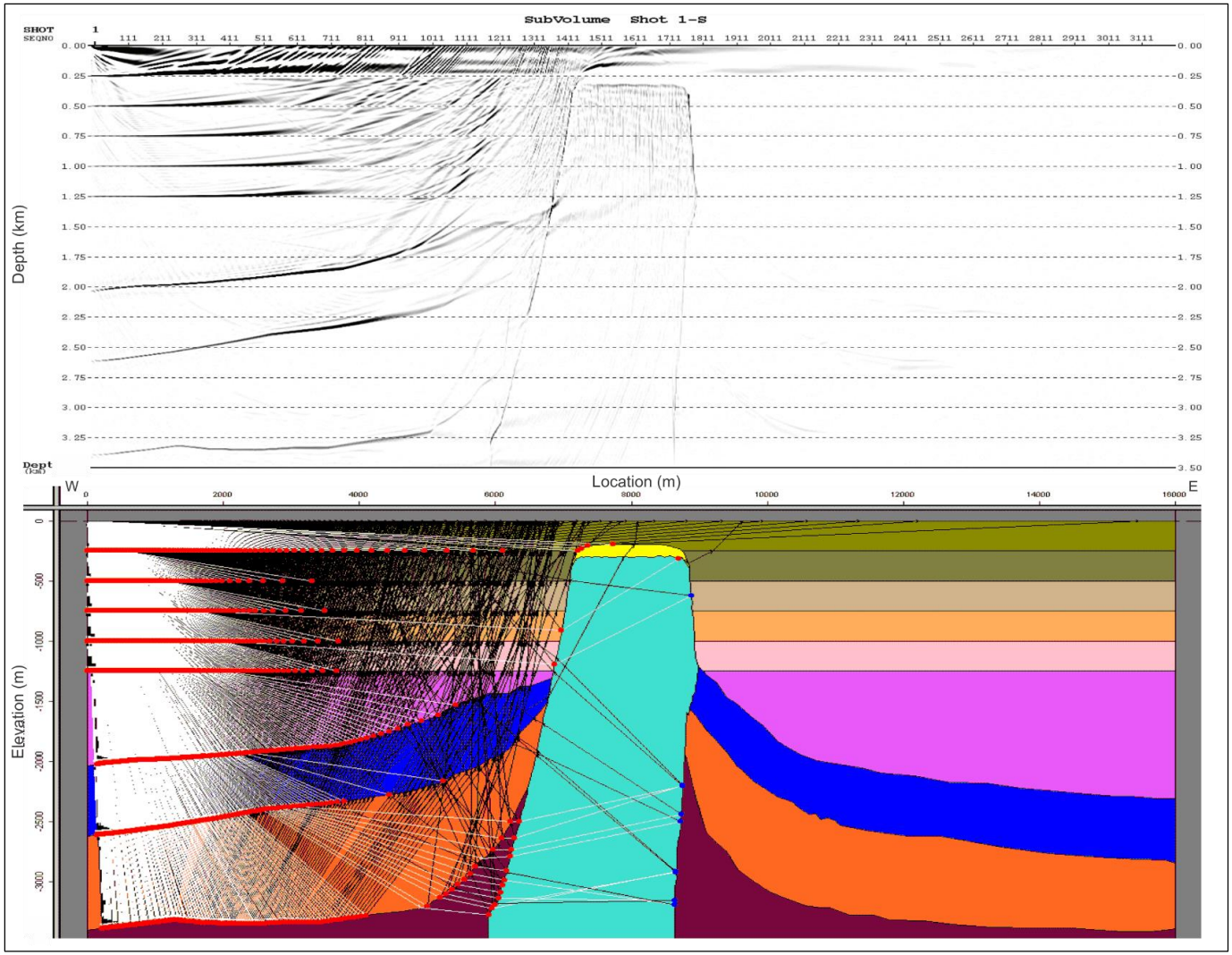

Figure 3.21. Sub-volume of first shot after RTM (above) and illumination of first shot for initial survey parameters (below).

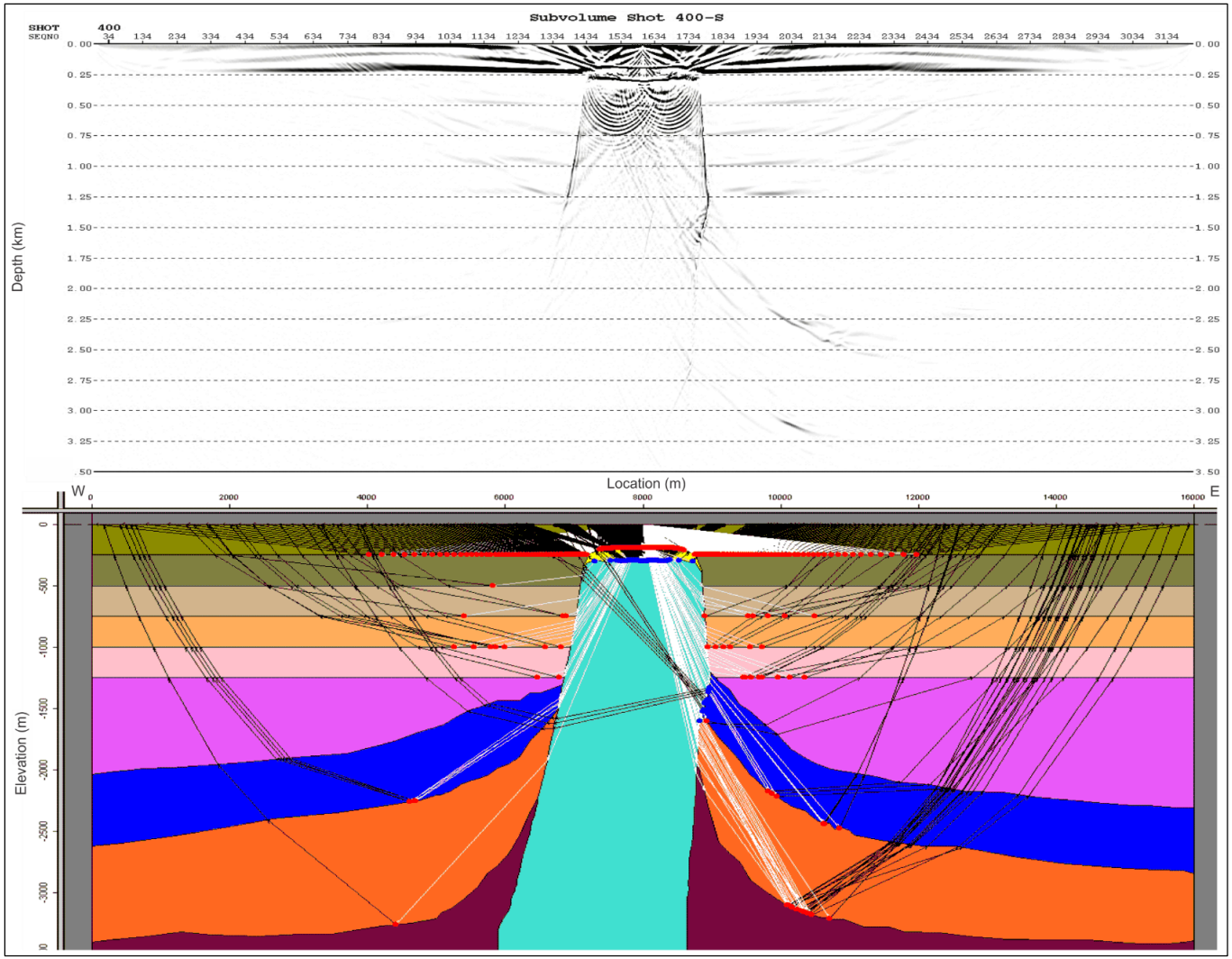

Figure 3.22. Sub-volume of the middle shot after RTM (above) and illumination of middle shot for initial survey parameters (below).

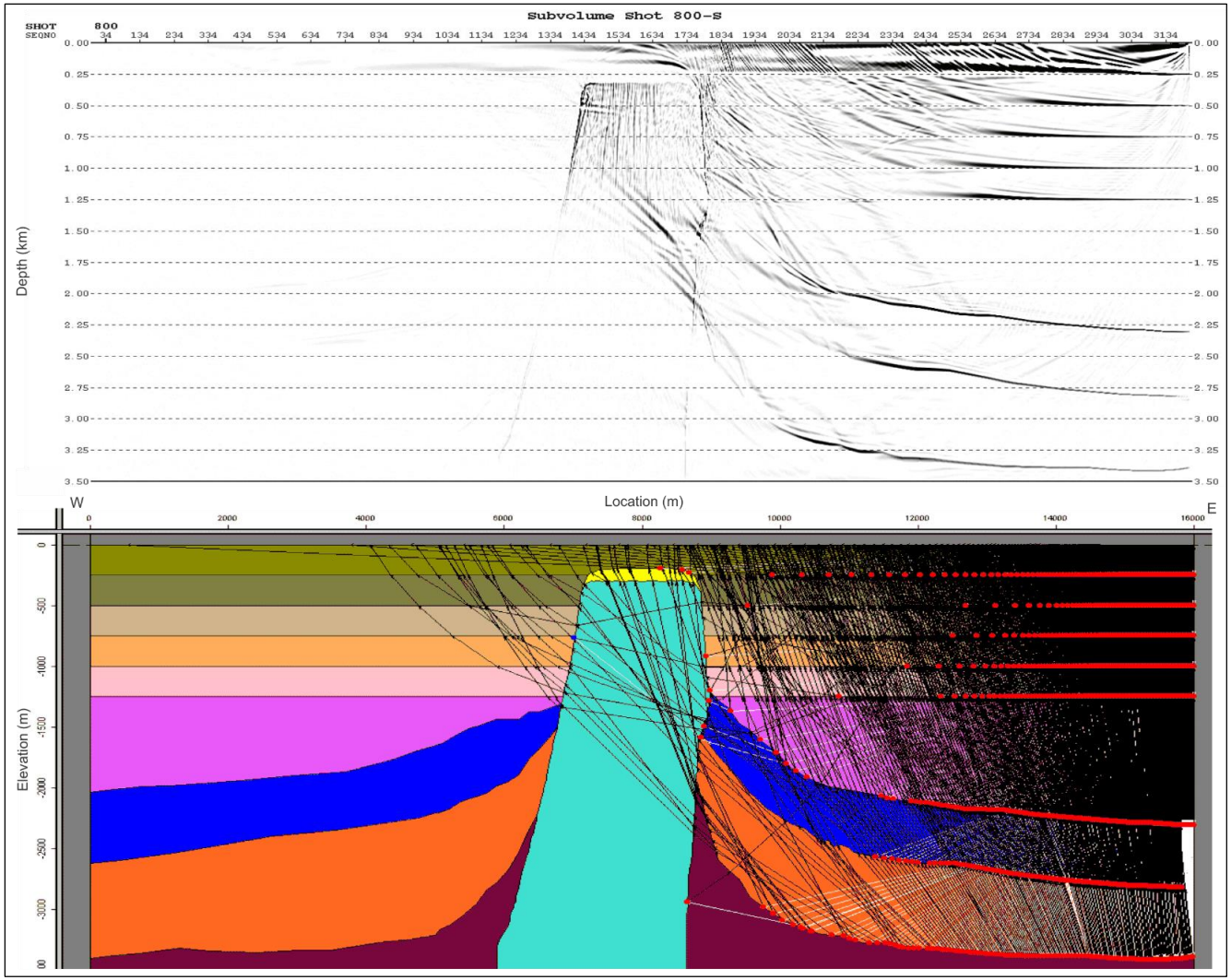

Figure 3.23. Sub-volume of the last shot after RTM (above) and illumination of last shot for initial survey parameters (below).

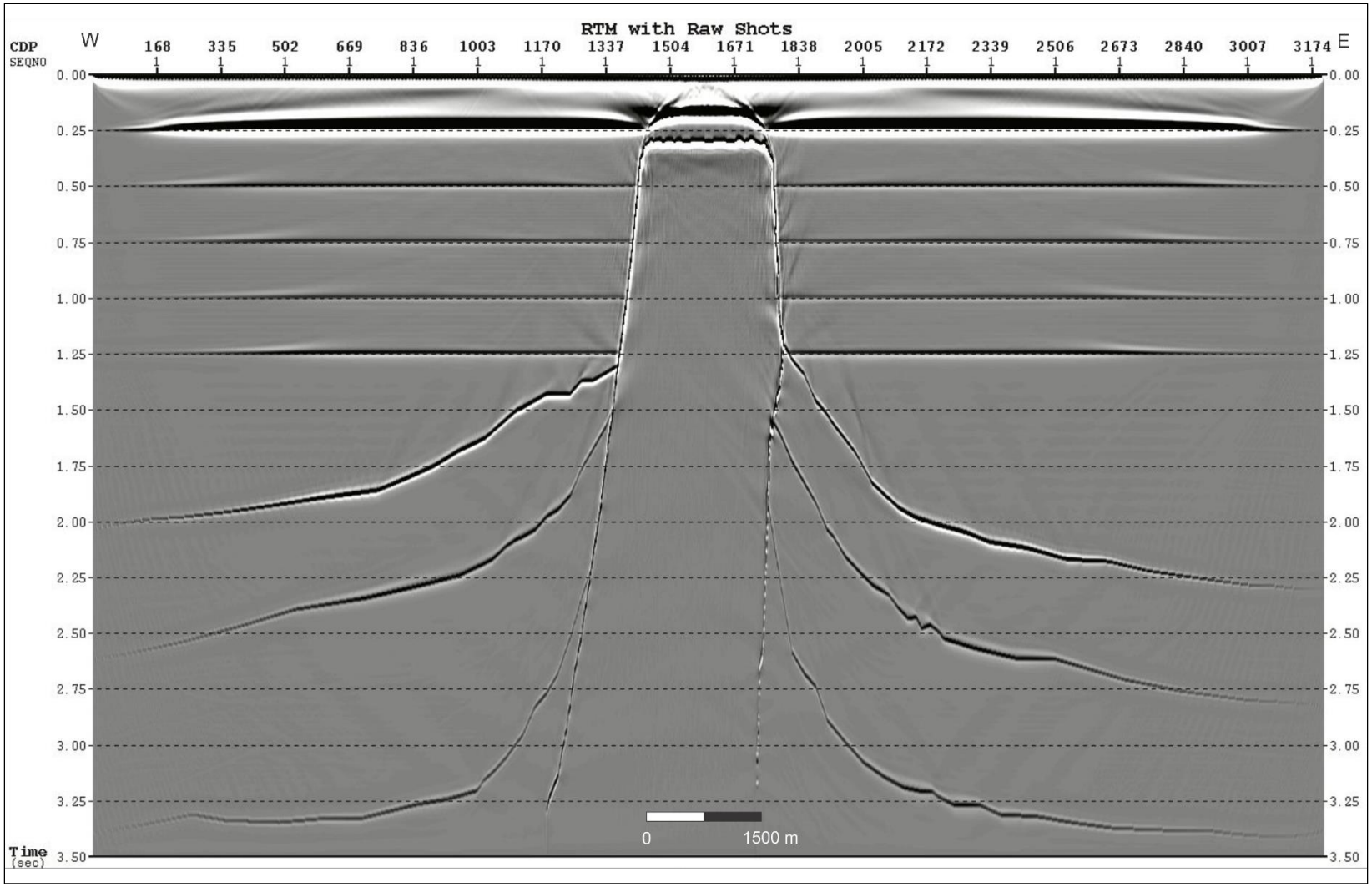

Figure 3.24. Final RTM image obtained from raw shot gathers.

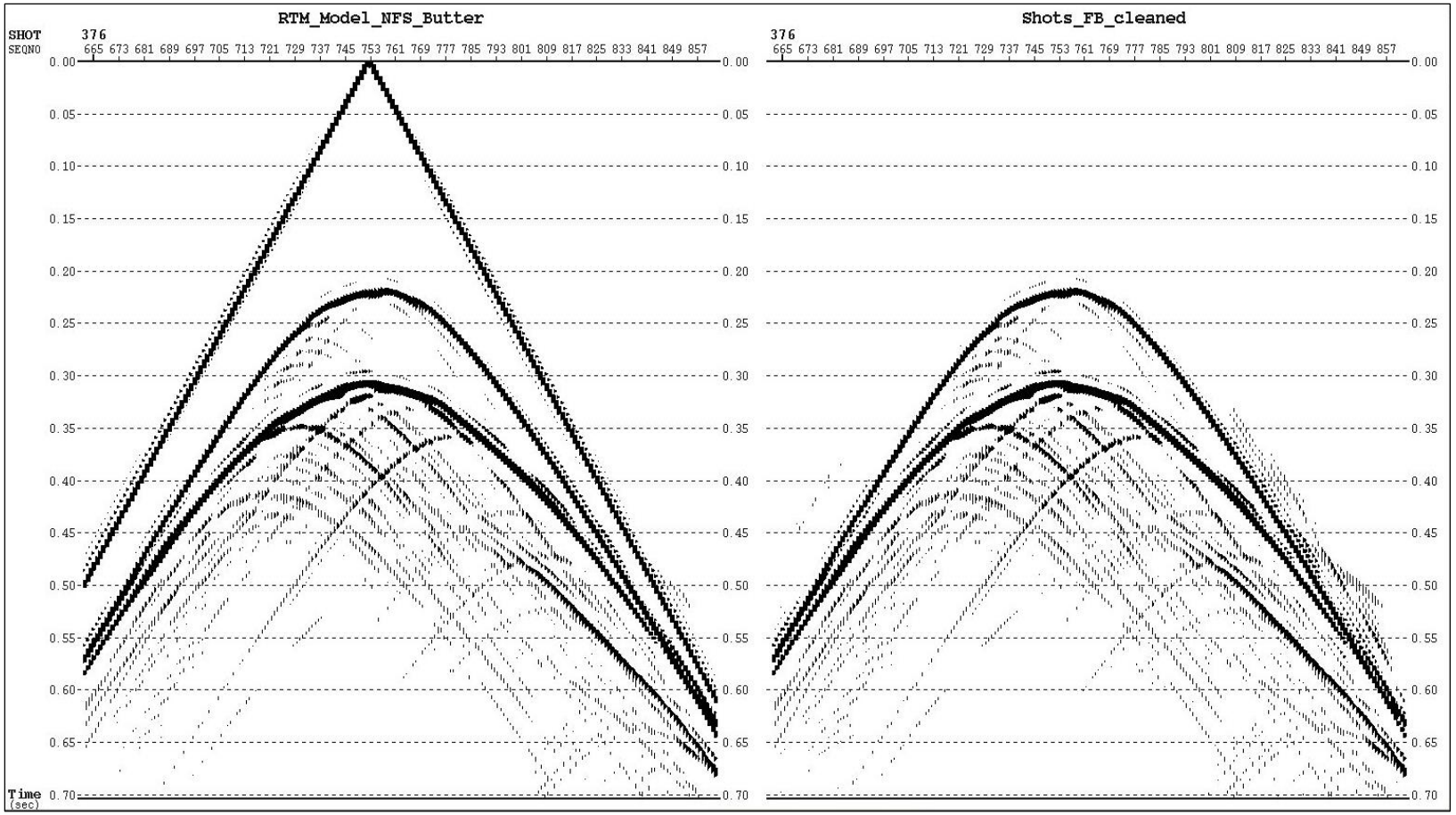

Figure 3.25. Raw and first break elimination applied to shot gathers (Shot number 376).

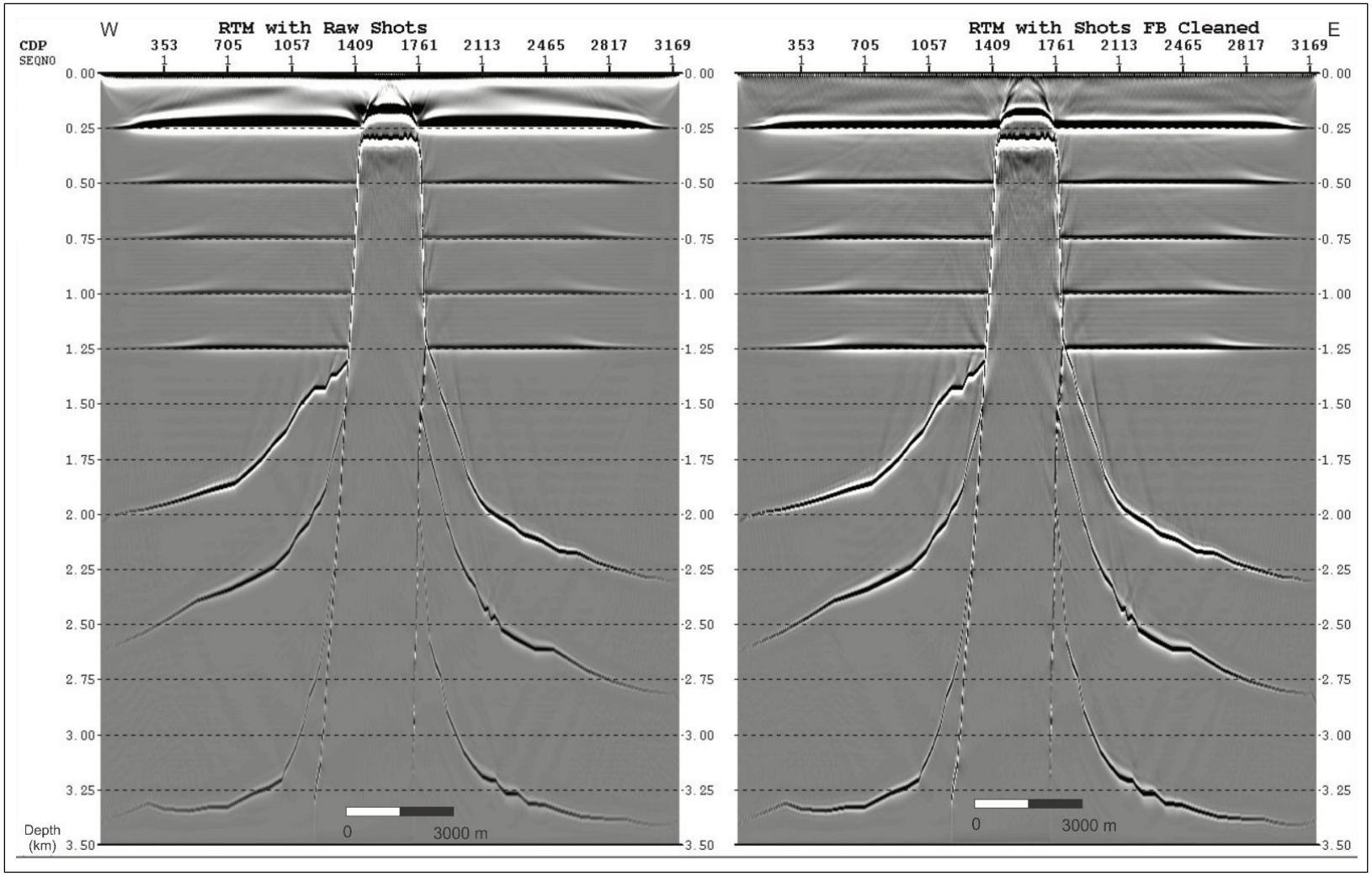

Figure 3.26. Comparison of final RTM images obtained from raw (left) and first break eliminated (right) shot gathers.

The offset range contribution was important to update the initial survey parameters and limit the maximum offset of the survey. To understand the contribution of different offsets, the images from the 0 - 6000 m, 6000 - 11,000 m, and 11,000 – 16,000 m offsets were analyzed (see Figures 3.27-3.29). Though all offset ranges assisted in achieving a better quality image, the best contribution to the RTM images was from 0 – 6000 m offset range (Figure 3.30). Also, images from the 6000 – 11,000 m and 11,000 – 16, 000 m offset ranges showed that these generated low frequency noise at shallow depths where horizontal or slightly dipping layers exist. Therefore, updating the initial survey parameters for the 6000 m offset range was possible. However, the offset range was still too large for the intended acquisition equipment.

In order to limit the maximum offset of the survey, the same offset contribution analyses were done for the 0 – 6000 m, 0 - 3000 m, and 0 – 1500 m offset ranges. None of the three RTM images from these different offset ranges showed much difference in terms of image quality (Figures 3.31 and 3.32). This comparison allowed us to limit the maximum offset range to 1500 m, which was a reasonable parameter for the limited acquisition equipment. Note that the 0 – 1500 m offset range equals to a 3000 m receiver line, since the shot is fired in the middle of the receiver line in conventional split-spread seismic surveys. Finally, the initial maximum offset was reduced from 16,000 m to 1500 m by analyzing the contribution of offset ranges in RTM images. Moreover, the number of receivers was reduced from 1600 to 300 by updating the offset range. Figure 3.33

illustrates the conventional seismic survey layout with the updated maximum offset parameter.

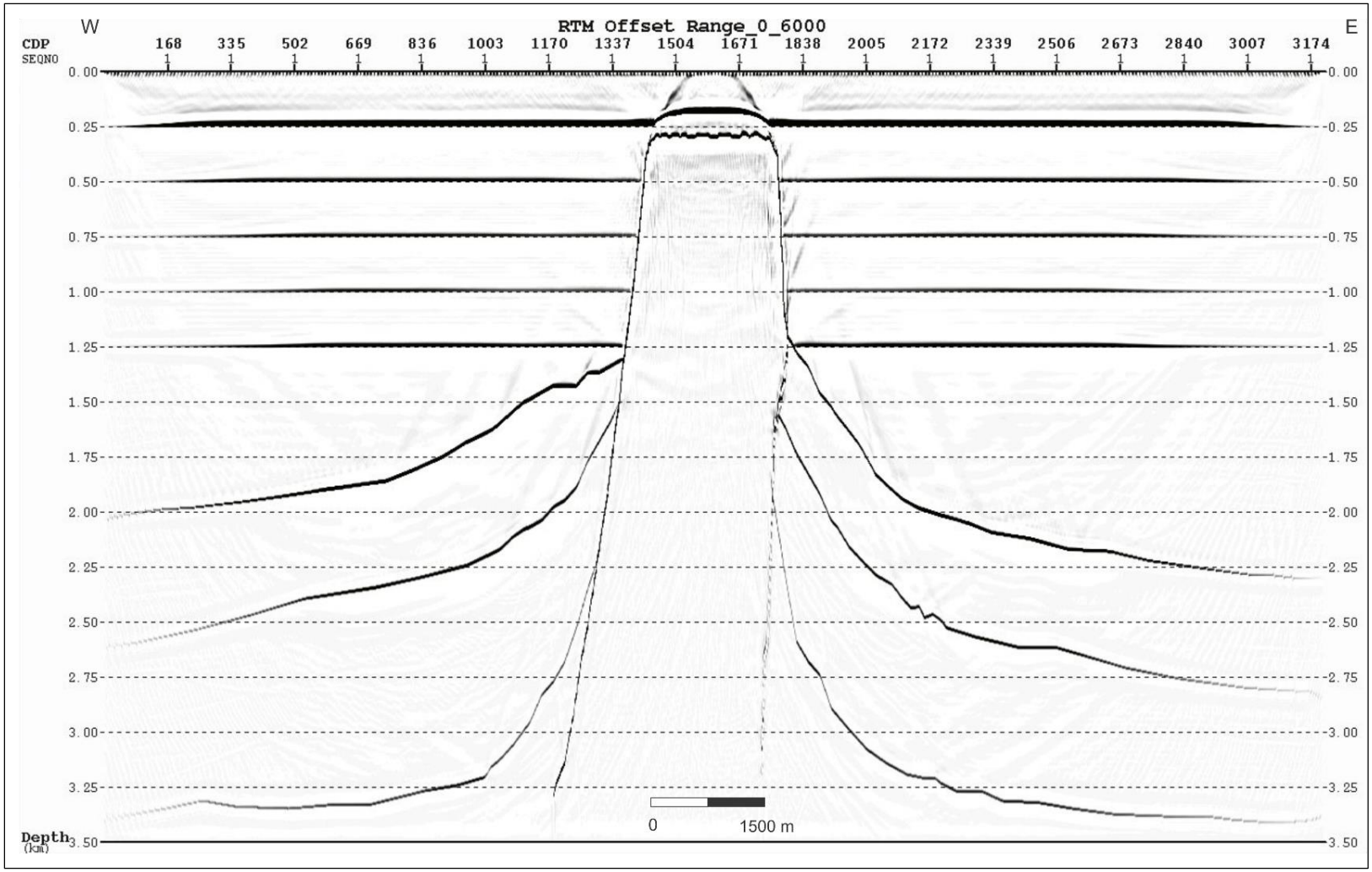

Figure 3.27. RTM image obtained using the 0–6000 m offset range.

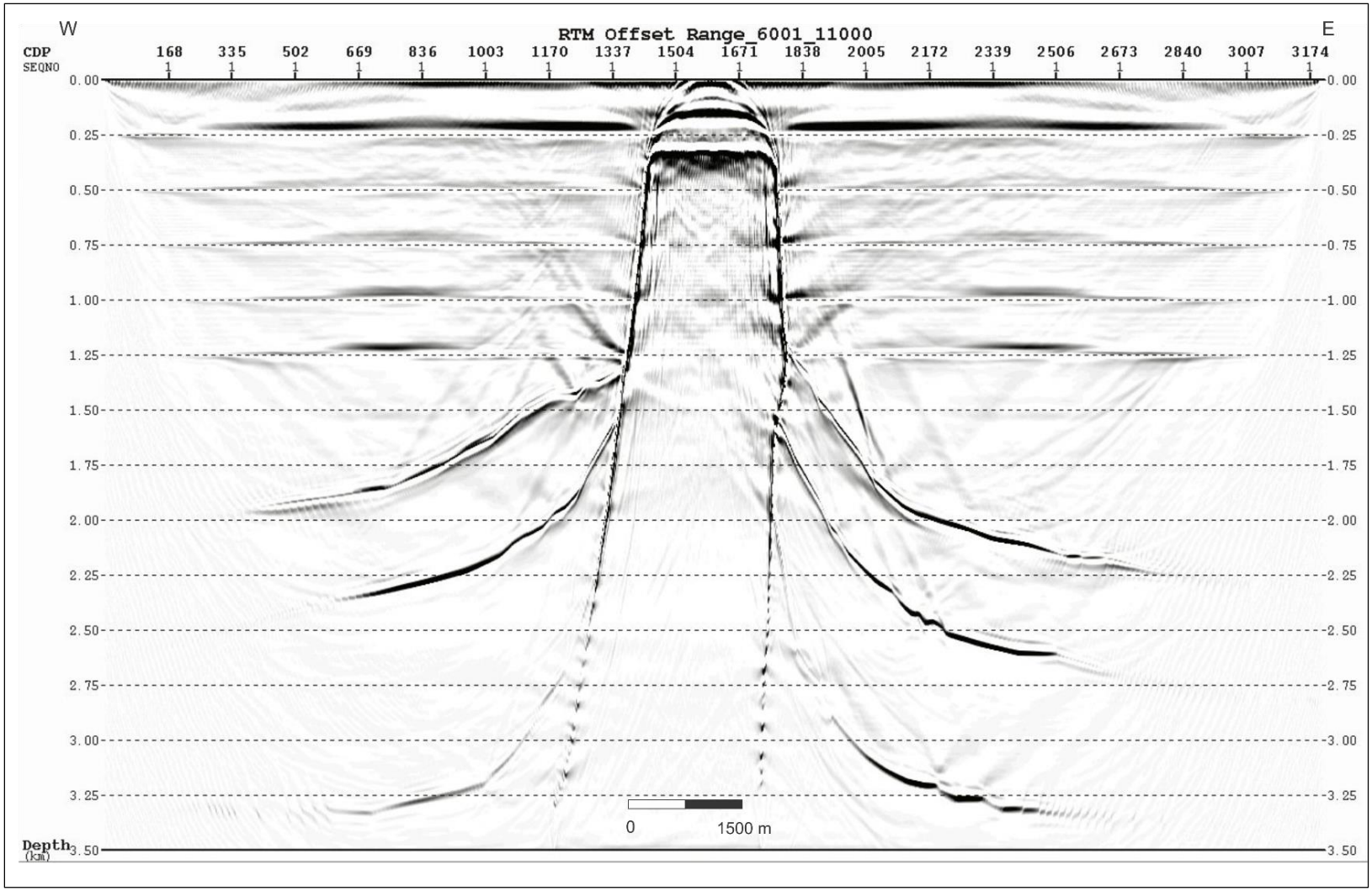

Figure 3.28. RTM image obtained using the 6000–11000 m offset range.

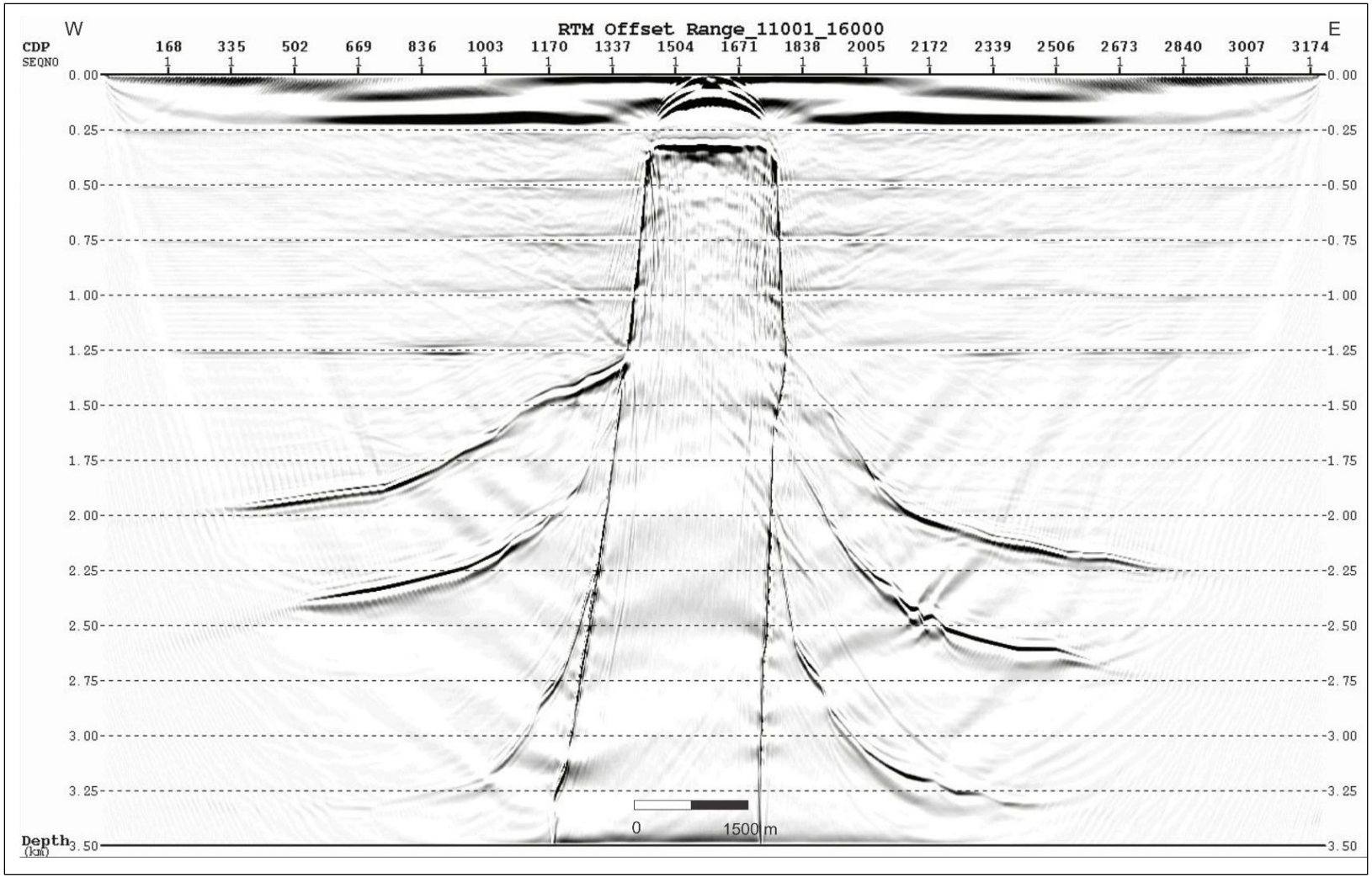

Figure 3.29. RTM image obtained using the 11000–16000 m offset range.

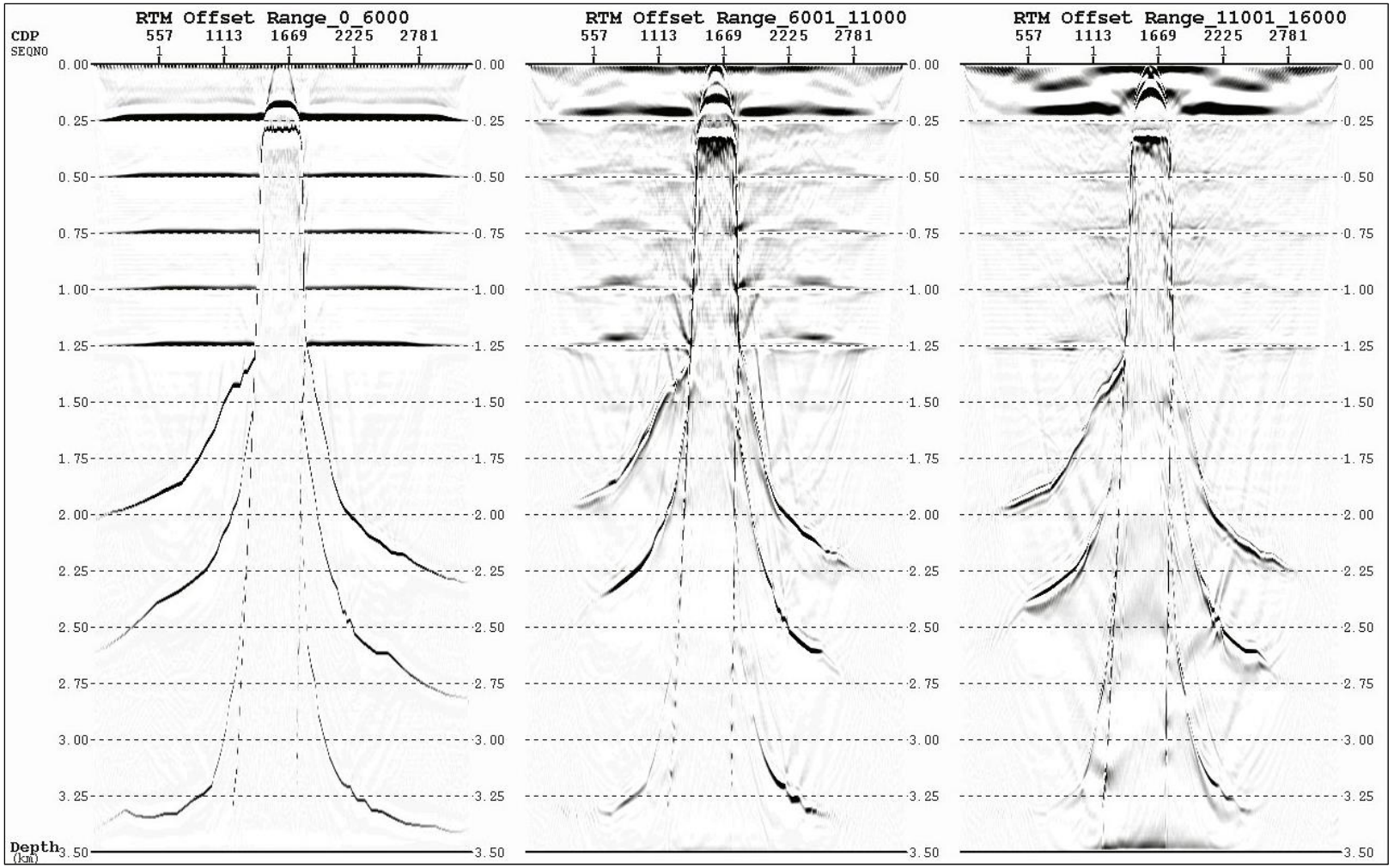

Figure 3.30. Comparison of RTM images obtained using different offset ranges.

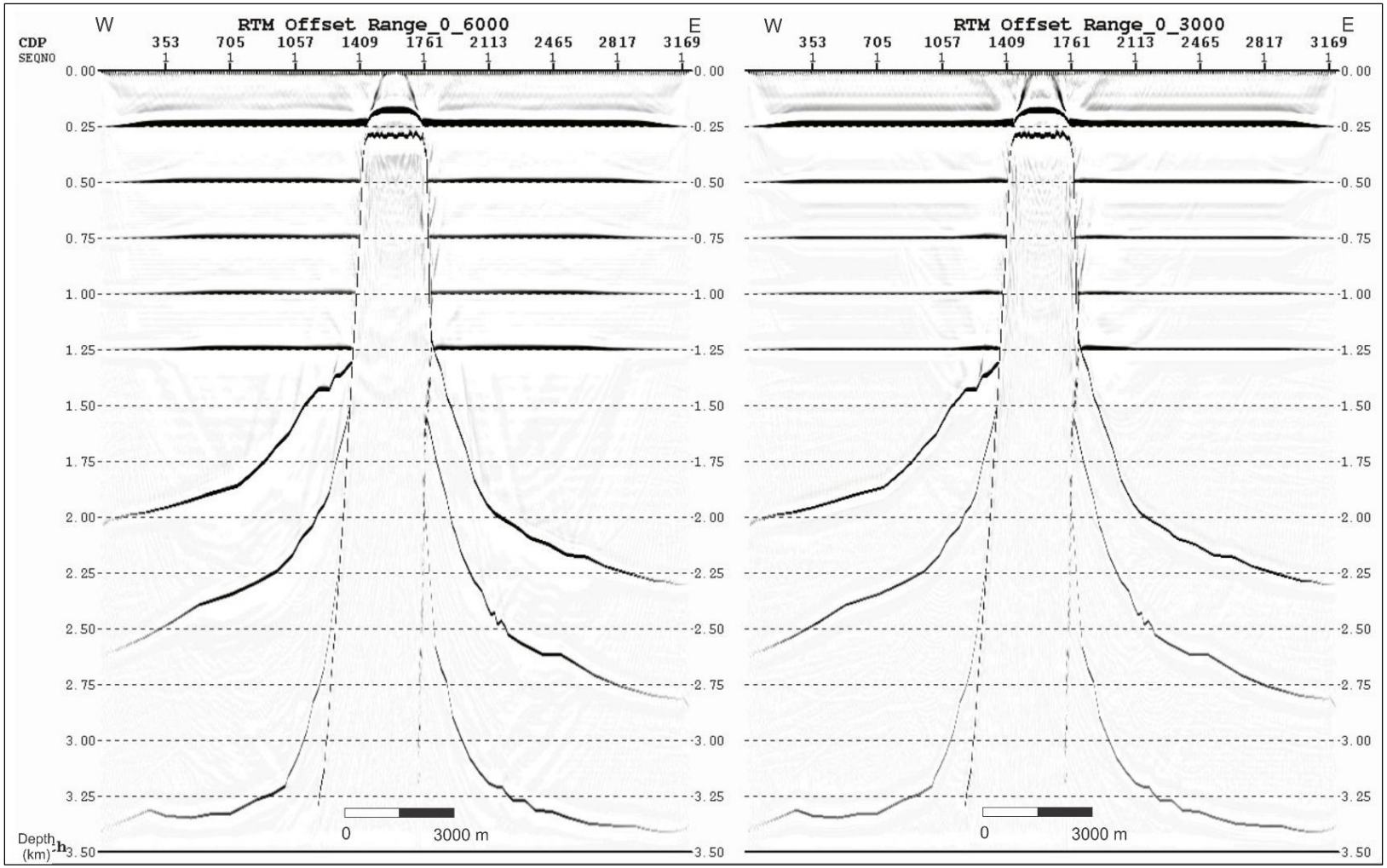

Figure 3.31. Comparison of RTM images obtained using the 0-6000 m and 0-3000 m offset ranges.

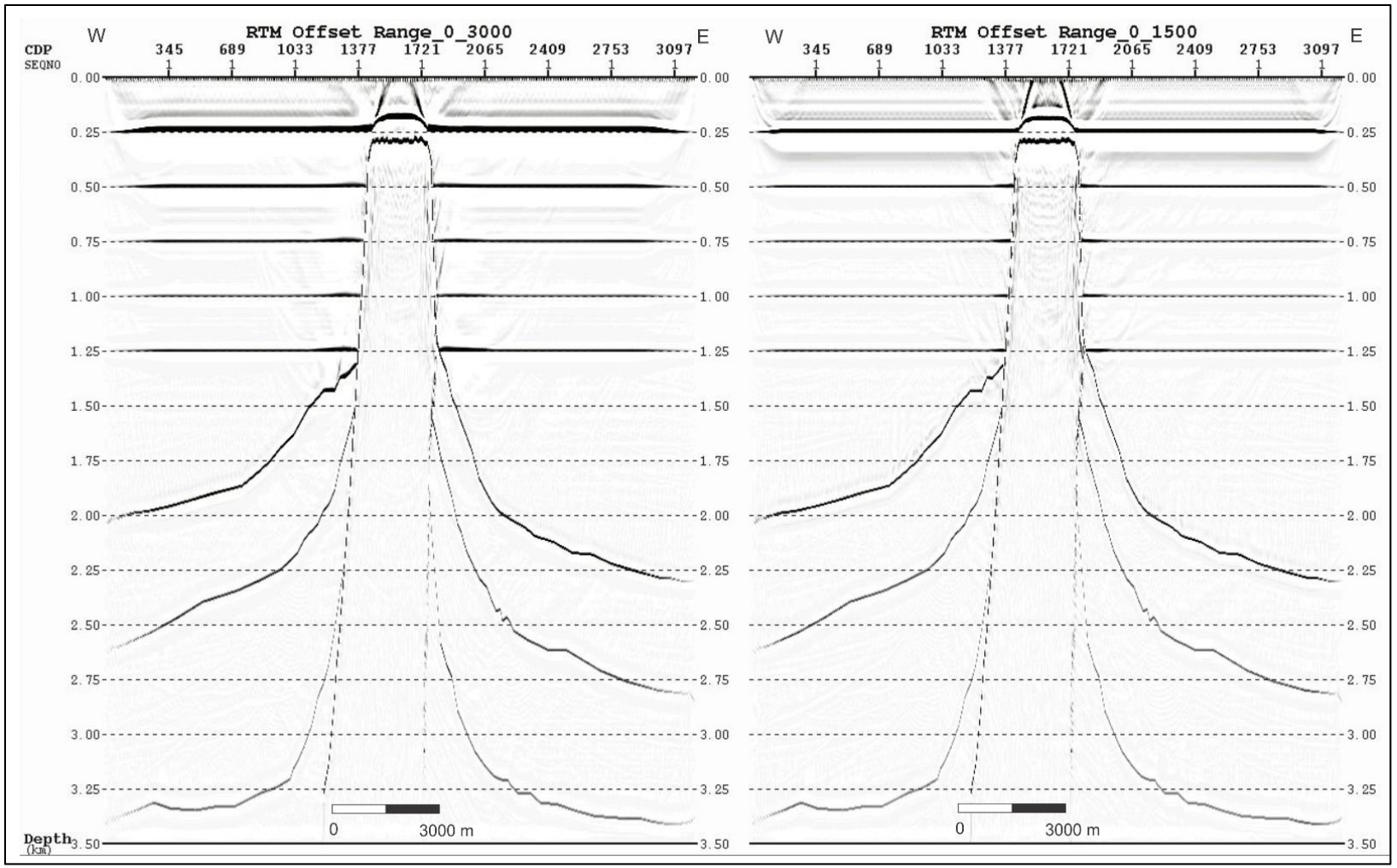

Figure 3.32. Comparison of RTM images obtained using the 0-3000 m and 0-1500 m offset ranges.

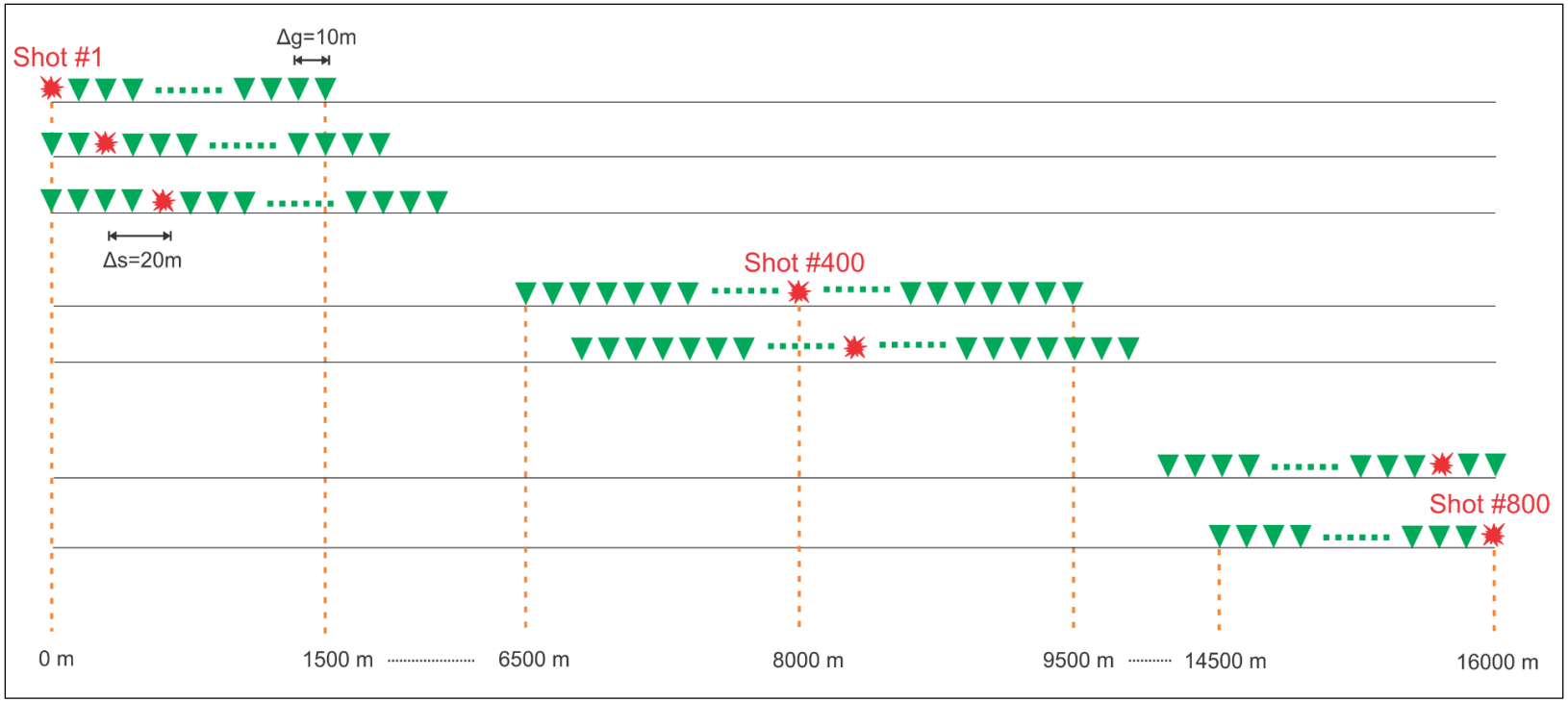

Figure 3.33. Survey layout after updating the maximum offset range. Green triangles and red stars represent the receivers and shots, respectively.

3.2.3.2 Group interval determination

As mentioned in 3.2.3.1, the number of receivers was reduced to 300 by the maximum offset minimization. The maximum group interval was another parameter that determined the number of receivers. In initial survey parameters, the maximum group interval was selected as 10 m due to the spatial aliasing limit. However, for such complex models it is possible to obtain a larger group interval by testing the survey with seismic imaging in terms of resolution. Data were modeled with 10 m and 20 m group intervals to see the difference between two parameters. According to RTM images shown in Figure 3.34, although the image obtained using a 20 m group interval showed some aliasing in certain areas, it still met our expectations for imaging the salt dome and surrounding sediments. Therefore, it was decided to update the group interval to 20 m. In this way, the number of receivers was reduced by half and the required limit of equipment was met. So, imaging tests for larger group intervals were not required, since the number of receivers was affordable.

3.2.3.3 Shot interval determination

The intervals between the shot stations are important to determine the fold of the survey. Smaller shot intervals provide better signal-to-noise ratios. The best way to determine a shot interval is doing field tests at the beginning of the survey. If necessary to skip field tests and having no information about a survey environment, shot intervals can be decided by seismic modeling and imaging tests.

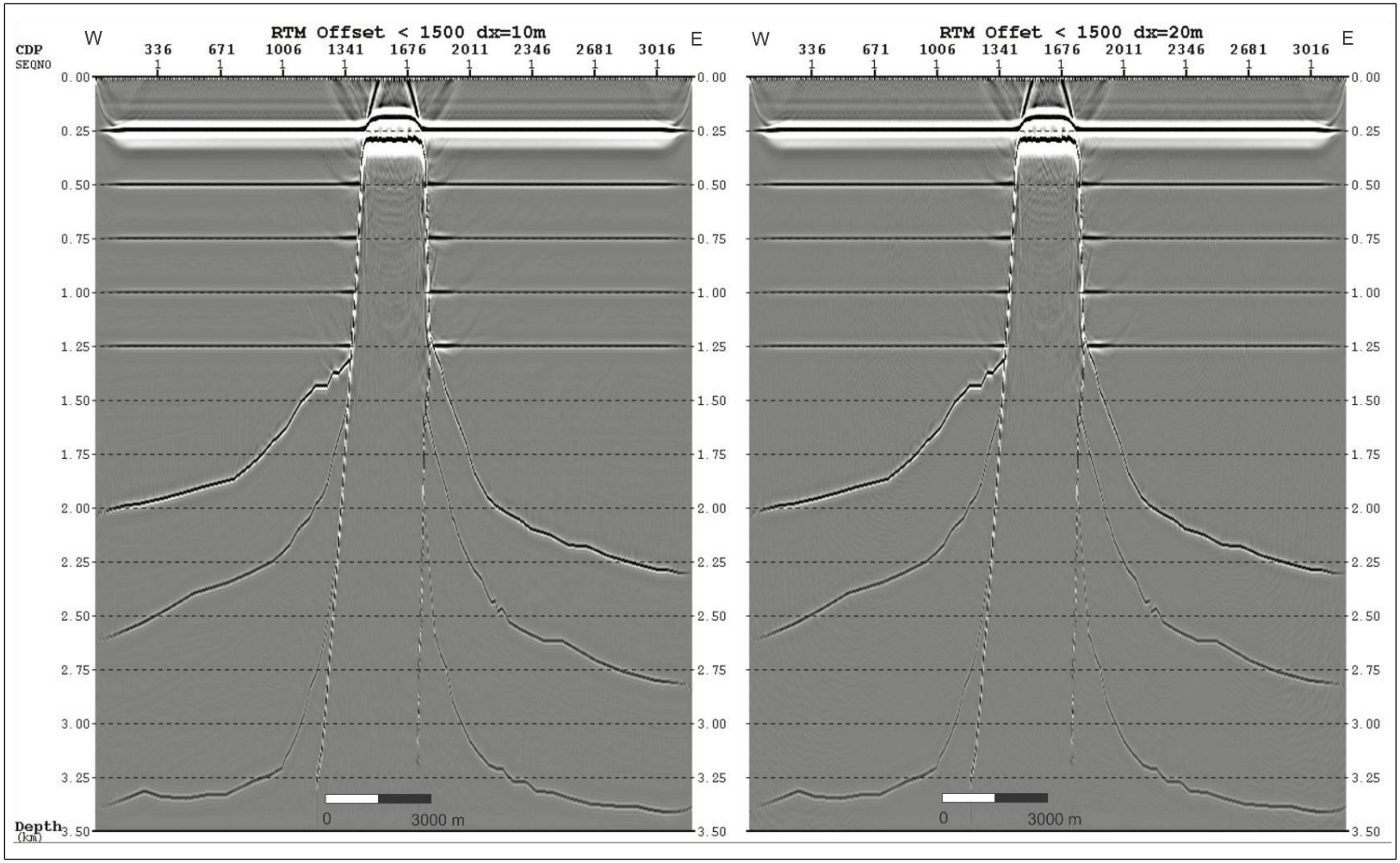

Figure 3.34. Comparison of RTM images that are modeled with 10 m (left) and 20 m (right) group intervals.

Also, it is possible to increase the number of vertical stacks to obtain a better signal-to-noise ratio without changing the shot interval, if the signal-to-noise ratio is lower than expected.

The shots were modeled with 40 m, 80 m, 160 m, and 320 m shot intervals to understand their effects on the data. As seen in Figure 3.35, the larger shot interval caused more noise in the image, especially in the shallower parts. However, none of the four RTM images showed much difference in the deeper parts of the data, which is the area of interest for this survey. Random noise which was not taken into account in this analysis could change the image quality. Therefore, the shot interval used was 40 m, to keep the fold as high as possible. According to updated parameters, the maximum fold of the survey was calculated as 37.5.

3.2.3.4 Record length determination

Record length is one of the parameters that directly affects survey duration. Optimum record length should be long enough to record any diffraction patterns coming from the deepest event of interest in order to perform a successful migration. Shots were modeled with shorter record lengths in order to update the initial record length of the survey to the optimum record length. The goal of this process is determining the shortest recording time that allows us to image the target zones without losing important events. RTM images of modeled shots with 8 s, 4 s, 3 s, and 2 s record lengths were compared with each other. As seen on Figure 3.36, an 8 s record length is unnecessarily long, since

the image of the data modeled with a 4 s record length already meets the same imaging needs. On the other hand, the data below 2.25 km could not be imaged, since a 2 s record length is very short for recording the diffractions coming from the deeper events required for migration. Images with 3 s and 4 s record lengths were examined in terms of data resolution. Figure 3.37 shows that the data modeled with a 3 s record length is not capable of imaging the salt flanks and steeply dipping layers in deeper parts. However, there is not much difference in resolution between two images at depths above 2 km. Thus, a 3 s record length is a suitable selection, if the area of interest is between 0-2 km depth. Record length was determined as 4 s for this study, in order to image the area down to 3.5 km.

3.2.3.5 Profile length determination

Analyzing the length of a profile by seismic imaging is a useful strategy for survey cost reduction. The shot spread length can be limited according to the imaging needs of the survey. The goal of our survey was to image the salt dome and surrounding sediments clipped at the flanks of the salt. Therefore, imaging the sediment layers far from the salt dome was not required. Establishing the optimum shot spread length was possible by imaging the data with different shot ranges. 0 – 800, 101 – 700, 201 – 600, and 301 – 500 shot ranges were imaged with updated survey parameters in order to find out the shortest shot spread length that provided the imaging needs of the survey. Figures 3.38 and 3.39 show that shot spread lengths between 0-800 and 101-700 provided larger seismic images than necessary. On the other hand, the resolution of the image obtained

using the 301 – 500 shot range was very poor for illuminating the steep dipping events (see Figure 3.40). Consequently, the 201-600 shot range equal to 8 km was chosen as the optimum shot spread length. After determining the shot spread profile, length of the survey was calculated as 11 km, as shown in Figure 3.41.

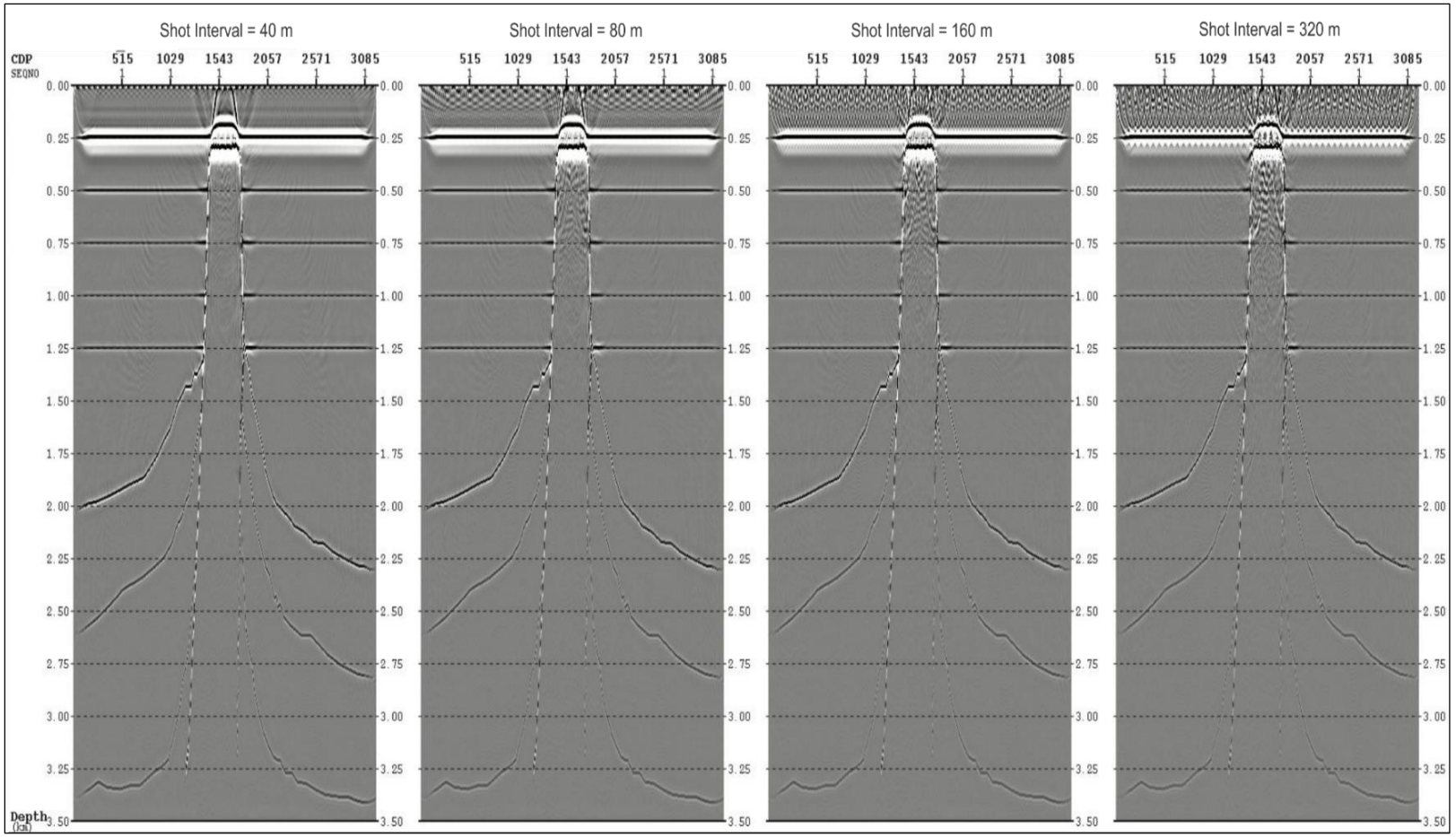

Figure 3.35. Comparison of RTM images that are modeled with 40 m, 80 m, 160 m and 320 m shot intervals.

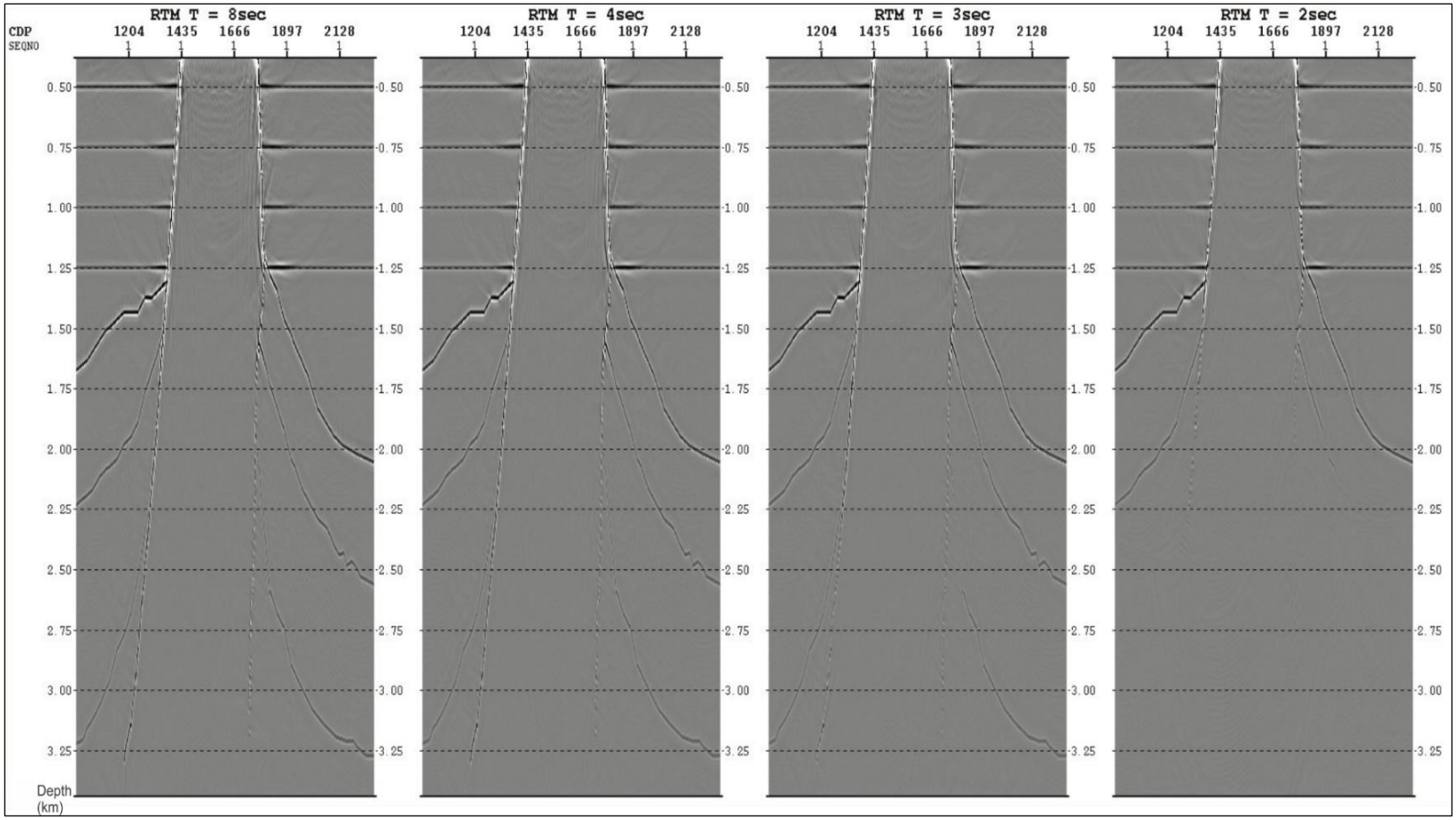

Figure 3.36. Comparison of RTM images that are modeled with 8 sec, 4 sec, 3 sec, and 2 sec record lengths.

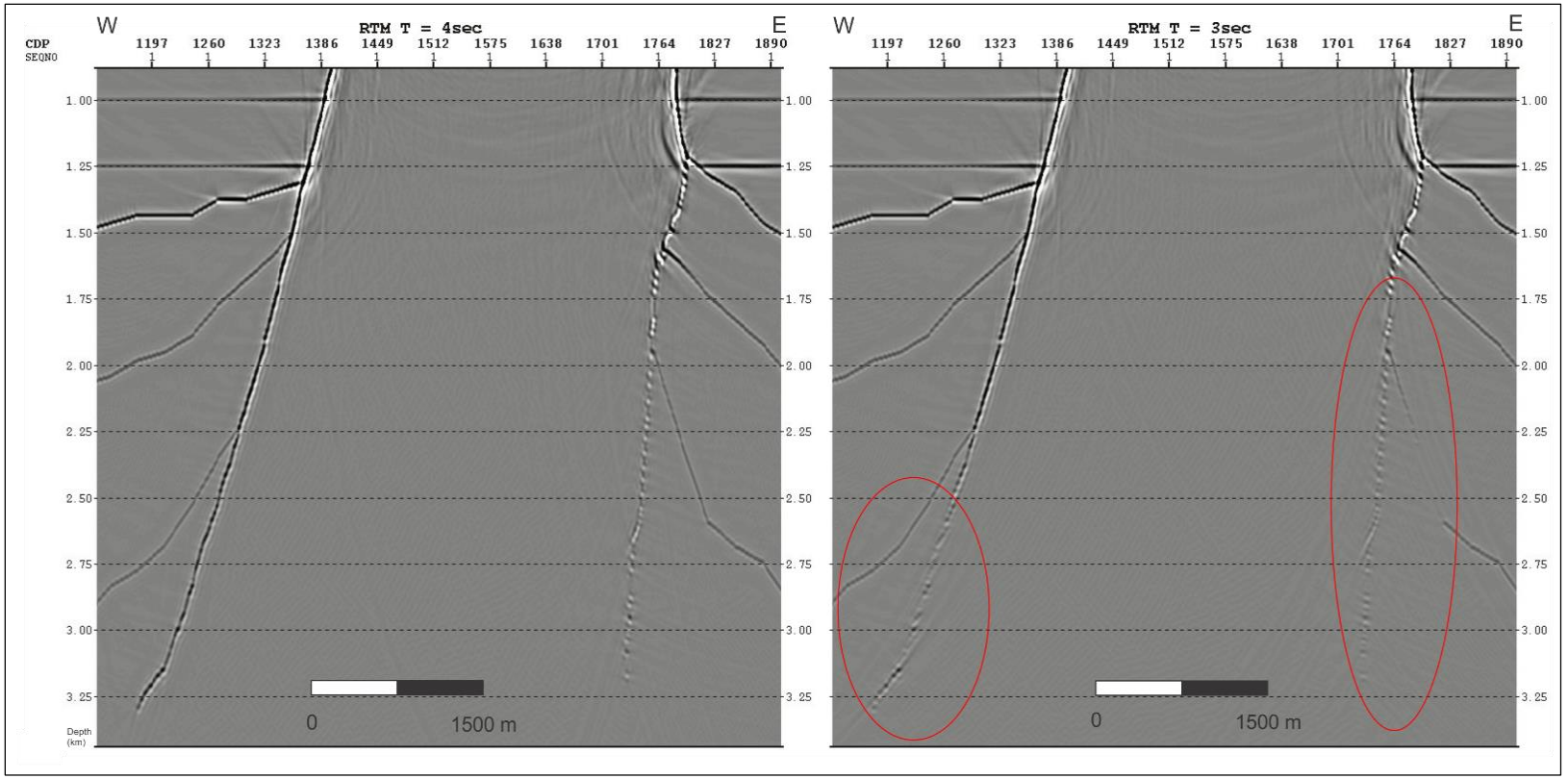

Figure 3.37. Comparison of RTM images that are modeled with 4 sec and 3 sec record lengths. Red circles highlight the poorly imaged areas.

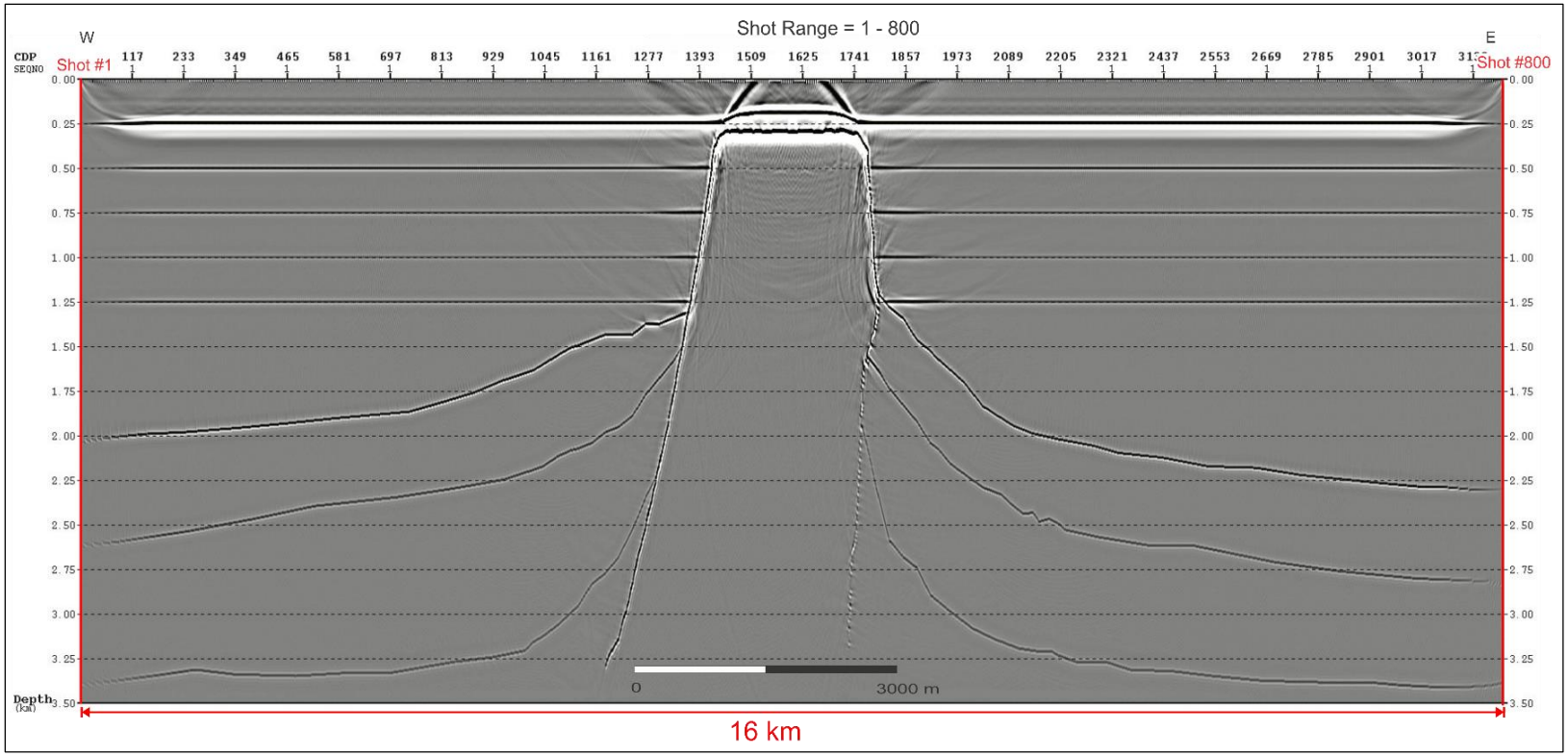

Figure 3.38. RTM image that is modeled with a 1-800 shot range.

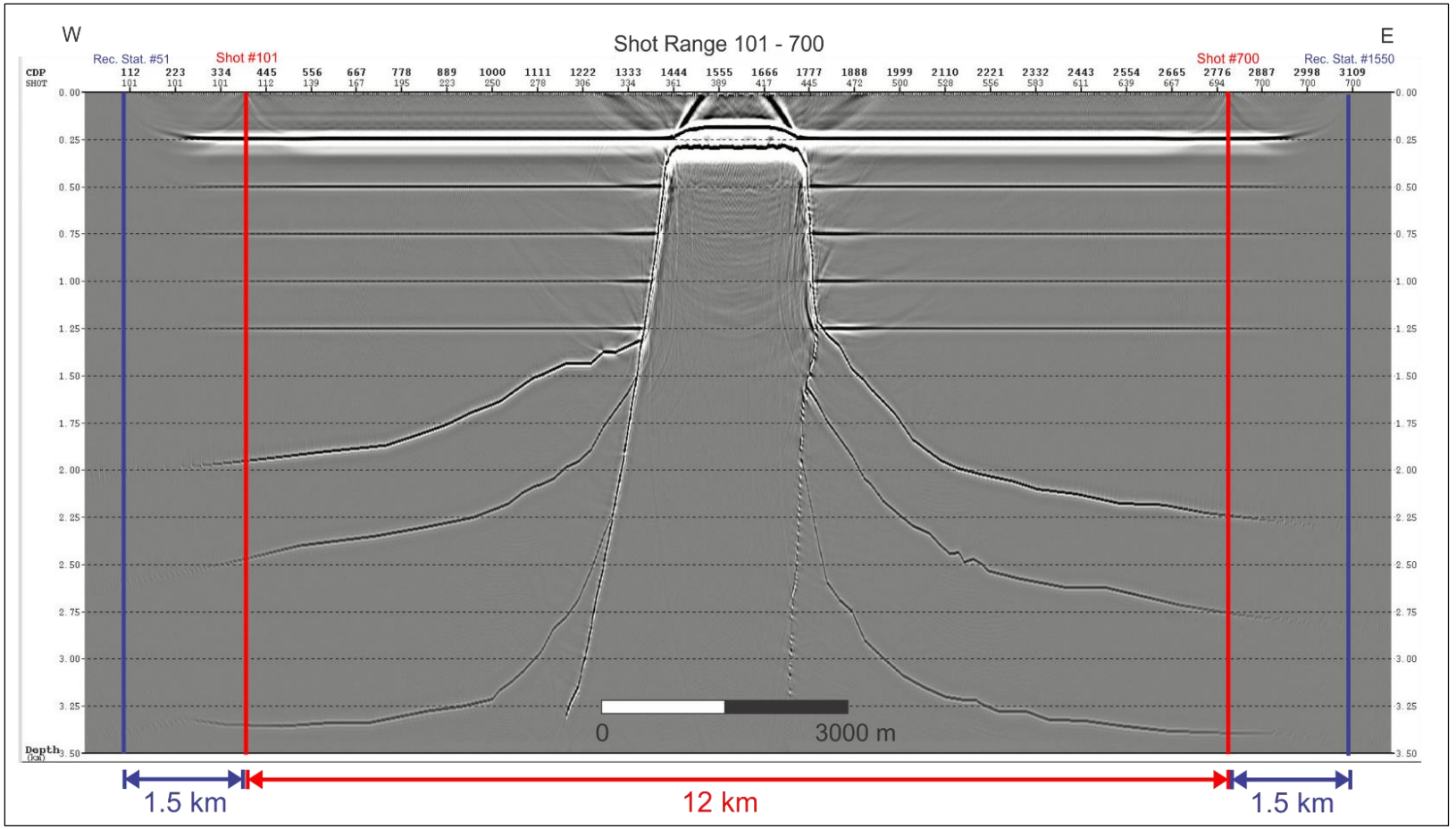

Figure 3.39. RTM image that is modeled with a 101-700 shot range.

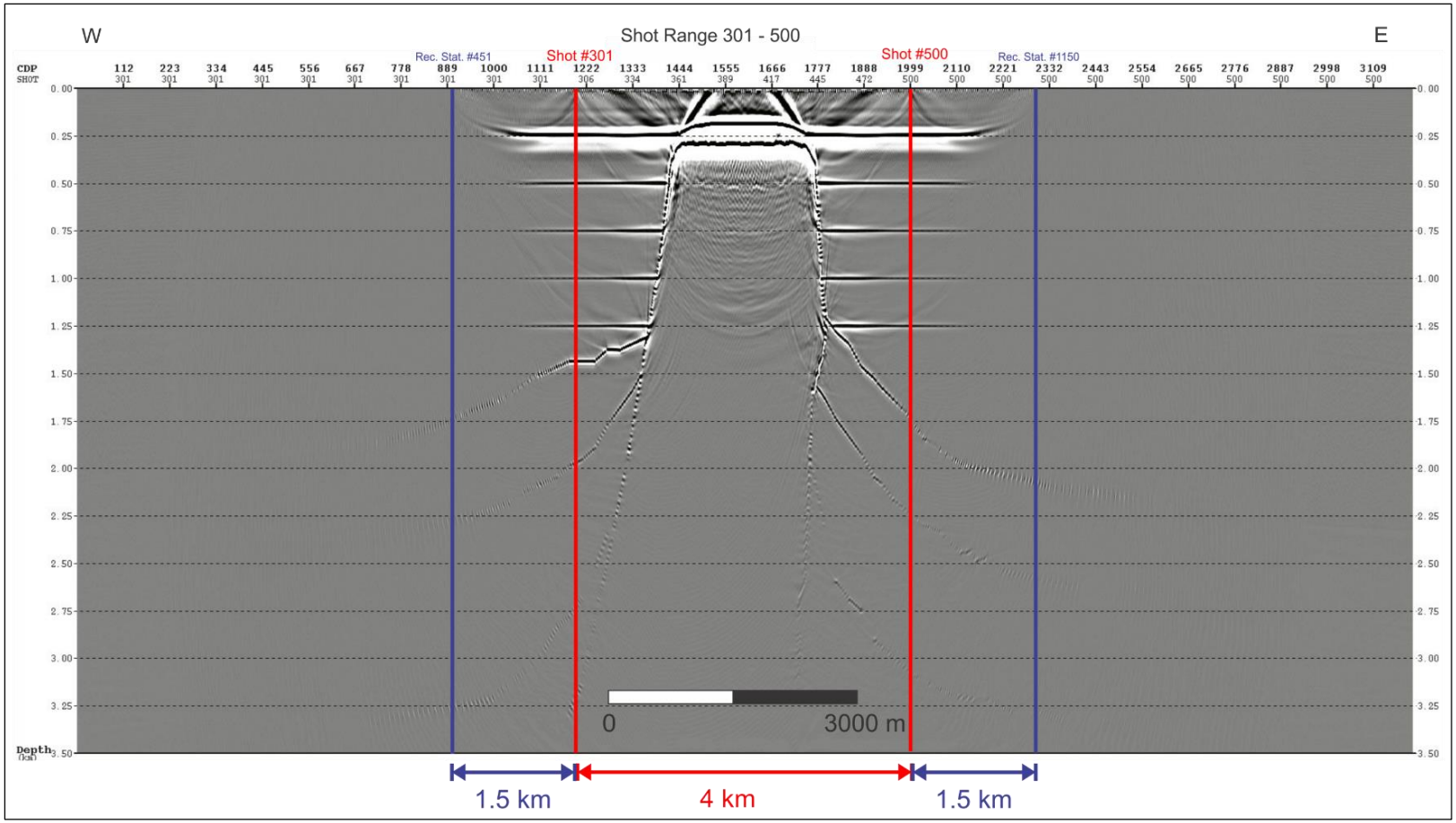

Figure 3.40. RTM image that is modeled with a 301-500 shot range.

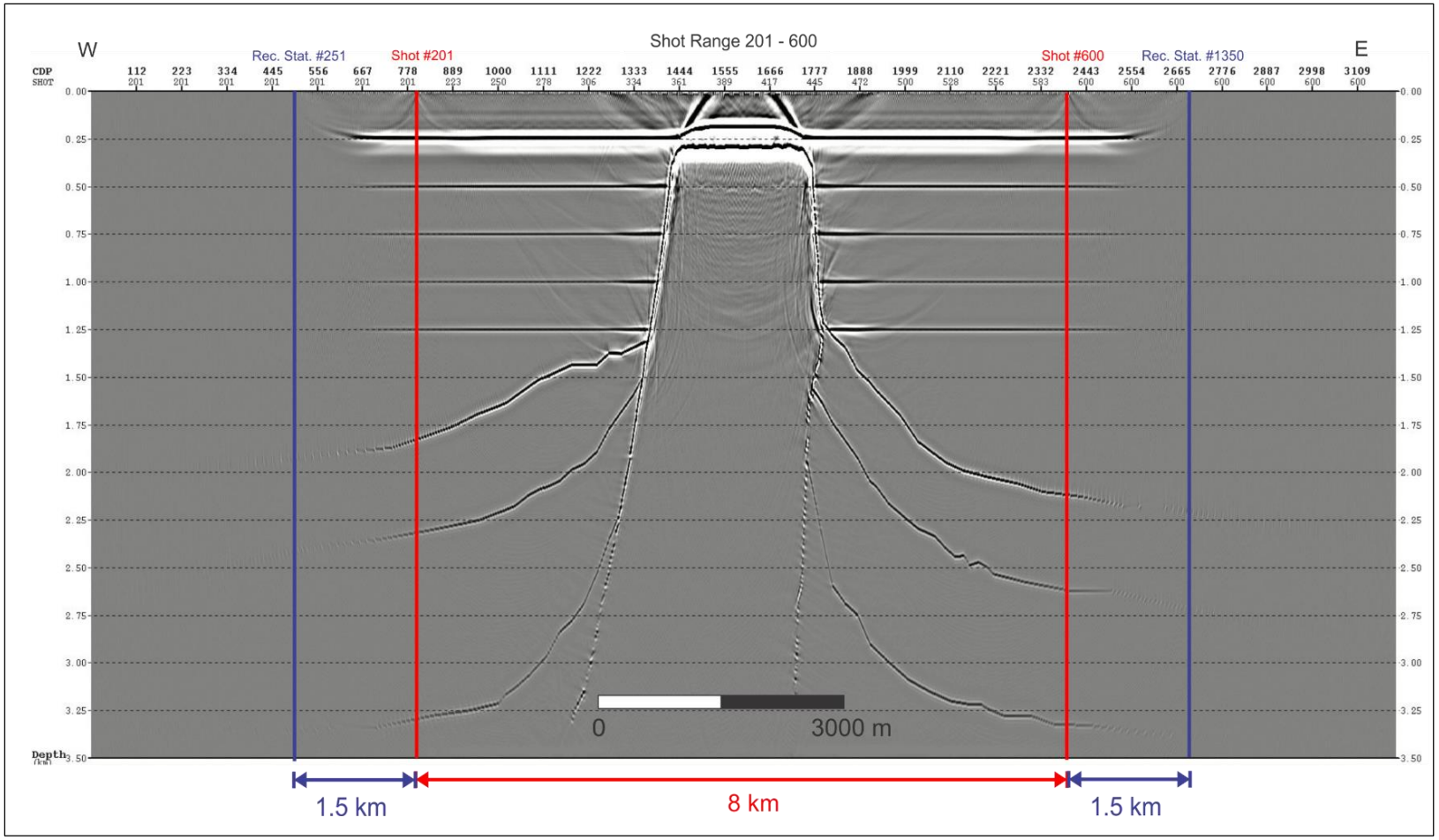

Figure 3.41. RTM image that is modeled with a 201-600 shot range.

3.2.4 Analyses of the 2-D Survey with Optimum Parameters

The new survey designed with RTM imaging was analyzed in terms of fold, resolution, illumination, and offset distribution. Final parameters of the new survey are given by Table 3.3.

Table 3.3. Acquisition parameters of new 2-D seismic survey.

Number of Receiver Stations	550	**Number of Shots**	200
Number of Receivers	150	**Receiver Interval**	20 m
Shot Interval	40 m	**Shot line length**	8000 m
Receiver line length	11000 m	**Sampling rate**	1 ms
Recording length	4 s		

The maximum fold of the survey was calculated as 38. This fold value is very small when compared with the maximum fold of the actual survey. But, unlike the actual survey, the fold was consistent at that maximum value throughout the profile. For this reason, the data quality of the new 2-D survey was expected to be better than the actual survey, since the fold was uniformly distributed. Survey geometry and fold distribution of the new survey is shown in Figure 3.42. As seen on the trace count-offset histogram of the new survey, the number of traces that fall into each offset bin is identical and higher than that of the actual survey as a result of rolling the receiver line with every shot along the profile (see Figure 3.43).

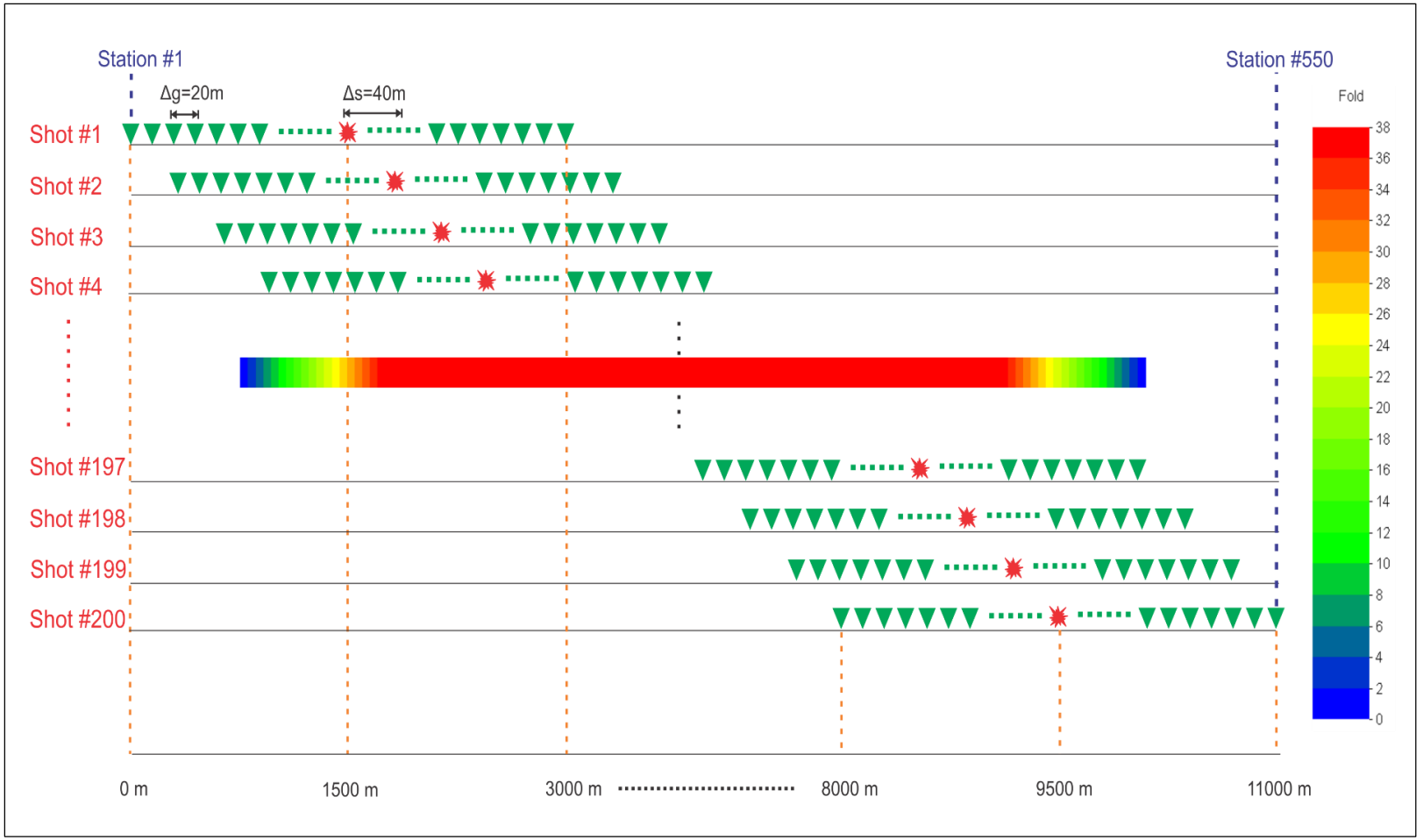

Figure 3.42. Survey geometry and fold distribution of the new 2-D survey.

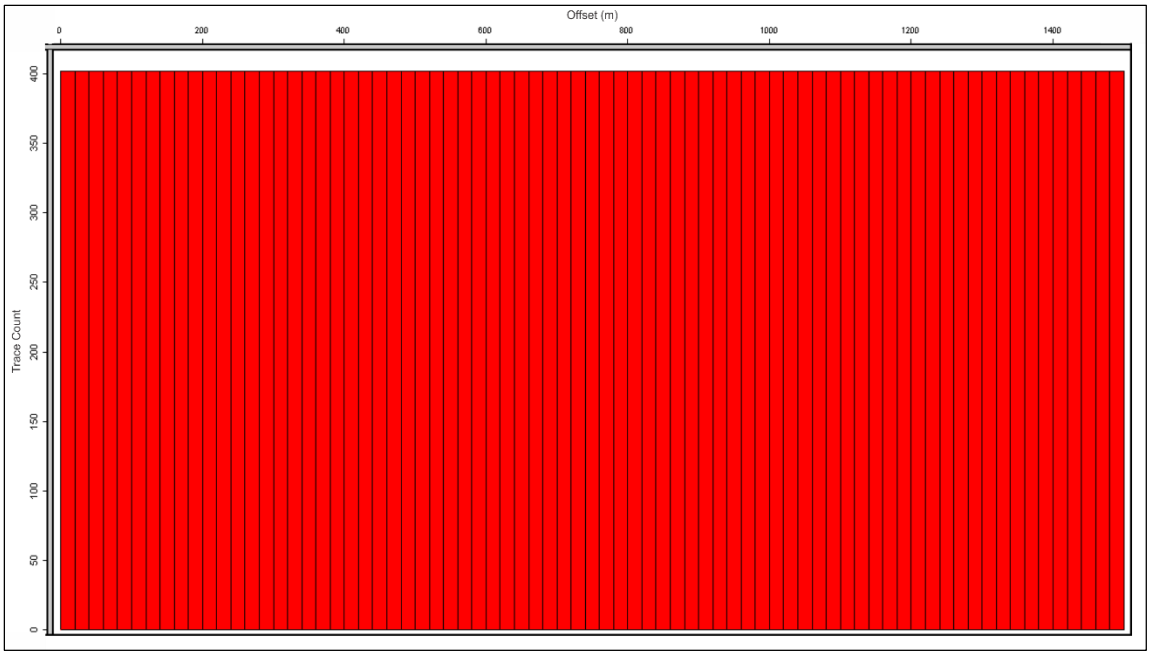

Figure 3.43. Trace count-Offset histogram of the new 2-D seismic survey. The chart shows the number of traces that fall in each range of offset values.

3.3 Three-D Seismic Survey Design via Modeling and RTM Imaging

3.3.1 Fundamentals of 3-D Seismic Survey Design

The basic concepts used for 2-D seismic surveys are used for 3-D seismic surveys as well. However, analyses of 3-D survey designs are more complicated, since the source and receiver arrays are not in-line as they are in 2-D surveys. Unlike in 2-D surveys, there are a number of source and receiver lines in 3-D surveys. Also, the source and receiver lines in 3-D surveys are mostly distributed orthogonally to each other; therefore, the source and receiver lines must be defined separately in 3-D.

The surface coverage in 2-D designs is defined by common-depth-points (CDPs). In contrast, the surface coverage of 3-D designs is described with square or rectangular

areas called bins. Spatial resolution of data sampling is dependent on the bin size decided for a survey (Stone, 1994). The importance of bin size selection is highlighted in 3-D survey design concepts. Also, most concepts in 2-D design are altered with the bin concept since they are eventually transferred into three dimensions.

The definitions of basic concepts in 3-D survey design can be presented in an orthogonal geometry, the most common geometry used for onshore 3-D seismic surveys. In this geometry, the receiver and source lines are laid out at right or normal angles to each other as shown in Figure 3.44.

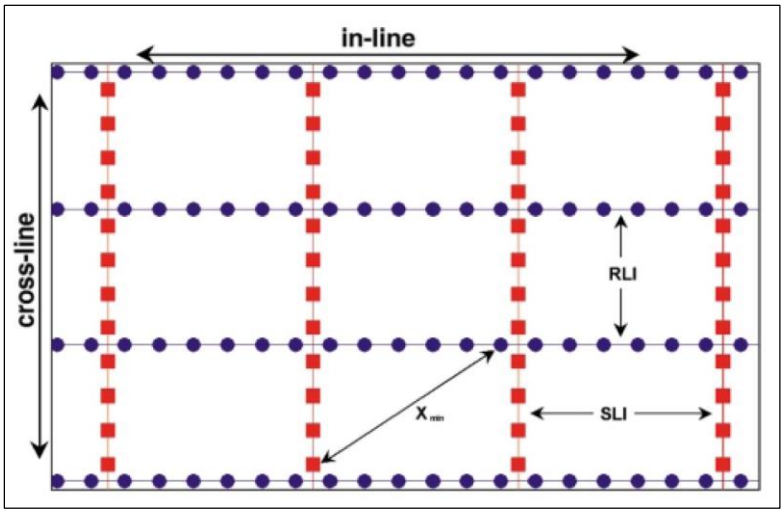

Figure 3.44 Elements of orthogonal geometry. Red squares and blue circles represent the source and receiver locations, respectively (modified after Cordsen et al., 2000).

3.3.1.1 Fold in 3-D

As mentioned in sub-section 3.2.1.5, fold is one of the parameters that affects signal-to-noise ratio. The fold and signal-to-noise ratio relationship expressed by Cordsen (2000) is presented in Figure 3.45. In the 3-D case, fold is defined by the number of

stacked traces in a bin, which are from different sources and receivers having the same midpoint reflection. The relationship between 2-D and 3-D folds is basically explained with frequency dependency by Krey (1987), using the following equation:

$$\boldsymbol{F_{3D} = F_{2D} \times f \times c} \quad , \qquad \text{Eq. 3.12}$$

where:

F_{3D} = fold in 3-D,

F_{2D} = fold in 2-D,

f = expected frequency, and

c = arbitrary constant.

A more complete approach of Krey for the relationship between 2-D and 3-D folds including CDP spacing, frequency, and average interval velocity can be expressed as:

$$\boldsymbol{F_{3D} = \frac{F_{2D} \times (bin_{3D})^2 \times f \times \pi \times 0.401}{CDP_{2D} \times V}} \quad , \qquad \text{Eq. 3.13}$$

where:

F_{2D} = fold in 2-D,

bin_{3D} = 3-D bin spacing,

f = frequency,

CDP_{2D} = 2-D CDP spacing, and

V = velocity.

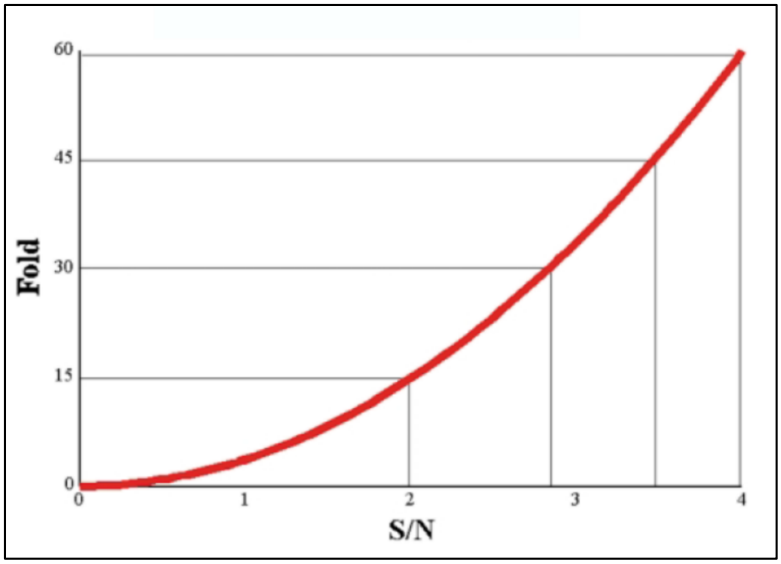

Figure 3.45. Fold versus signal-to-noise ratio (S/N), after Cordsen (2000).

Calculation of the average 3-D fold can be obtained using the eq. 3.13. One who wants to calculate the fold in detail should examine the in-line and cross-line components of the fold. The total fold of the survey is calculated combining the in-line and cross-line folds. The full stacking fold is defined by the maximum in-line and cross-line offsets along with the receiver and source line intervals. The station spacing influences fold indirectly since it modifies the bin size, the source density, and the number of channels required. Also, the required number of channels (NC) can be calculated if fold, bin size, source station, and line intervals are determined, as shown in the following:

$$\boldsymbol{NC = F_{3D} \times dx_{SL} \times dx_S \times B^2} \quad , \qquad \text{Eq. 3.14}$$

where:

F_{3D} = fold in 3-D,

dx_{SL} = source line interval,

dx_S = source interval, and

B = bin dimension for square bins (Cordsen et al, 2000).

3.3.1.2 Bin Size

For 3-D data, the bin concept is the main building block throughout a survey. The shape of the bin is usually selected to be a rectangle or square (Stone, 1994). Rectangular bins are preferred when the required lateral resolution in one direction is different from the required resolution of the other direction (Cordsen et al., 2000). Otherwise, square bins are popular for obtaining adequate spatial sampling in both dimensions.

According to Cordsen et al. (2000), the signal-to-noise ratio (S/N) is directly proportional to the length of one side of the bin for square bins (see Figure 3.46). The fold is a quadratic function of the length of one side of the bin.

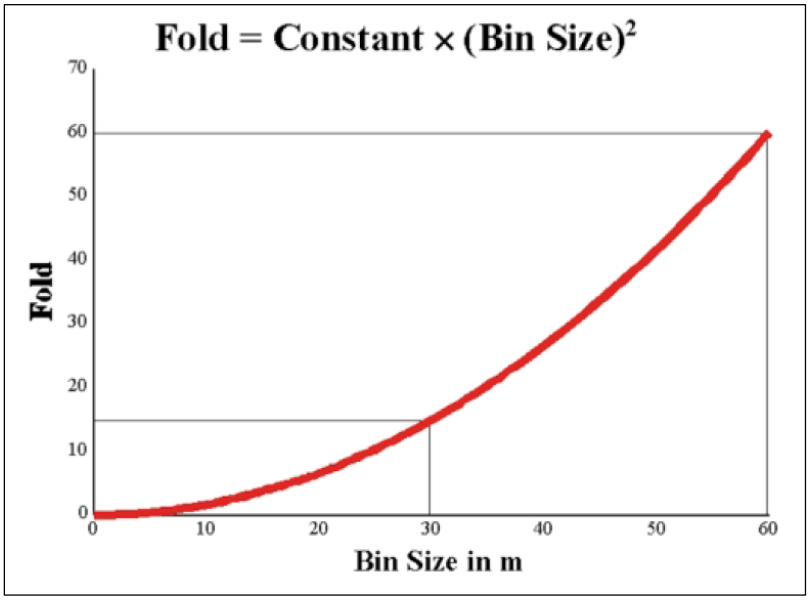

Figure 3.46. Fold versus bin size (after Cordsen et al., 2000).

Bin size is determined based on target size, maximum un-aliased frequency due to dip, and lateral resolution analyses. These analyses can provide different bin size values. Survey budget is another factor determining bin size proposed by different analyses.

The bin size of a survey using target size is expressed in Eq. 3.17 as proposed by Cordsen et al. (2000):

$$\boldsymbol{Bin\ size} \leq \frac{\boldsymbol{Target\ size}}{\mathbf{3}} \quad . \qquad \text{Eq. 3.17}$$

Existence of dipping layers in the survey area is also an important factor for determining bin size. The maximum possible un-aliased frequency before migration is related to the velocity of the target, the value of the geological dip, and the bin size. Different bin sizes can be obtained using maximum frequency-dip angle, and dip angle-bin tables. The equation for calculating the bin size for alias frequency is as follows:

$$\boldsymbol{Bin\ Size} = \frac{\boldsymbol{V_{int}}}{\mathbf{4}\times\boldsymbol{f_{max}}\times\mathbf{\sin\theta}} \quad , \qquad \text{Eq. 3.18}$$

where:

V_{int} = interval velocity,

f_{max} = maximum frequency, and

Θ = maximum dip angle.

Many researchers have recommended different definitions and equations for lateral resolution, such as Clearbout (1985), Embree (1985), Freeland and Hogg (1990), Ebrom et al. (1995), and finally Vermeer (1998). Cordsen et al. (2000) suggested using

Vermeer's equation to simply calculate bin size, assuming that lateral resolution can be between one quarter and one half the dominant wavelength, as follows:

$$\boldsymbol{Bin\ Size} = \frac{\boldsymbol{V_{int}}}{\boldsymbol{N \times f_{dom}}} \quad , \qquad \text{Eq. 3.19}$$

where:

V_{int} = interval velocity,

f_{dom} = dominant frequency, and

N varies from 2 to 4.

Note that calculated resolution is always better than actual resolution since there will be resolution loss due to noise. All bin size analyses give the maximum bin size for achieving the minimum acceptable resolution on target. Bin size should be adjusted according to budget of the seismic survey.

3.3.1.3 Minimum Offset (X_{min})

The largest minimum offset is the diagonal of the box described with coincident source and receiver stations at corners (see Figure 3.47). The receiver and source line intervals (RLI & SLI respectively) directly control the X_{min} value in many designs, such as in the orthogonal, brick, and zigzag designs (Cordsen et al., 2000). X_{min} can be calculated as follows:

$$\boldsymbol{X_{min}} = \sqrt{(\boldsymbol{RLI})^2 + (\boldsymbol{SLI})^2} \quad . \qquad \text{Eq. 3.20}$$

Having small X_{min} is important in order to sample the shallowest reflector wanted to be mapped in three dimensions. According to Vermeer (1999), at least four-fold multiplicity is necessary to have enough confidence in a correct interpretation at a shallow horizon. The four-fold formula for symmetric sampling at mute distance X_{sh} is defined using the following:

$$\boldsymbol{X_{sh} = RLI \times 2 \times \sqrt{2} = 2 \times X_{min}} \quad . \qquad \text{Eq. 3.21}$$

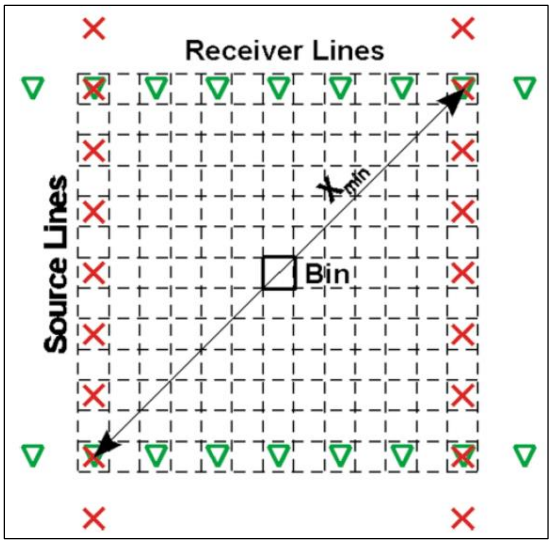

Figure 3.47. X_{min} definition with coincident source and receiver stations at corners of box (Cordsen et al., 2000).

3.3.1.4 Maximum Offset (X_{max})

An adequate maximum offset selection is needed to record the traces coming from deeper horizons. The maximum recorded offsets are affected by the processing mute of the far offsets as well. Muting the traces within a given bin will decrease the fold coverage of a related bin. So the X_{max} should be determined very carefully to keep the fold value stable. The fold within a circle of radius R is defined by:

$$\boldsymbol{Fold} = \frac{(\boldsymbol{SD}\times\boldsymbol{NC}\times\boldsymbol{B}^2)}{\boldsymbol{Patch\ Size}} \quad , \qquad \text{Eq.3.22}$$

where:

SD = source density,

NC = number of channel, and

B = bin size.

As shown in Figure 3.48, R represents the X_{max} and it is always advantageous to determine the X_{max} along the diagonal of the patch. If X_{max} is determined as the in-line maximum offset, some traces will be muted; otherwise, all traces will be used in the stack. Also, using diagonal measurement will give a uniform offset distribution (Cordsen, 1995).

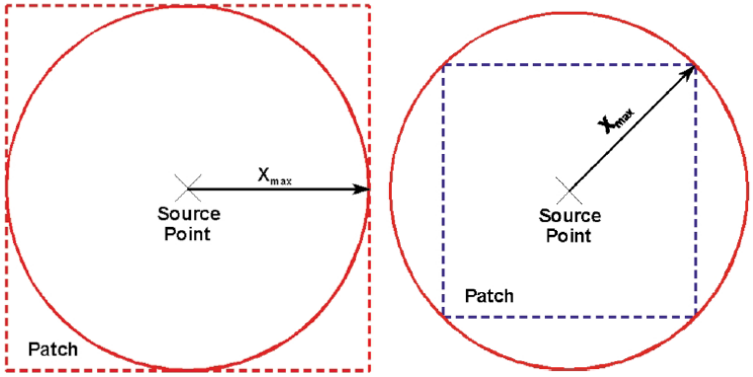

Figure 3.48. Definition of X_{max} two different approaches. In-line maximum offset (left) and diagonal maximum offset (right), after Cordsen et al. (2000).

Another approach to determine the X_{max} is to trace the rays on geological models. Conversion of reflected energy to refracted energy can be examined for each event in a model. Then suitable X_{min} and X_{max} values can be determined for an entire model.

3.3.1.5 Offset Distribution

Each CMP bin stores many midpoints associated with different offsets and azimuths from the source to the receiver. The offset distribution is directly related to the fold. Higher folds always show better offset distribution. The main goal for a designer is to obtain a good mix of far and near offsets for each CMP bin.

3.3.1.6 Azimuth Distribution

Like the offset distribution, the azimuth distribution is also controlled by the fold. A good azimuth distribution allows to recording of data having azimuth-dependent variations, such as anisotropy and/or dipping. The general rule to achieve a good azimuth distribution is keeping the aspect ratio between 0.6 and 1.0.

3.3.1.7 Recording Time

The minimum recording time for 2-D surveys is already explained in sub-section 3.2.1.4. The vertical travel time calculation will not be sufficient to record the diffractions from the deepest event in a 3-D survey. Additionally, dip requirements, static shifts, multiples, and NMO reflections should also be considered. According to Margrave (1997), the minimum recording length (t) should be calculated as follows:

$$\boldsymbol{t} = \frac{\boldsymbol{2Z}}{\boldsymbol{V}\cos\boldsymbol{\theta}} \quad , \qquad \text{Eq. 3.23}$$

where:

Z = depth, and

V = interval velocity.

3.3.1.8 Ray Trace Modeling

Ray trace modelling is one of the most useful methods to test the acquisition parameters so as to build an accurate geological model. Areas with complex geology, such as salt domes, faults, steeply dipping layers, and lateral velocity discontinuities, can be analyzed in terms of illumination by ray tracing. Using the ray tracing method allows detection of the areas where illumination is required. Then, receiver and/or source intervals may be updated according to the imaging needs of the model (Neff and Rigdon, 1994).

3.3.2 3-D Seismic Survey Design using RTM Cases

The optimum parameter considerations and observations of the 2-D survey design in sub-section 3.2.3 provided insights for determining the best 3-D design. However, there are some parameters not applicable in 2-D to be determined for 3-D survey design, such as survey geometry, regularity, offset and azimuth distributions, and fold in 3-D. In this sub-section, the parameters determined using RTM images in 2-D were modified for a 3-D seismic survey. Therefore, optimum survey parameters to image the salt structure in 3-D will were obtained.

3.3.2.1 Survey Geometry

There are many survey geometries that can be applied to 3-D surveys, such as swath, orthogonal, brick, non-orthogonal, zig-zag, and star. Each geometry has

advantages over others, and need selecting according to survey objectives. Among popular 3-D survey geometries, we found orthogonal geometry more advantageous for our study. In terms of cost effectiveness, orthogonal geometry is superior to parallel (swath) geometry. On the other hand, zig-zag geometry is more economic in open areas, such as deserts. All the other geometries usually do not provide desirable resolution and spatial continuity (Vermeer, 2002). Furthermore, survey and recording crews can make arrangements easily for deploying the equipment ahead of shooting and roll-along operations in orthogonal geometry (Cordsen et al., 2000). These advantages made us choose orthogonal geometry.

3.3.2.2 Dimensions of the Survey Area

The size of the survey area was determined by reviewing the 2-D survey parameters. An 8 km by 8 km square survey area was considered adequate for imaging the salt structure and surroundings, since the salt model is in the center, circular, and there is no rooting in any direction.

Distances between the source and receiver lines determine the largest minimum offset (X_{min}) important to record shallow events. The source and receiver line intervals were selected as 250 m. Hence, X_{min} of the survey was calculated as 327 m, which is small enough to sample shallow reflectors adequately. As a result, 33 in-lines and 33 cross-lines were distributed over the survey area with equal intervals; this is shown in Figure 3.49.

3.3.2.3 Patch (Template) Description

The patch is defined as the distribution of the active receivers that corresponds to one shot point in the survey. It is moved after each salvo along the survey and the survey area is covered by the overlapping patches. Patches can be rolled along in-line or cross-line directions (Chaouch and Mari, 2006). The number of active receivers, group and shot intervals, in-line and cross-line intervals, and maximum offset should be described so as to define the patch of the survey.

In 3-D surveys, shot and group intervals are usually selected to be coarser than those in 2-D surveys in order to decrease survey cost. On the other hand, intervals should be decided appropriately to resolve structural dips and to ensure the imaging needs (Cordsen et al., 2000).

Although our RTM images of the 2-D survey showed that increasing the group and shot intervals is possible, choosing very large intervals can affect the imaging objectives. Therefore, group and shot intervals were slightly increased to 25 m and 50 m, respectively. Square CMP bin dimensions were determined as 12.5 m, which is one-half length of the group interval. The patch includes 3000 m-long 13 in-lines (receiver line) and 33 cross-lines (shot lines) to keep the aspect ratio at 1:1. Eventually, the number of geophones required for such a survey was calculated to be 1573. Table 3.4 summarizes the parameters of the patch used for the 3-D survey. Also, illustration of the parameters is shown in Figure 3.50.

Table 3.4. Table summarizing the 3-D acquisition parameters.

Receiver line direction	E-W	**Source line direction**	N-S
Receiver interval	25 m	**Shot interval**	50 m
Receiver line interval	250 m	**Shot line interval**	250 m
Length of the receiver line	3000 m	**Length of the shot line**	3000 m
Number of channels	1560	**Number of Receivers per line**	121
Aspect ratio of the patch	1	**Number of shots**	10583
Shot Density (Source per km^2)	83	**Bin shape and size**	Square 12.5 m x 12.5 m

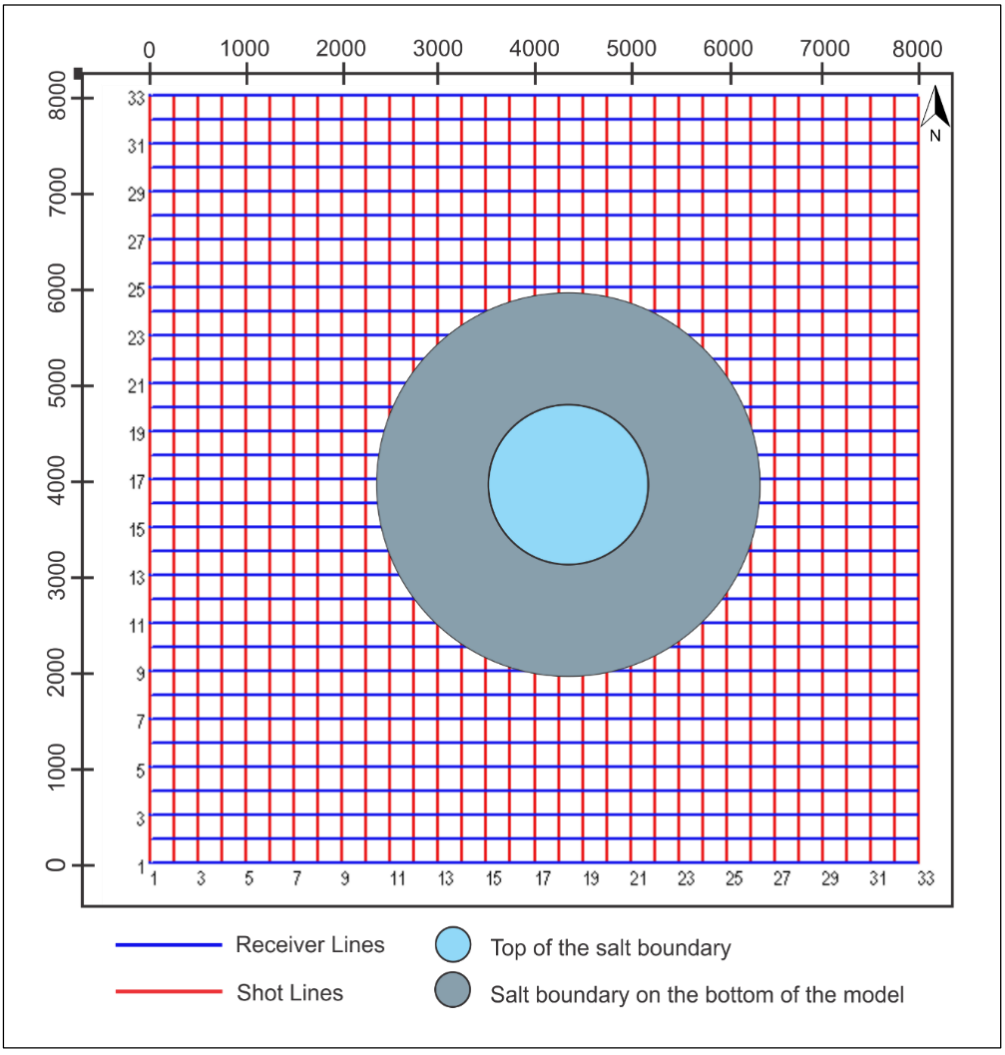

Figure 3.49. Designed 3-D survey area. Red and blue lines represent the shot and receiver lines, respectively. Boundary of the salt at the top and bottom of the model is shown by blue and grey circles, respectively.

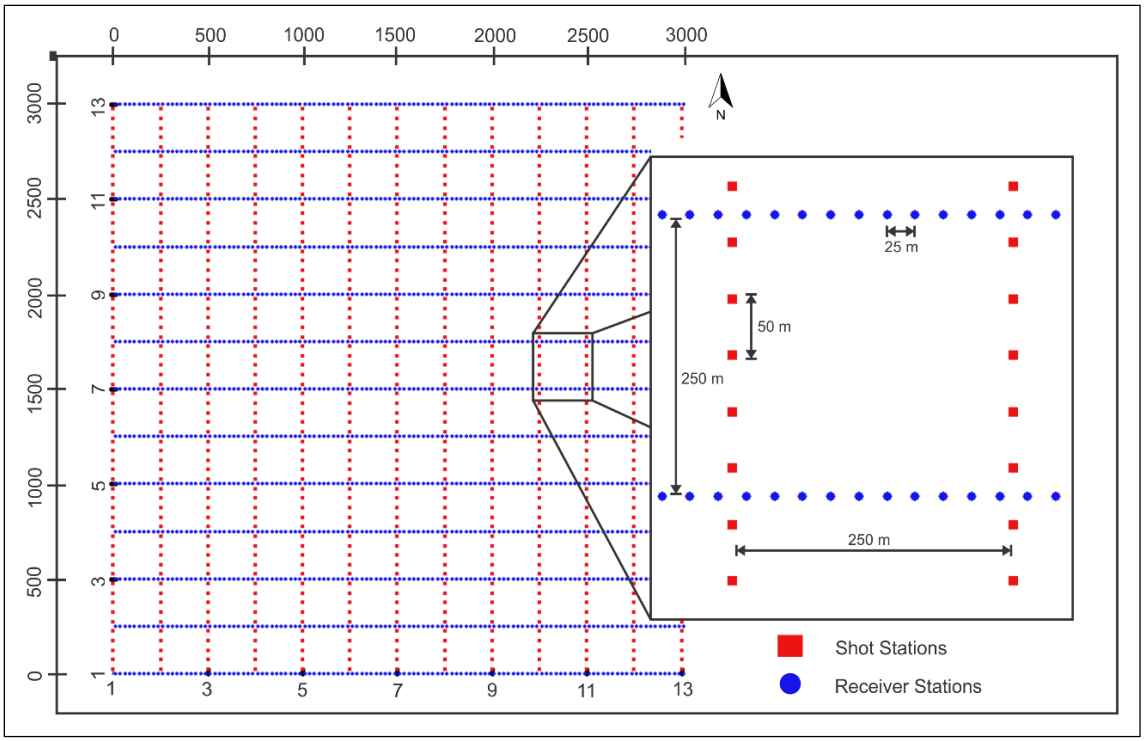

Figure 3.50. Definition of the 3-D patch. Red squares and blue circles represent the shot and receiver stations, respectively.

3.3.2.4 Analyses of 3-D survey with optimum parameters

Once the acquisition geometry and parameters were determined, the survey was analyzed based on the fold, offset and azimuth distribution, and shot contribution. The maximum total fold of 49 was uniformly distributed over the survey area. However, it is decreasing at the edges of the box, since the number of active receivers is decreased at the corners and the edges of the survey area, due to the shooting pattern. Figure 3.51 shows the number of receiver lines that have active stations for each shot. Nevertheless, 76.5% of the area is covered by the maximum fold appropriate for imaging the salt dome and its surroundings. Also, even the fold values are less than the maximum at the sides of

the area, and they have remarkable contributions to the data in the imaging process. The fold distribution of the survey is shown in Figure 3.52.

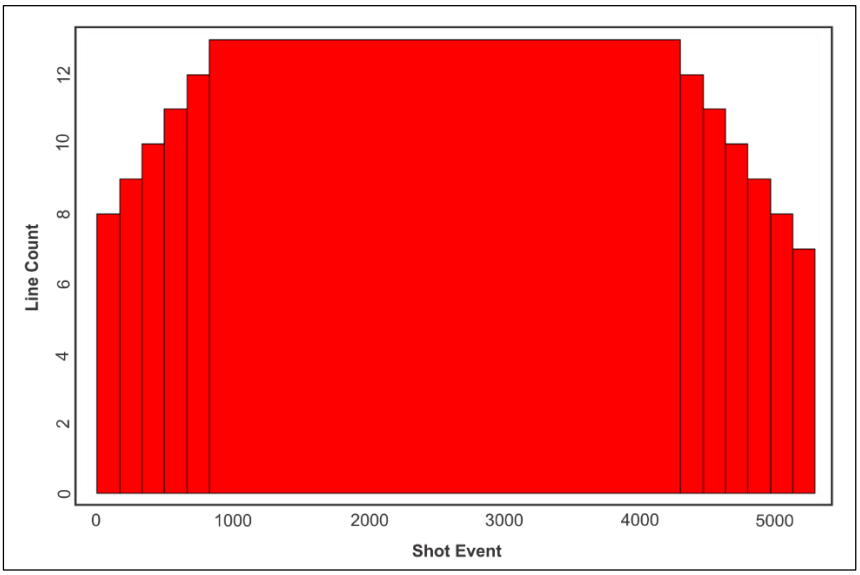

Figure 3.51. Line Count-Shot Event chart of the 3-D survey. The chart shows how many receiver lines have active stations for each shot event.

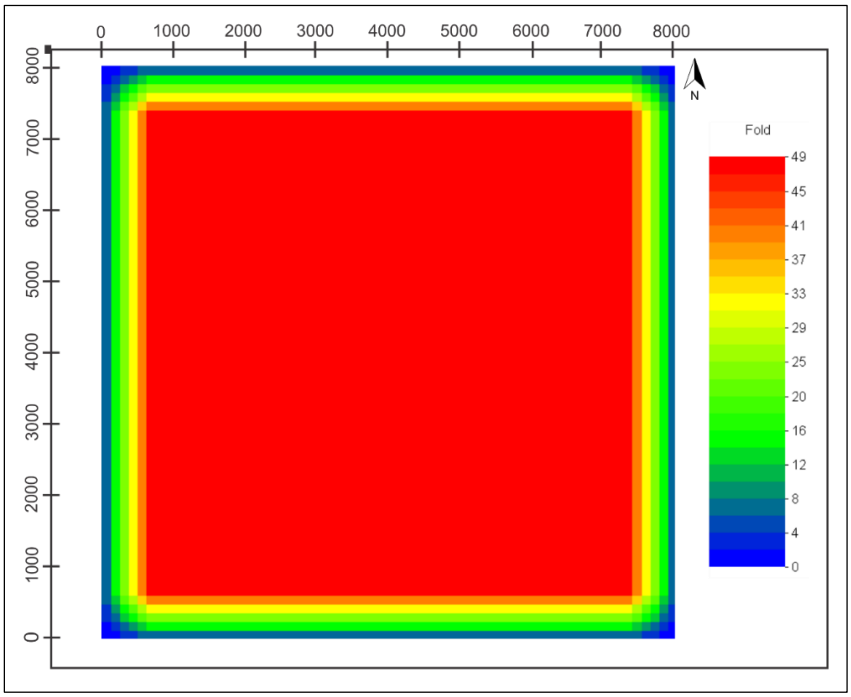

Figure 3.52. Fold distribution of the 3-D survey.

The data acquired with poor offset distribution usually cause problems and limitations in processing and interpretation (Wright, 2003). It is always better to examine the fold distribution while designing the survey. In this study, the offset distribution of the designed survey was examined using a Trace Count–Offset plot. As expected, a regular offset distribution was observed, since the aspect ratio of the patch is 1:1. As seen in Figure 3.53, the number of traces that fall in each bin of offset value is high enough to make valuable contribution to the final image.

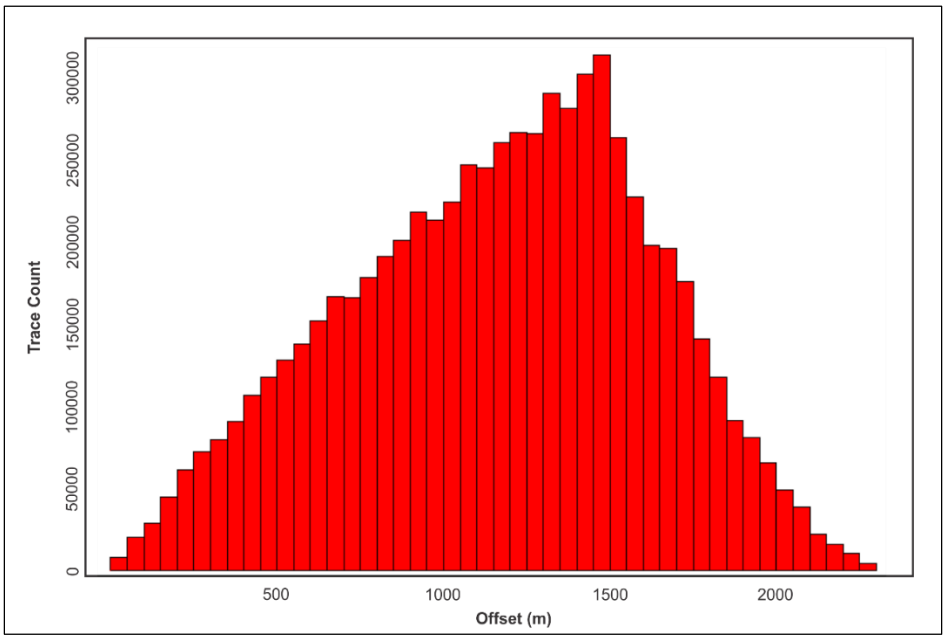

Figure 3.53. Trace Count-Offset plot of the 3-D survey.

Another important factor that determines data quality is the azimuth distribution. Each trace recorded from different azimuths stores valuable information about the subsurface structure in 3-D. Owing to the aspect ratio determined for the 3-D survey, uniform azimuth distribution was provided in order to image the target area adequately.

The Trace Count-Azimuth plot shows that the minimum number of traces that falls in each azimuth bin is 90,000 (Figure 3.54). Moreover, the number of traces that falls in 30°-60° and 120°-150° azimuth bins is higher than the average, as the missing traces on the corners and sides of the survey area provide poor azimuth distribution as a result of the shooting geometry. Even so, the average number of traces that falls in each azimuth bin is acceptable to sample the data from every azimuth bin.

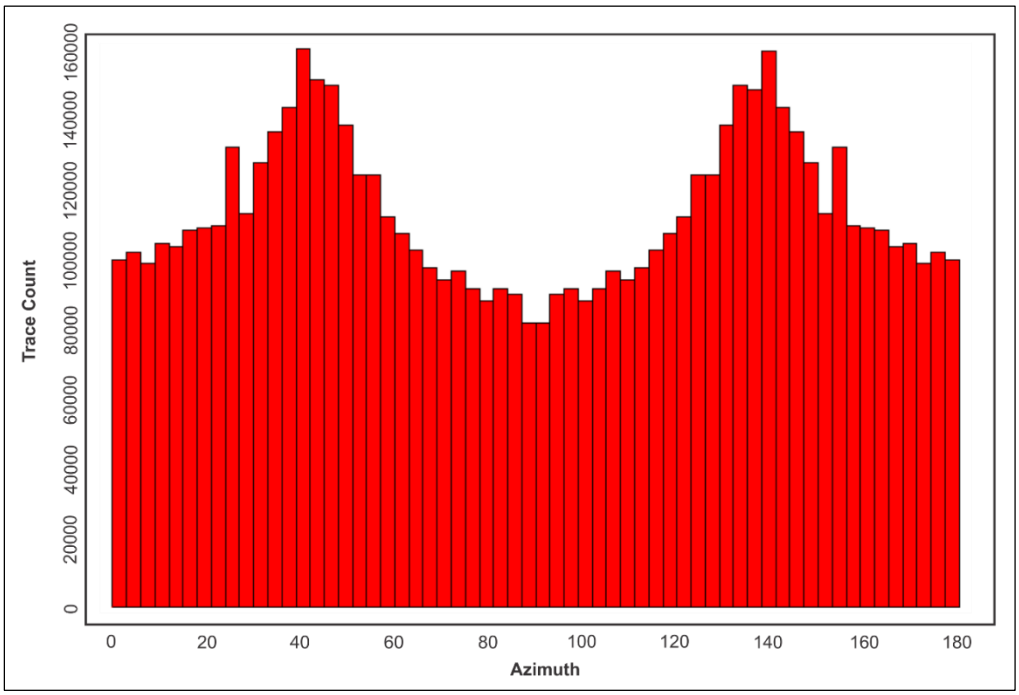

Figure 3.54. Trace Count-Azimuth plot of the 3-D survey.

Both the azimuth and offset distributions can be examined using a rose diagram. A rose diagram is colored by the number of traces that fall in each sector defined by the offset and azimuth. The rose diagram of the survey is shown in Figure 3.55. As expected, the number of traces increased with the larger offsets at every azimuth bin in the survey area.

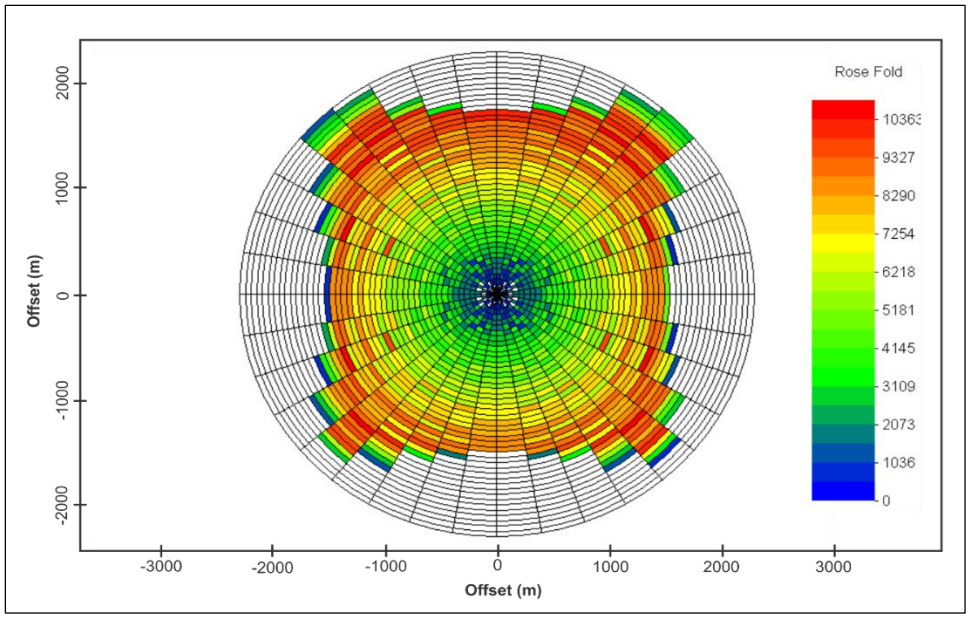

Figure 3.55. Rose diagram of the 3-D survey. Offset and azimuth sector steps are 50 m and 10°, respectively.

3.3.2.5 Pre-stack modeling and Imaging of 3-D seismic

The synthetic shot gathers from the designed 3-D seismic survey were modeled with a finite difference method using a full (two-way) acoustic wave equation. The pre-stack images of the data were produced with RTM. Before the shot gathers were modelled, CDP bins with 12.5 intervals were created from the velocity model. Therefore, CDP numbering ranged between 1 and 1279 in both in-line and cross-line directions. However, the survey area was limited between the 320th and 960th CDP numbers. The raw shot gathers created by the finite difference method for the 2745th (shot at In-line CDP 486 – Cross-line CDP 420) and 4924th (shot at In-line CDP 618 – Cross-line CDP 440) shots are shown in Figures 3.56 and 3.57, respectively.

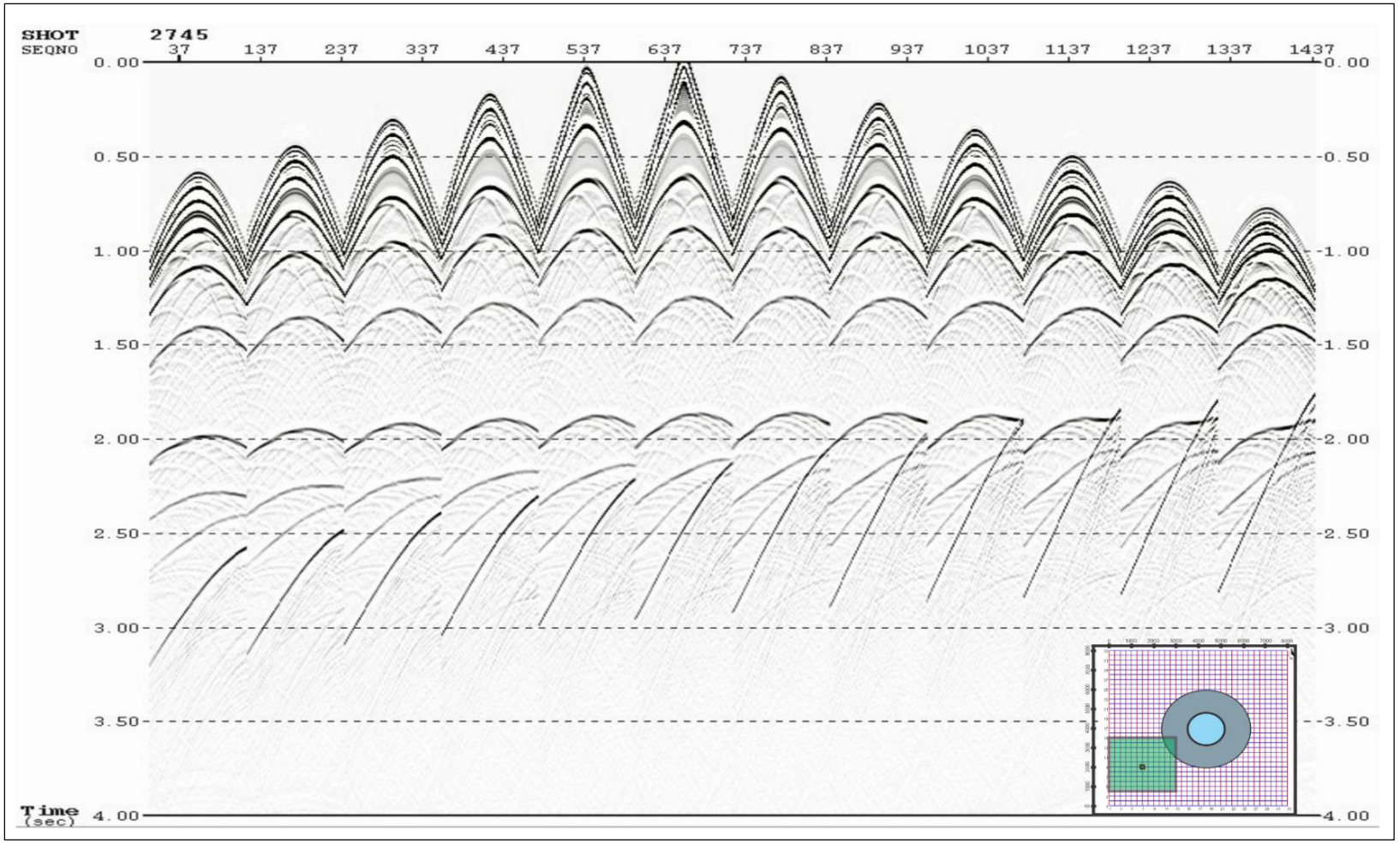

Figure 3.56. Raw shot gather of the 2745th shot. The location of the shot and active channels associated with the shot are shown with black and green squares, respectively.

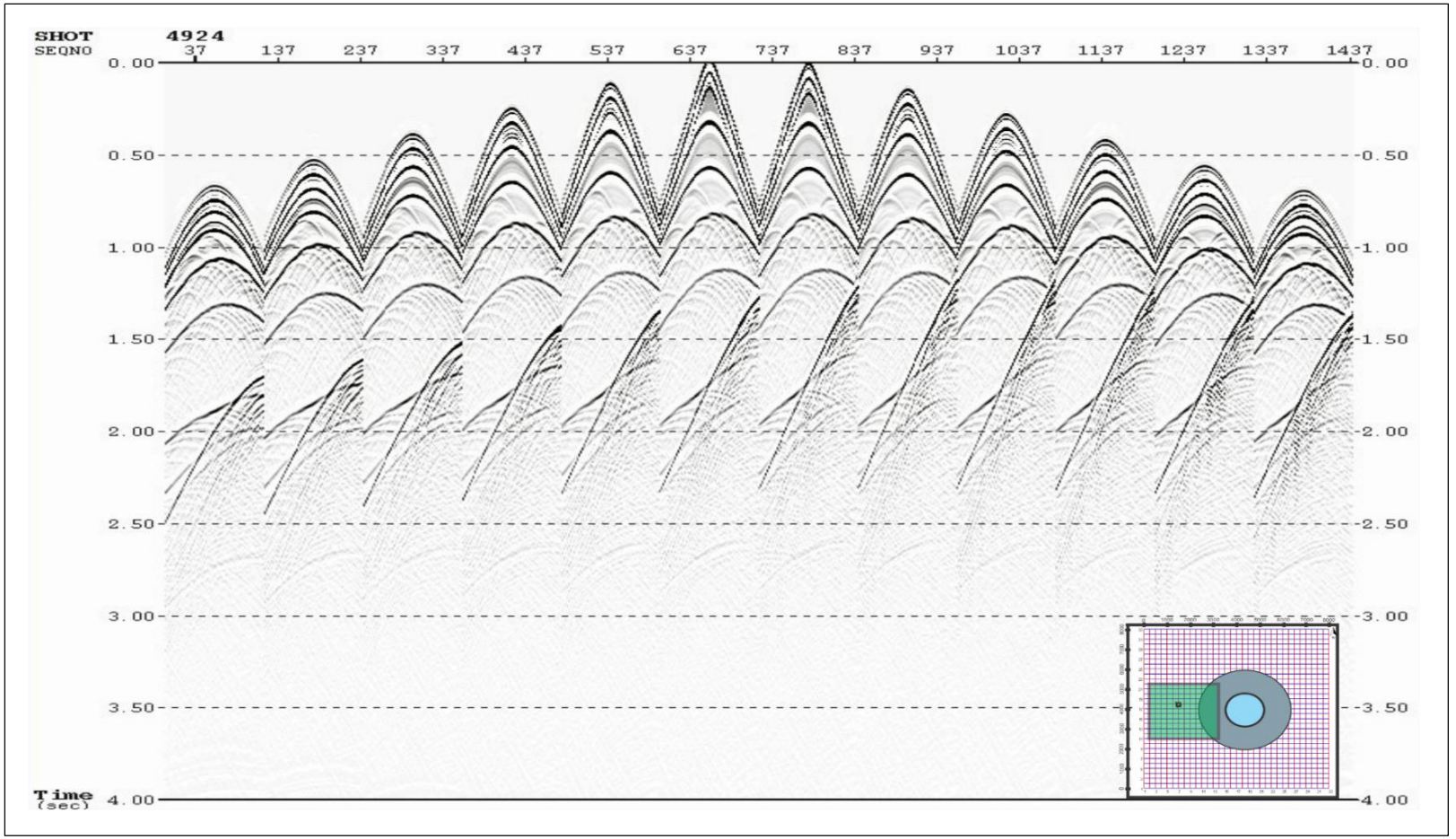

Figure 3.57. Raw shot gather of the 2745th shot. The location of the shot and active channels associated with the shot are shown with black and green squares, respectively.

As was observed in 2-D seismic imaging, especially shallow parts of the data contain low frequency noise caused by first breaks. Hence, the first breaks were filtered from each shot gather to increase the data quality. The RTM images of the synthetic 3-D data showed that the amplitudes of events dramatically decreased with increasing depth. Therefore, illumination of each shot was examined in order for them to be scaled with the raw RTM images. As a result, the amplitudes of the deeper events were normalized by scaling the RTM images with the illumination stack. The product of this process is shown in Figure 3.58.

After scaling with the illumination stack, the data were imaged with in-line, cross-line, and depth slices. As observed in in-line and cross-line images, the salt dome and surrounding sediments are adequately imaged with planned survey parameters (Figures 3.59-3.62). Also, the poorly built velocity model in 3-D had effects on the final RTM images. The stepped view of the horizons could be caused by coarse gridding, poor smoothing, or personal errors during modelling. Nevertheless, it can be counted as an advantage in order to test the survey design over the areas where faulting is also present.

Depth slices are very useful images for 3-D interpretation. The extension of the salt dome and location of the dipping horizons at exact depths can be observed by depth slices. The extension of the salt dome is symmetrical and circular at every depth range. But the horizons are seen as asymmetric circles, since their dip angles are variable throughout the model. The RTM image slices from 408 m, 2460 m, and 3360 m are shown in Figures 3.63-3.65.

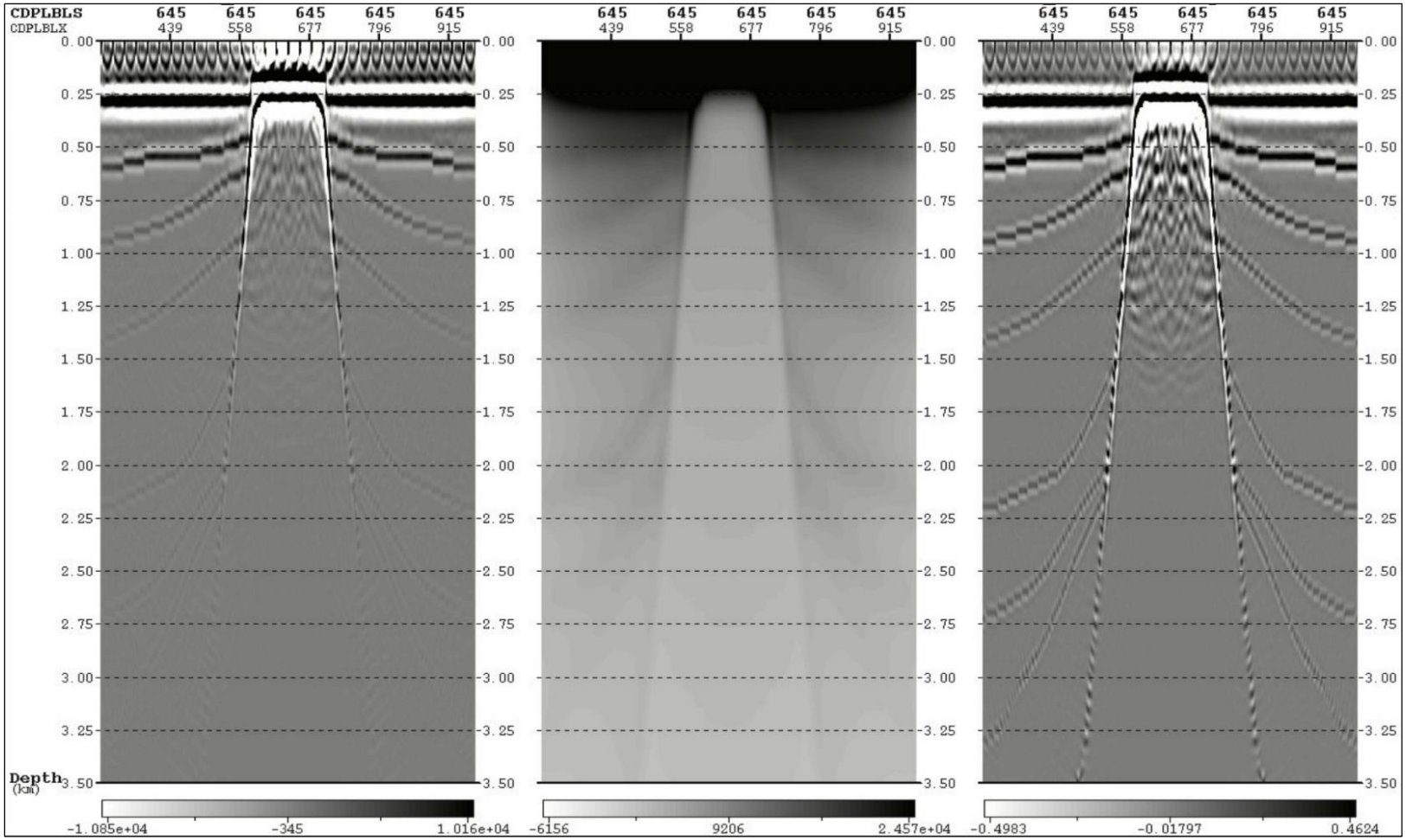

Figure 3.58. Process of scaling the RTM image with illumination stack. The raw RTM image (left), illumination stack (middle), and RTM image scaled with illumination stack (right) of inline 645 cross-section.

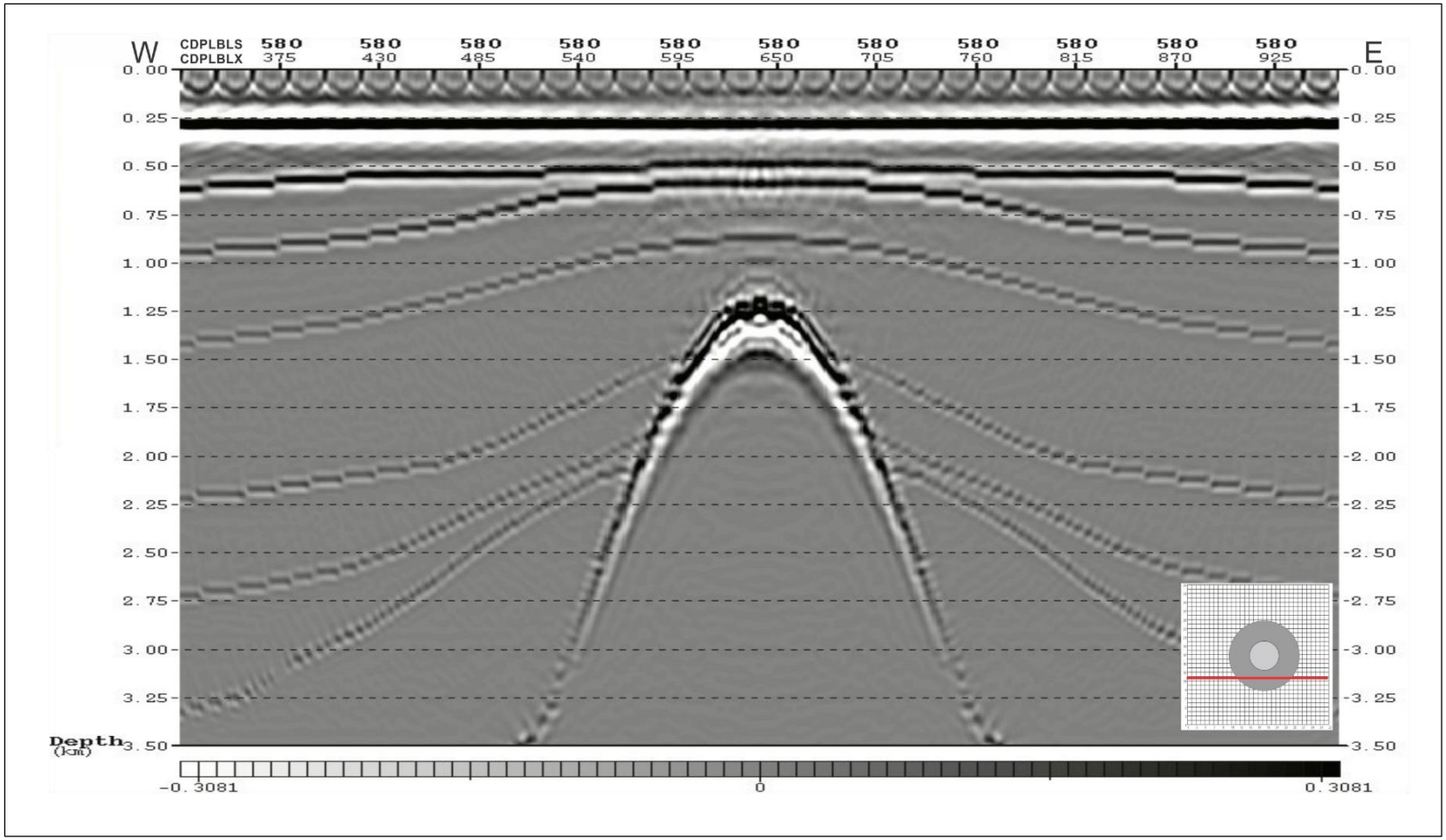

Figure 3.59. RTM image of the in-line 580th cross-section.

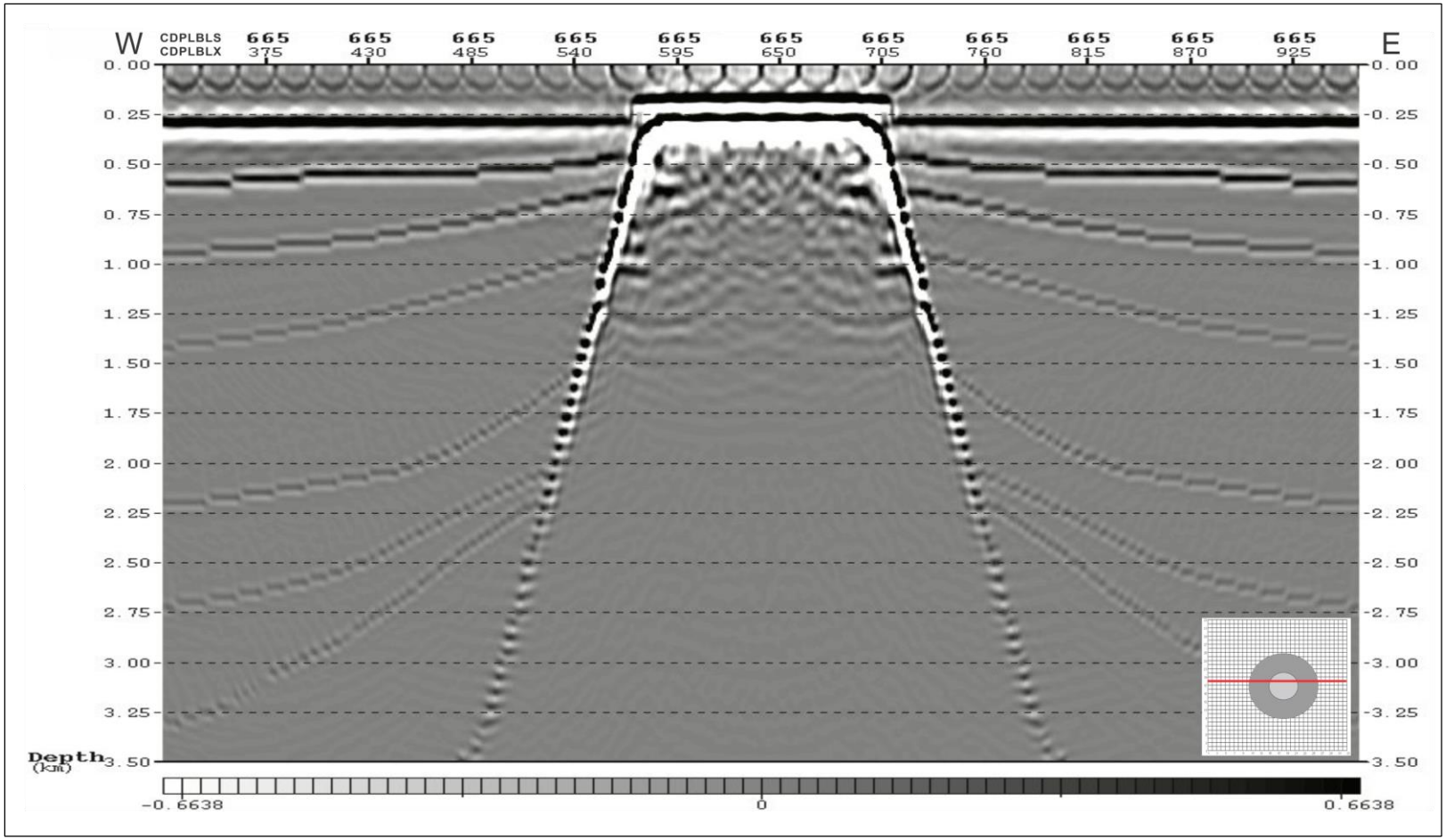

Figure 3.60. RTM image of the in-line 665th cross-section

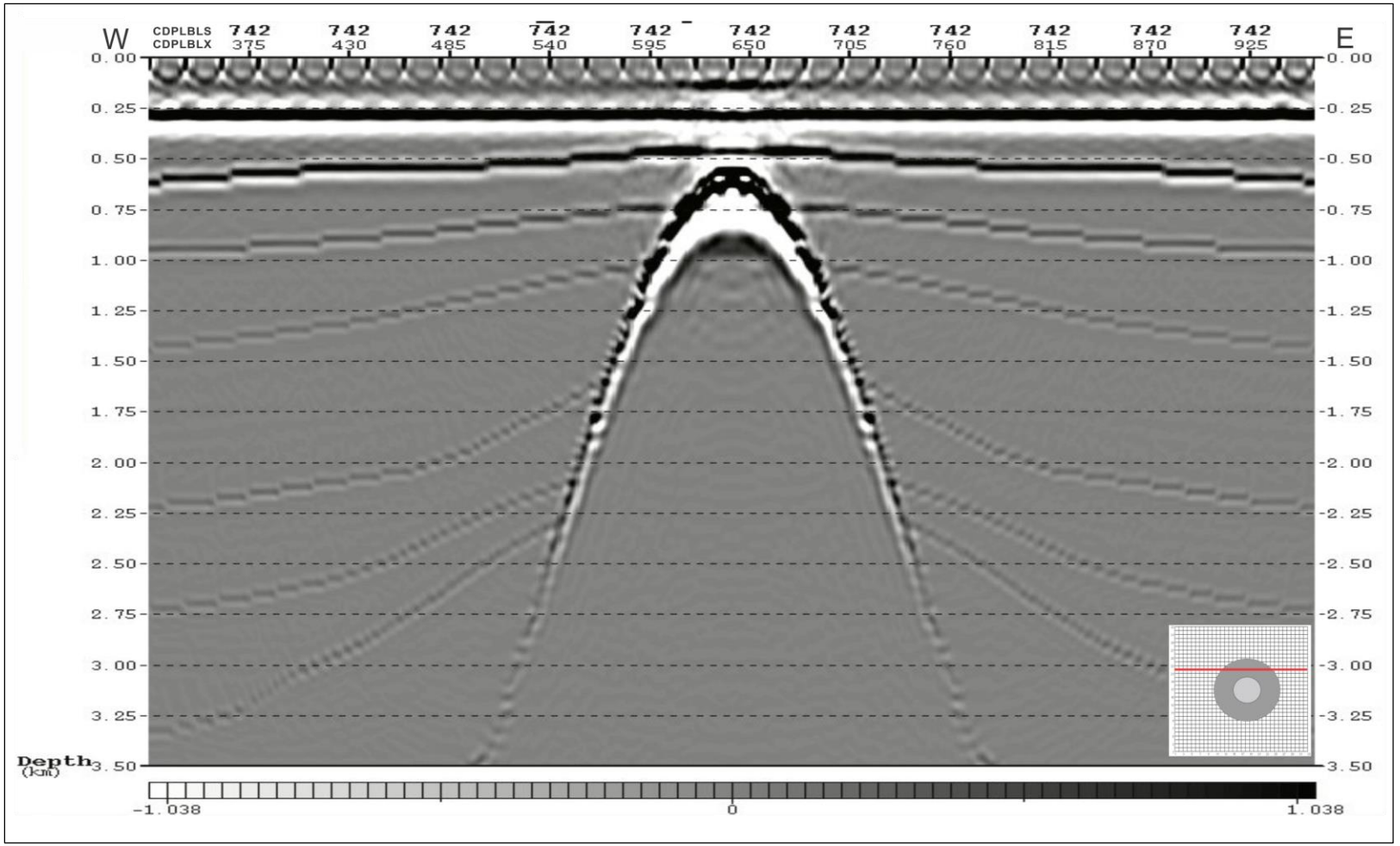

Figure 3.61. RTM image of the in-line 742nd cross-section.

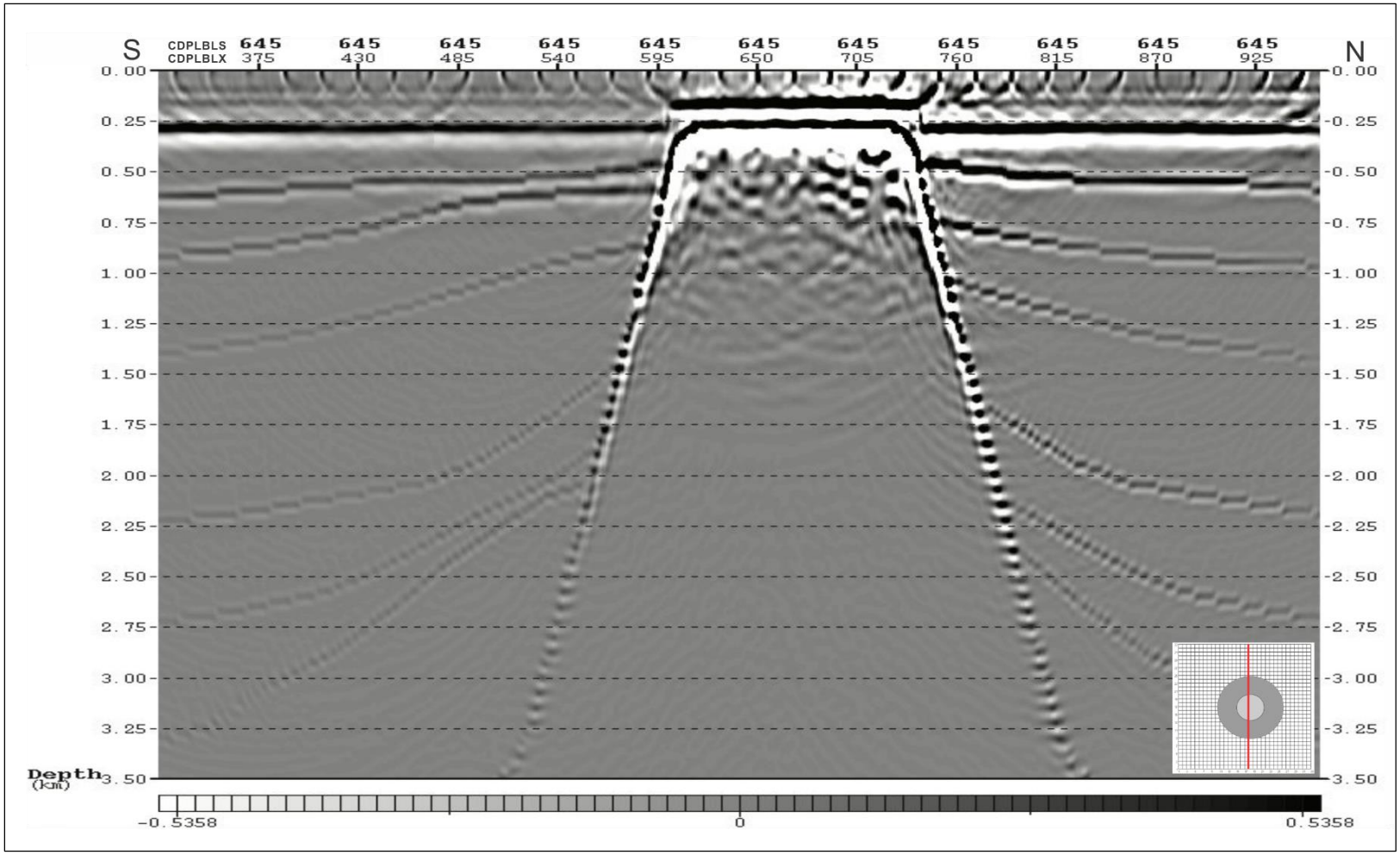

Figure 3.62. RTM image of the cross-line 645th cross-section.

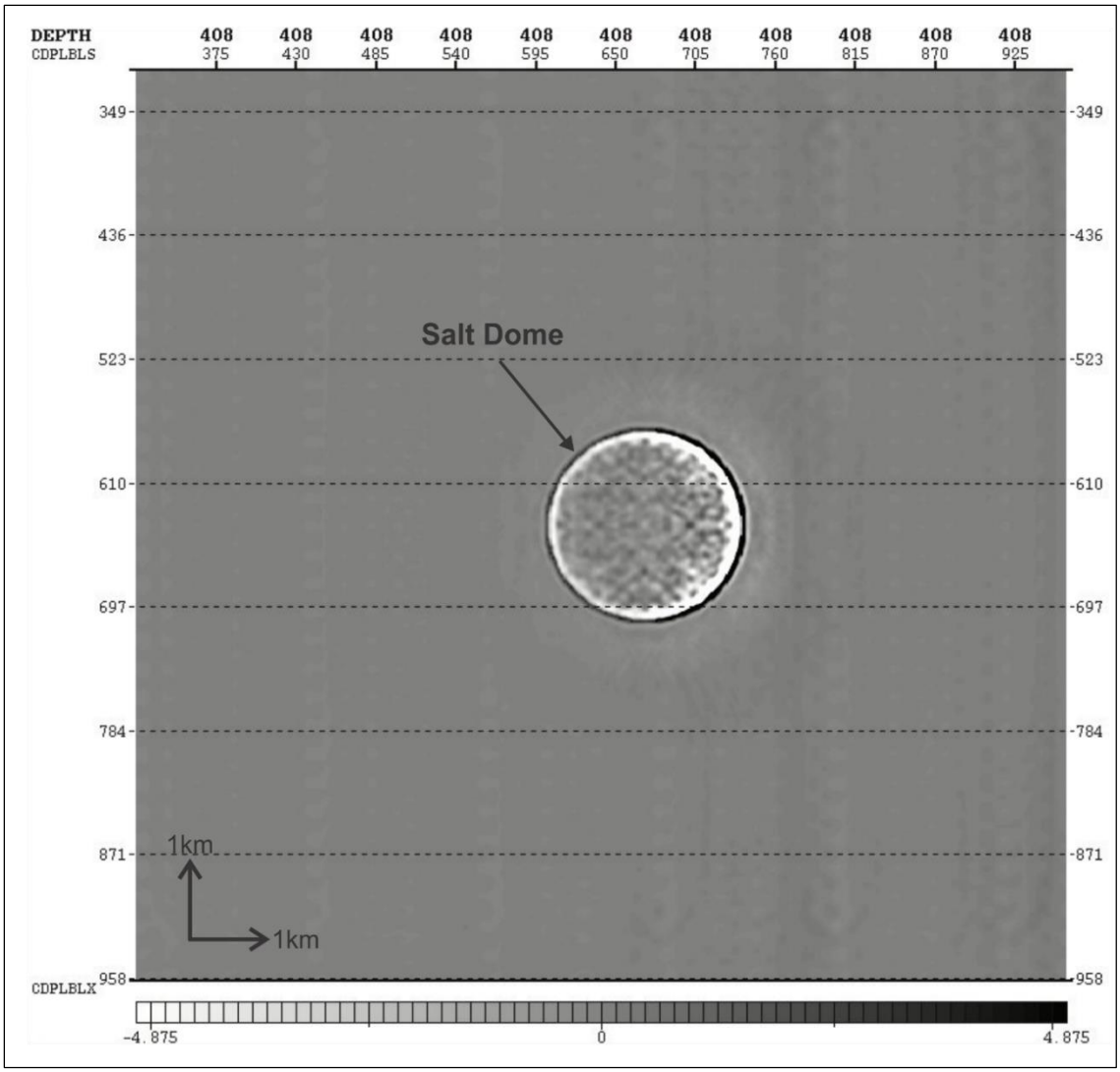

Figure 3.63. Depth slice image at 408 m. Circular reflection represents the boundary of the salt.

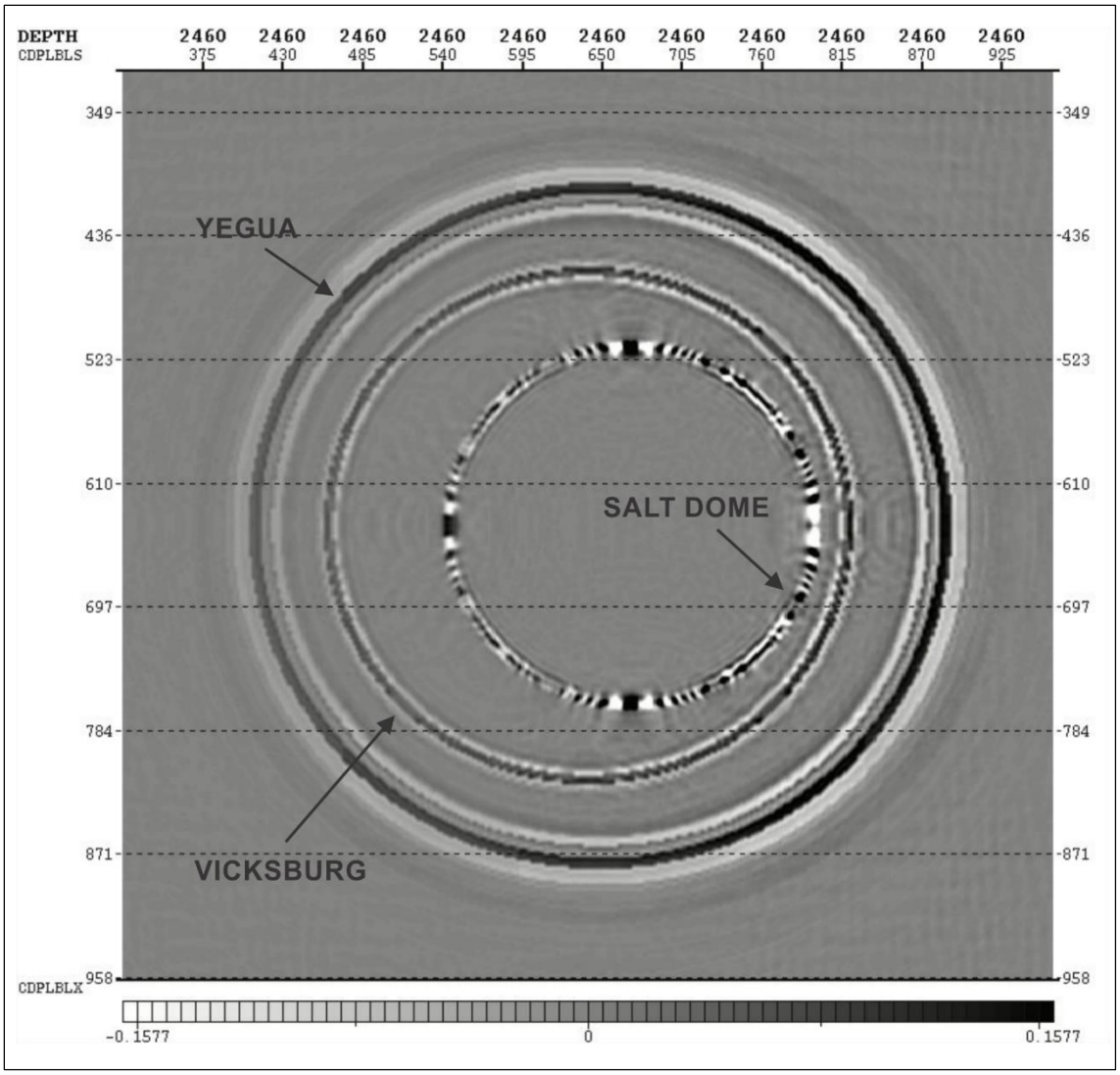

Figure 3.64. Depth slice image at 2460 m. Circular reflections represent the boundary of the salt, Vicksburg, and Yegua formations.

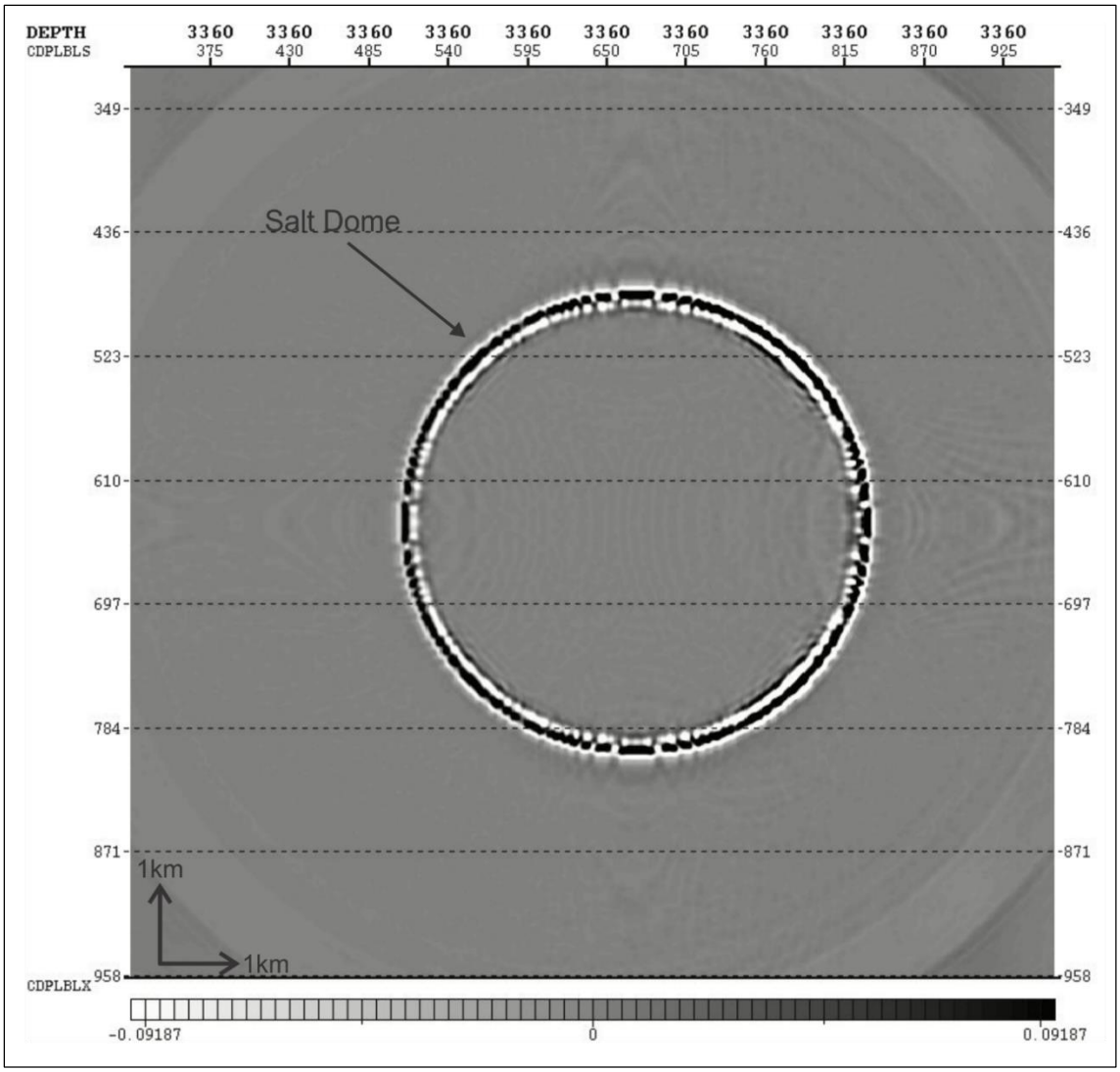

Figure 3.65. Depth slice image at 3360 m. Circular reflection represents the boundary of the salt almost at the bottom of the model.

CHAPTER FOUR: DISCUSSION

Two-D and 3-D seismic acquisition modelling studies in the Pierce Junction salt dome area were performed in order to find out the optimum parameters for cost-effective surveys while meeting the imaging objectives. Moreover, the surveys were designed considering the limited equipment of the Allied Geophysical Laboratories (AGL) which has facilities like small companies and other research institutions.

The proposed optimum survey parameters can be updated according to equipment capacity. Using less equipment than proposed for 2-D and 3-D surveys can prevent meeting the survey objectives.

In the 2-D survey, decreasing the number of geophones and using larger station intervals would cause aliasing issues, resulting in low lateral resolution. On the other hand, reducing the maximum offset of the survey would result in poor images, due to the lack of offset contribution, especially from dipping layers. Using larger shot intervals would reduce the cost of the survey. However, the quality of the data will also decrease, since the maximum fold of the survey would be diminished. Consequently, a survey designer whose objective is to image an area in 2-D adequately should use the proposed parameters. Otherwise, the data will not meet the imaging objectives.

The number of geophones needed for the proposed optimum survey parameters in 3-D is 1573, an affordable number for a small company or research institution. The only way to decrease the number of geophones used in the patch is to decrease the aspect

ratio. An aspect ratio of 1:1 is recommended for a 3-D survey in the study area in order to obtain good offset and azimuth distributions. Narrow azimuth (aspect ratio of the patch is less than 0.5:1) surveys are not recommended since they provide limited range of azimuth and less uniform offset distribution while higher weights of far offsets are expected for better image quality (Cordsen et al., 2000). Therefore, although it is affordable as is, if it is necessary to reduce the number of geophones, it is better to keep the aspect ratio higher than 0.5:1. Thus, the minimum number of geophones would be 968 for an aspect ratio of 0.6:1. Recording the seismic traces coming from every range of azimuth in a given study area is quite important. Therefore, an aspect ratio of 1:1 is highly recommended for imaging the salt dome and the surrounding area.

The study area is situated in the middle of many busy highways, railroads, and apartment complexes. Moreover, there are lots of oil producing wells and oil/gas storage facilities in the area. Hence, ambient noise was the major problem for our seismic study. In this study, acquisitions were modelled without any noise addition to the raw shot gathers. The field tests applied before shooting the survey or available 2-D data can be helpful to determine the number of vertical stacks to increase signal-to-noise ratio. Increasing the maximum fold of the survey with higher shot density is another option for achieving better signal-to-noise ratio.

RTM modeling has become more applicable with the recent advancements in computing technologies. Several companies leading the industry use this technique in many 3-D seismic projects. However, it is still counted as an expensive technique for

small-scale companies, since it requires powerful hardware along with good storage capacity. This study has been done using Paradigm's powerful work stations. Recent improvements in computer systems and programming science will make this technique more viable for more common commercial use.

CHAPTER FIVE: LIMITATIONS OF THE STUDY

The main limitation of this study is the unavailability of data for building more accurate velocity models for the study area.

A 2-D velocity model of the study area was built using 2-D seismic data acquired on the top of the salt, on the east-west geological cross-section drawn by Glass (1953). However, there is no available documentation about the study area other than Glass (1953). Additional 2-D seismic data from the sides of the salt dome would provide detailed velocity information to increase the complexity of the model by inserting sub-layers and velocity gradients. Also, an extensive geological cross-section would provide thickness and dipping information about the layers. Moreover, petrophysical properties of the layers would affect the velocity building part of the study significantly.

A classic circular piercement salt dome shape having the dimensions of the Pierce Junction salt dome was used in 3-D velocity model. Also, horizons around the salt were created rotating the 2-D velocity model 360° around the origin. In order to build an accurate 3-D velocity model of the study area, a sufficient number of well logs and 2-D seismic information around the salt dome and adequately sampled 3-D gravity data for modelling the shape of the salt dome and its surroundings are also required.

CHAPTER SIX: SUMMARY AND CONCLUSION

The optimum seismic survey parameters to adequately image the Pierce Junction salt dome and its surrounding sediments in both 2-D and 3-D were determined by acquisition modeling. The velocity models of the study area were built with the help of the available data and previous studies. The synthetic raw shot gathers were created by the finite difference method using a full (two-way) acoustic wave equation and pre-stack imaging using RTM.

Instead of calculating the survey parameters with basic survey design formulas, 2-D survey parameters, such as maximum offset, group and shot interval, recording time, and profile length, were determined by observations on the final RTM images. However, the initial survey design parameters were calculated using basic formulas. Afterwards, the parameters were updated with the limited geophysical equipment of the AGL while preserving the desired image quality. Finally, it was proposed that a conventional 2-D survey can be performed using 150 geophones with a 20 m interval and 200 shots with a 40 m interval. The length of the receiver line (11 km) was chosen to be longer than that of the shot profile (8 km) in order to have a good full-fold distribution. Although the maximum fold of the survey is high enough, the number of vertical stacks can be increased when performing field tests in a real survey environment.

Once the optimum parameters for the 2-D seismic survey were determined, they were adapted to the 3-D survey. The 3-D survey with orthogonal geometry was planned

for an 8 km by 8 km square area. Thirty-three in-lines and 33 cross-lines were distributed over the survey area with 250 m intervals. The patch is the most important factor that determines the equipment requirements of a survey. The receiver interval of the patch was determined to be 25 m for balancing the cost and imaging objectives of the survey. Consequently, it was proposed that a minimum of 1573 geophones are needed to image the study area adequately. Reducing the number of the geophones is possible by decreasing the aspect ratio of the patch. But it is not recommended, since the poor azimuth and offset distributions will adversely affect the image resolution.

REFERENCES

Bain, R. C., 2010, Hidden structure revealed by a Simple 3D Velocity Model—McAllen Ranch Field, Hidalgo County, Texas: Gulf Coast Association of Geological Societies Transactions, **60**, 39-55.

Barton, D. C., 1933, Mechanics of formation of salt domes with special reference to Gulf Coast salt domes of Texas and Louisiana: AAPG Bulletin, **17(9)**, 1025-1083.

Baysal, E., D. D. Kosloff, and J. W. Sherwood, 1983, Reverse time migration: Geophysics, **48(11)**, 1514-1524.

Beckman, J. D., and A. K. Williamson, 1990, Salt dome locations in the gulf coastal plain, south-central United States: US Geological Survey, Water-Resources Investigations Report no: 90-4060.

Boyd, T. M., 2003. Introduction to Geophysical Exploration, http://galitzin.mines.edu/INTROGP/, accessed December 2010.

Carmichael, R. S., 1984, CRC Handbook of Physical Properties of Rocks, Volume III: CRC Press.

Castagna, J. P., M. L. Batzle, and R. L. Eastwood, 1985, Relationships between compressional-wave and shear-wave velocities in clastic silicate rocks: Geophysics, **50(4)**, 571-581.

Chaouch, A., and J. L. Mari, 2006, 3-D land seismic surveys: Definition of geophysical parameters: Oil & Gas Science and Technology-Revue de l'IFP, **61(5)**, 611-630.

Claerbout, J. F., 1985, Fundamentals of Geophysical Data Processing: Blackwell Scientific Publications.

Cordsen, A., 1995, Arrangement of source and receiver lines for three-dimensional seismic data acquisition: U.S. Patent 5,402,391.

Cordsen, A., M. Galbraith, and J. Peirce, 2000, Planning Land 3-D Seismic Surveys: Geophysical Development No: 9, SEG Publications.

Darton, N. H., 1933, Guidebook of the Western United States: Part F. The Southern Pacific Lines, New Orleans to Los Angeles: US Geological Survey series, **845**.

Ebrom, D., X. Li, J. McDonald, and L. Lu, 1995, Bin spacing in land 3-D seismic surveys and horizontal resolution in time slices: The Leading Edge, **14(1)**, 37-40.

Embree, P., 1985, Resolutions and rules of thumb: SEG Seismic Field Techniques Workshop, SEG Publications.

Ewing, T.E., N. Tyler, and R.A. Morton, 1983, Consolidation of geologic studies of geo-pressured geothermal resources in Texas: United States Department of Energy Report No: ACOS-79ET27111.

Ewing, T. E., 1991, Structural framework, *in* The Gulf of Mexico Basin: Geological Society of America Publications, 31-52.

Freeland, J. M., and J. E. Hogg, 1990, What does migration do to seismic resolution?: Recorder, **5(1)**, 6-15.

Feely, H. W., and J. L. Kulp, 1957, Origin of Gulf Coast salt-dome sulphur deposits: AAPG Bulletin, **41(8)**, 1802-1853.

Glass, N.C., 1953, Pierce Junction field, Harris County, Texas *in* Guidebook, field trip routes, oil fields, geology: Houston Geological Society, 143-150

Gore, R.H., 1992, The Gulf of Mexico: Pineapple Press, Inc.

Goupillaud, P., A. Grossmann, and J. Morlet, 1984, Cycle-octave and related transforms in seismic signal analysis: Geoexploration, **23(1)**, 85-102.

Halbouty, M. T., and G. C. Hardin, 1956, Genesis of salt domes of Gulf Coastal Plain: AAPG Bulletin, **40(4)**, 737-746.

Halbouty, M. T., 1967, Salt Domes: Gulf Region, United States, and Mexico: Gulf Publishing Company.

Halbouty, M.T., 1979, Salt Domes of Gulf Region, United States and Mexico, 2nd ed. Houston, Texas: Gulf Publishing Company.

Holzer, T. L., and R. L. Bluntzer, 1984, Land subsidence near oil and gas fields, Houston, Texas. Ground Water, **22(4)**, 450-459.

Huang, Z. Y., 2012, Multidisciplinary Investigation of Surface Deformation above Salt Domes in Houston, Texas: Master Thesis, University of Houston.

Hudec, M. R., and M. Jackson, 2007, Terra infirma: Understanding salt tectonics: Earth-Science Reviews, **82(1)**, 1-28.

Huffman, A. C., 2004, Salt diapirs in the Gulf Coast U.S. Dataset accessed 10 October 2013 at https://catalog.data.gov/dataset/salt-diapirs-in-the-gulf-coast-gcdiapirg.

Jackson, M. T., and C. J. Talbot, 1986, External shapes, strain rates, and dynamics of salt structures: Geological Society of America Bulletin, **97(3)**, 305-323.

Jiao, K., W. Huang, V. Denes, J. Kapoor, R. Coates, E.W. Starr, and X. Cheng, 2012, Elastic migration for improving salt and subsalt imaging and inversion: 82nd Annual International Meeting, SEG, Expended Abstracts, 1-5.

Konyukhov, A. I., 2008, Geological structure, evolution stages, and petroliferous complexes of the Gulf of Mexico basin: Lithology and Mineral Resources, **43(4)**, 380-393.

Krey, T. C., 1987, Attenuation of random noise by 2-D and 3-D CDP stacking and Kirchhoff migration: Geophysical Prospecting, **35(2)**, 135-147.

Kupfer, D.H., 1989, Diapirism sequences as indicated by internal salt structures: Gulf Coast Section Society of Economic Paleontologists and Mineralogists Foundation 10th Annual Research Program and Abstracts, 79-89.

Kyle, J. R., M. R. Ulrich, and W. A. Gose, 1987, Textural and paleomagnetic evidence for the mechanism and timing of anhydrite cap rock formation, Winnfield salt dome, Louisiana *in* Dynamical Geology of Salt and Related Structures: Academic Press, Inc., 497-542.

Lash, C. C., 1980, Shear waves, multiple reflections, and converted waves found by a deep vertical wave test (vertical seismic profiling): Geophysics, **45(9)**, 1373-1411.

Liner, C., 2004, Elements of 3-D Seismology: PennWell Books.

Margrave, G. F., 1997, Seismic acquisition parameter considerations for a linear velocity medium. 67th Annual International Meeting, SEG, Expended Abstracts, 47-50.

Moritz, H., 1980, Geodetic reference system 1980: Journal of Geodesy, **54(3)**, 395-405.

Morlet, J., G. Arens, E. Fourgeau, and D. Glard, 1982, Wave propagation and sampling theory Part-I: Complex signal and scattering in multilayered media: Geophysics, **47(2)**, 203-221.

Murray, G. E., 1961, Geology of the Atlantic and Gulf coastal province of North America: Harper Publications.

Neff, W. H., and H. K. Rigdon, 1994, Incorporating structure into 3D seismic survey preplanning: A mid-continent example *in* MESA Technology Conference.

Nelson, T. H., 1991, Salt tectonics and listric-normal faulting *in* The Gulf of Mexico Basin: Geological Society of America Publications, 73-89.

Nettleton, L. L., 1934, Fluid mechanics of salt domes: AAPG Bulletin, **18(9)**, 1175-1204.

Nettleton, L. L., 1976, Gravity and Magnetics in Oil Prospecting: McGraw-Hill Publications.

Oezsen, R., 2004, Velocity modelling and prestack depth imaging below complex salt structures: a case history from on-shore Germany: Geophysical prospecting, **52(6)**, 693-705.

Oppenheim, A. V., R. W. Schafer, and J. R. Buck, 1999, Discrete-Time Signal Processing: Prentice Hall Publications.

Otoum, M. A., 2011, An Integrated Geophysical Investigation to Map the Hockley Active Fault in Northwest Harris County, Texas: Doctoral dissertation, University of Houston.

Parra, O. J. and H. A. Collier, 1997, Petrophysical properties and geology of selected intervals in the Frio formation, Stratton field for modeling interwell seismic logging responses: 38th Annual Logging Symposium of Society of Petrophysicists and Well Log Analysts, Expanded Abstracts.

Partyka, G., J. Gridley, and J. Lopez, 1999, Interpretational applications of spectral decomposition in reservoir characterization: The Leading Edge, **18(3)**, 353-360.

Posey, H. H., and J. R. Kyle, 1988, Fluid-rock interactions in the salt dome environment: an introduction and review: Chemical Geology, **74(1)**, 1-24.

Prieto, C., 2000, Gravity/magnetic signatures of various geologic models-an exercise in pattern recognition: Footnotes on Interpretation, **4(4)**, 20-27.

Railroad Commission of Texas, Oil and Gas Well Records. Data accessed 10 October 2013 at http://www.rrc.state.tx.us/data/wells/wellrecords.php.

Robinson, E.A., and S. Treitel, 1980, Geophysical Signal Analysis: Prentice Hall Publications.

Querio, C. W., 1974, Simultaneous Storage of LPG and Production of Brine, Pierce Junction Dome, Houston, Texas: 4th Symposium of Northern Ohio Geological Society, Expanded Abstracts, 285-290.

Salvador, A. (1991). Origin and development of the Gulf of Mexico basin *in* The Gulf of Mexico Basin: Geological Society of America Publications, 389-444.

Seigel, H. O., I. Brcic, and P. Mistry, 1995, A guide to high precision land gravimeter surveys: Scintrex LTD.

Seni, S. J., W. F. Mullican, and H. S. Hamlin, 1984, Texas Salt Domes-Aspects Affecting Disposal of Toxic-chemical Waste in Solution-mined Caverns: Bureau of Economic Geology, University of Texas at Austin Publications.

Sheriff, R. E., 2002, In Encyclopedic Dictionary of Applied Geophysics: SEG Publications.

Stone, D. G., 1994, Designing Seismic Surveys in Two and Three dimensions: SEG Publications.

Taner, M. T., F. Koehler, and R. E. Sheriff, 1979, Complex seismic trace analysis: Geophysics, **44(6)**, 1041-1063.

Thomas, R. L., and R. M. Gehle, 2000, A brief history of salt cavern use: 8th World Salt Symposium, Expanded Abstracts, 207-214.

Vermeer, G. J., 1998, 3-D symmetric sampling in theory and practice: The Leading Edge, **17(11)**, 1514-1519.

Vermeer, G. J., 1999, Factors affecting spatial resolution: Geophysics, **64(3)**, 942-953.

Vermeer, G. J. O., 2002, 3-D Seismic survey design: SEG Publications.

Willis, M. E., R. Lu, X. Campman, N. Toksoz, Y. Zhang, and M. V. D. Hoop, 2006, A novel application of time-reversed acoustics: Salt-dome flank imaging using walkaway VSP surveys: Geophysics, **71(2)**, 7-11.

Wright, S., 2004, Azimuth and offset in design of successful 3-D survey: AAPG Search and Discovery Article no. 40118.